A NEW MULTICONTINUUM MODEL FOR COMPOSITIONAL GAS TRANSPORT IN A DEFORMABLE SHALE FORMATION

A Dissertation

by

OLUFEMI MOROUNFOPEFOLUWA OLORODE

Submitted to the Office of Graduate and Professional Studies of
Texas A&M University
in partial fulfillment of the requirements for the degree of

DOCTOR OF PHILOSOPHY

Chair of Committee,	Yucel I. Akkutlu
Co-Chair of Committee,	Yalchin Efendiev
Committee Members,	Nobuo Morita
	Raytcho Lazarov
Head of Department,	A. Dan Hill

August 2017

Major Subject: Petroleum Engineering

ABSTRACT

A new multi-continuum compositional gas simulation model is presented for deformable organic-rich source rocks. The model describes the advective and diffusive mass balance equations for each hydrocarbon components in the organic and inorganic continua. It accounts for the presence of dispersed kerogen with sorbed-gas corrected dynamic porosity. Maxwell-Stefan theory is used to predict the pressure- and composition-dependence of molecular diffusion. The coupled nonlinear system of equations for the multi-component gas transport and geomechanics are discretized using the control volume finite element method, and linearized using the Newton-Raphson iteration scheme. Any fractures in the reservoir domain is modeled using the discrete fracture model.

The simulation is based on a new multi-scale conceptual flow model, in which the kerogen is considered to be discontinuous and dispersed in the inorganic matrix at reservoir simulation scale. Scanning Electron Microscopy images, as well as the expected slow transport in the nanoporous organic matrix in comparison to the advective transport in the organic matrix form the basis for this new numerical model. A simple mass balance equation is introduced to enable kerogen to transfer reservoir fluids to the inorganic matrix that is collocated in the same grid-block. The advective-diffusive transport takes place between neighboring grid blocks only in the inorganic matrix.

The simulation results indicate that the multi-scale nature of the rock is important and should not be ignored because this could result in an overestimation of the contribution of kerogen to production. Although the adsorbed fluid can contribute significantly to storage in these source rocks, its contribution to production could be severely limited by the lack of kerogen continuity at the reservoir scale and by a low degree of coupling between the organic and inorganic pores. The contribution of Maxwell-Stefan diffusion to the over-

all transport in organic-rich source rocks appears to be more significant at lower values of matrix permeability, and as the permeability decreases in response to pressure decline during production. The coupled geomechanics and flow simulation results indicate that production of reservoir fluids can induce higher compressive stresses that can in turn reduce fracture conductivity, and lead to faster production decline.

DEDICATION

To my mother, sister, and brother for providing so much inspiration and support throughout my academic journey.

ACKNOWLEDGMENTS

I would like to thank Dr Akkutlu for the insights and guidance he provided throughout the course of my research, and for serving as the chair of my graduate committee. I am grateful to Dr Efendiev for his research supervision as the co-chair of my graduate committee. Dr Morita and Dr Lazarov also served on my graduate committee, and I appreciate their valuable contributions to this research work.

I am also grateful for the departmental funding I received during my program at Texas A&M University. The Texas A&M supercomputing facilities, as well as the departmental computing resources help facilitate my research work.

I would like to thank my friends at Texas A&M University who contributed in different ways to the rich experience I had here at College Station. My office mates also contributed to the quality of my experience at Texas A&M, and I appreciate all the useful discussions we had.

CONTRIBUTORS AND FUNDING SOURCES

Contributors

This work was supported by a dissertation committee consisting of Professor Akkutlu of the Department of Petroleum Engineering as chair, and Professor Efendiev of the Department of Mathematics as co-chair. Professor Morita of the Department of Petroleum Engineering and Professor Lazarov of the Department of Mathematics also served as members of my dissertation committee. All work for the dissertation was completed independently by the student.

Funding Sources

Graduate study was supported by departmental funding.

NOMENCLATURE

y	vector of mole fractions of components, i in the gas phase
y_i	mole fraction of component, i in the gas phase
z	vector of overall mole fractions
z_i	overall mole fraction of component, i
c	total concentration or total molar density, mol/m^3
c_i	concentration or molar density of component i, mol/m^3
c_G	concentration or molar density of the gas phase, mol/m^3
c_μ	adsorbed-gas concentration in kerogen in mole per grain volume, mol/m^3
$c_{\mu s}$	maximum monolayer gas adsorption on the internal kerogen solid surfaces (in mole per grain volume, mol/m^3)
c_L	Langmuir concentration, mol/m^3
ϵ_{kp}	kerogen pore volume per total matrix pore volume
ϵ_{ks}	total organic content in terms of organic grain volume per total grain volume
v	total Darcy velocity of the bulk phase m/s
k	matrix permeability, m^2
l_m	shape factor
p	pressure, Pa
D	matrix of diffusion coefficients in inorganic pores, m^2/s
$\mathbf{D_k}$	matrix of diffusion coefficients in organic pores, m^2/s

$\mathbf{D_s}$	matrix of surface diffusion coefficients in kerogen, m^2/s
$\mathcal{B}$	drag matrix
J_i	relative (molar) flux of component, i
ϕ	porosity
μ	viscosity, Pa.s
τ	tortuosity
Γ	matrix of thermodynamic factor

TABLE OF CONTENTS

Page

LIST OF FIGURES

FIGURE Page

LIST OF TABLES

TABLE Page

1. INTRODUCTION

1.1 Statement of the Problem

Commercial production of oil and gas from organic-rich source rocks has contributed significantly towards the global energy supply over the past decade. The technologies that facilitated the commercial production from these ultra-low unconventional resources include hydraulic fracturing and horizontal drilling. Several researchers have therefore developed models to describe the macroscopic transport of reservoir fluids towards the multiply-fractured horizontal wells in these unconventional resources. There appears to be a general consensus that the network of hydraulic fractures, natural fractures and/or microcracks in these source rocks play a dominant role in the production, especially early in the production life of these resources. However, the production typically shows a sharp decline, which could be indicative of a transition from the early time, when the production is mainly due to the flow in the fractures, to a later period, when the matrix begins to contribute to production. Considering that these ultra-low permeability resources are typically characterized by long production periods, a study of the storage and transport mechanisms in both the fractures and matrices will be pivotal to the optimization of production from these resources. At present, there is active research in the area of fracture modeling and hydraulic fracture propagation. This work, in addition to the modeling of the production of multi-component gas from the hydraulic fractures, also focuses on the study of the shale matrix, and could provide new insights into the optimization of production from these source-rocks.

This research involves the development of a new numerical model and simulator to describe the coupled geomechanics and transport of multi-component gas in organic-rich source rocks. Several authors have published different variations of multiple-continuum

models, like the dual-continuum models, and triple continuum models, among others. In these models, the matrix of the source-rock is typically modeled as two different continua, comprising an inorganic matrix and an organic matrix, which is also known as kerogen. In the triple continuum models, the fractures are typically modeled as the third continuum. In this research, I develop a new model which seeks to honor the observation that Scanning Electron Microscopy (SEM) images indicate that kerogen could be discontinuous and dispersed within the inorganic matrix at the reservoir simulation scale. The SEM images are typically on the order of micrometers, and they generally indicate that the kerogen is less abundant and dispersed within the inorganic matrix. In this research, I therefore neglect the continuous transport (by advection and diffusion) of hydrocarbons in the organic matrix based on the argument that the kerogen will be discontinuous at the large scales associated with reservoir simulation. The fact that the diffusion-dominated transport in the organic matrix is expected to be much slower than the advection-dominated transport in the microcracks also supports the argument in favor of neglecting the continuous transport of hydrocarbons in the organic matrix. The model presented in this work allows the release of fluids from the organic matrix into the inorganic matrix, but does not allow the continuous transport of fluids from the organic matrix in a simulation cell to the organic matrix in the neighboring cell.

Organic-rich source rocks are known to have very low matrix permeability values, which leads to very long transient flow in these matrices. In order to capture the transient flow in the coupling between the organic and inorganic matrices, I derived a transient shape factor by making analogy to the Zimmerman transient shape factor that was developed for a dual-permeability matrix/fracture system. To model the molecular diffusion of multiple hydrocarbon components under concentration gradient, I used the multi-component Maxwell-Stefan diffusion model. This, unlike most of the published models accounts for the dependence of the diffusion coefficient tensor on pressure and composition. To

accurately model the storage of multi-component gas in the organic matrix, I extended the petrophysical model presented by Ambrose et al. (2012) and Hartman et al. (2012), and incorporated this in the mass balance equation for the organic matrix. The Ambrose et al. (2012) model accounts for the pore-volume occupied by the adsorbed gas molecules, which was not considered in the old methodology that simply added the adsorbed gas amount to the amount of gas stored in the pores (without considering that the amount of gas in the pores will be reduced by an amount equal to the pore volume occupied by the adsorbed gas molecules).

Considering the importance of propped hydraulic fractures to commercial production, this research also presents a fully-coupled geomechanics and multi-component gas simulator that is able to dynamically model the expected reduction in fracture aperture and conductivity due to the closing stresses that are induced as reservoir fluids are produced from these organic-rich source rocks. The coupling of the storage mechanism, which accounts for the pore-volume occupied by the adsorbed gas molecules, together with the mechanical deformation of the rock provides the ability to study the dynamics of pore-volume reduction due to the decrease in pressure during production, as well as the potential increase in pore volume due to the release of some adsorbed gas molecules. The Control Volume Finite Element Method (CVFEM) was used to discretize all the species mass balance equations and linear momentum balance equations, because it provides a mass conservative scheme with flexible gridding, where all primary variables are co-located at the vertices of the elements. The coupled geomechanics and compositional flow simulator is used to perform a numerical study of the effect of the elastic and creep deformation of the proppants during production. The simulator is also used to study to potential of storing CO_2 in a depleted Barnett-type shale. The core objective of this numerical study is to evaluate the feasibility of injecting CO_2 into this shale, and to study of the potential of the kerogen in trapping the injected CO_2.

1.2 Objectives

The overall objectives of this research are:

1. To develop a mathematical model for the transport of multi-component gas in a shale matrix, consisting of the organic and inorganic matrices. Unlike previous models for transport in shales, this work models the organic matrix (or kerogen) as a dispersed and discontinuous continuum. The rationale behind this dispersed kerogen model is inferred from SEM images, as well as the experimental and history-matching work by Kang et al. (2011), which indicates that kerogen appears to be discontinuous at scales larger than tens of microns, and that the coupling between the organic and inorganic matrices is in series.

2. To present a Maxwell-Stefan formulation for the computation of the pressure- and composition-dependent diffusion coefficients in a multi-component system with more than two components.

3. To develop and implement a time-dependent shape factor to be used in the coupling term that describes the series transport of the multi-component shale gas from the kerogen into the inorganic matrix. This time-dependence of the coupling term was developed based on the time-dependent shape factor presented by (Zimmerman et al., 1993) for a dual-porosity matrix/fracture system. In this work, we focus on a dual-continuum matrix comprising of the inorganic and organic matrices.

4. To implement a modified form of the petrophysical model proposed by Ambrose et al. (2012) and Hartman et al. (2012). The petrophysical model from Ambrose et al. (2012) and Hartman et al. (2012) basically reduces the pore volume available for the storage of free gas in the shale matrix by the pore volume occupied by the adsorbed gas molecules. The modification in this work is to correct only the organic

pore volume (and not the total pore volume) by the volume occupied by the adsorbed gas molecules because we do not expect any significant adsorption in the inorganic pores.

5. To develop a fully-coupled model for the transport of multi-component gas in a deformable shale matrix. The stress-dependence of the matrix permeability will be modeled using the Gangi's model (Gangi, 1978), while the stress and time-dependence of the propped fracture conductivity will be modeled using an analytical viscoelastic model presented by Guo and Liu (2012).

6. To evaluate the potential of injecting and storing anthropogenic CO_2 in depleted organic-rich source rocks, using the numerical simulator developed.

2. LITERATURE REVIEW

2.1 The Multiscale Nature of the Shale Matrix

Oil and gas production from resource shale is characterized by a sharp decline. This decline is a manifestation of flow-regime transition from an early time, when the production is mainly due to flow in fractures, to a later period, when the matrix begins to contribute to the production. The extent of the early transient, which could be ephemeral, really depends on the presence of fractures and on the physical qualities (conductivity, spatial distribution, etc.) of the fracture network. The later period, on the other hand, could take large production times and is characterized by a long tail in production history plots. Its extent is controlled by the shale formation qualities. The latter observation and the desire to manipulate decline rates in shale-gas wells for optimum production has resulted in research interest on the shale matrix, in particular, its storage and transport mechanisms.

Recent investigations on petrophysical characterization of resource shales using scanning- and transmission-electron microscopy images have visually revealed the presence of multiple continua in the shale formation, consisting of the organic matrix also known as kerogen, the inorganic matrix (mainly consisting of clays, quartz, carbonate, pyrite, and feldspars), and the fractures (Loucks et al., 2009, 2012; Ambrose et al., 2012). Kerogen appears in 2D images (like Figure 2.1) as the finely-dispersed phase within the inorganic matrix at the sub-micron scale, or in 3D images (like Figure 2.2), as the continuous phase creating its own interconnected network intertwined with the inorganic matrix. Ambrose et al. (2012) presented 3D images at the micron-scale, using Barnett shale samples. An adapted version of the image is shown in Figure 2.2. Akkutlu and Fathi (2012) presented the first set of governing equations honoring these petrophysical observations to describe single-phase flow of gas in shale formation including this duality and coupling

of the organic-inorganic matrices. These equations included the contribution of molecular diffusion and surface diffusion in the shale formation. This was necessary, they argued, because the permeability of the shale matrix could be so low that other transport mechanisms could contribute to the overall transport significantly. Recent publications (Sun et al., 2015; Zhang et al., 2015; Akkutlu et al., 2016) on the numerical modeling of transport in shale-gas reservoirs now typically include surface diffusion and Knudsen diffusion in the kerogen pore network, in addition to molecular diffusion and convection in the kerogen/inorganic pore network. However, these publications typically ignore the dispersed nature of kerogen, as well as the dependence of the molecular diffusion coefficients on pressure and composition.

2.2 Numerical Modeling of Transport and Storage in Organic-rich Source Rocks

Several authors have developed numerical models that attempt to describe the storage and transport mechanicsms that are peculiar to organic-rich source rocks. Freeman et al. (2010) and Moridis et al. (2010) presented a detailed mathematical model and simulator

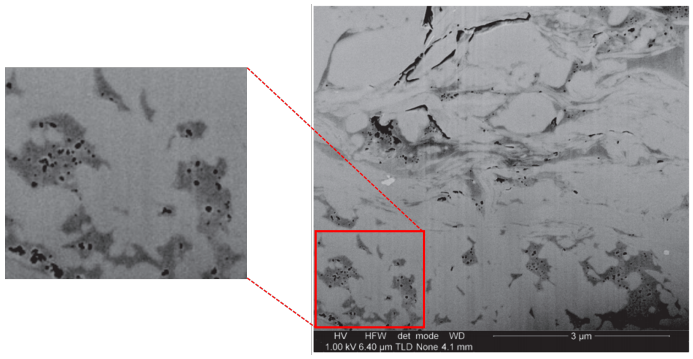

Figure 2.1: 2D focused-ion-beam/scanning-electron-microscope image of an organic-rich shale sample showing finely dispersed kerogen embedded in an inorganic matrix. In these images, black represents the pores, dark gray represents the kerogen matrix, and light gray represents the inorganic shale matrix. This image is adapted from Ambrose et al. (2012).

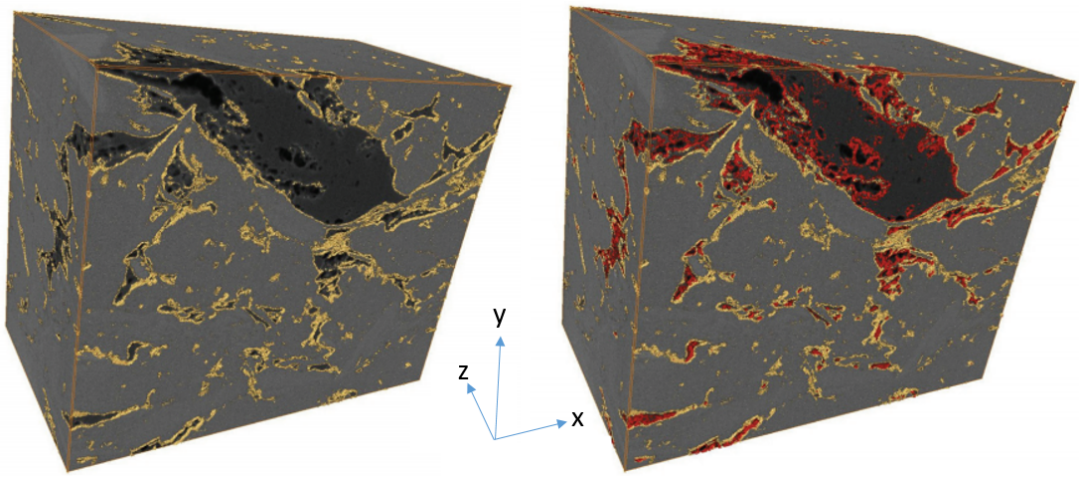

Figure 2.2: 3D SEM image of an organic-rich shale adapted from Ambrose et al. (2012). The sample has lengths of 5 μm, 4 μm, and 2.5 μm in the x, y, and z directions, respectively. LEFT: The kerogen network is shown with the yellow outlines. RIGHT: The kerogen network is also outlined in yellow, while the pore spaces are outlined in red.

for tight gas or shale gas reservoirs. Their model features an additional contribution of adsorbed gas molecules to the total storage in these unconventional gas reservoirs, using the Langmuir isotherm. Molecular effects were also considered and related to the Knudsen number. Ambrose et al. (2012) and Hartman et al. (2012) later indicated that adsorbed gas molecules actually occupy some pore volumes, and they presented a new petrophysical model that accounts for the reduction in the free pore volume, due to the presence of adsorbed gas molecules on the pore walls. Akkutlu and Fathi (2012) presented a mathematical model for organic-rich source-rocks that basically considered the natural fractures, organic and inorganic matrices as different continua. Several authors have also published some results on the modeling of fractured organic-rich source rocks with multiple continuum models (Sun et al., 2015; Zhang et al., 2015; Alfi et al., 2015; Akkutlu et al., 2016; Yan et al., 2016).

This work considers the dispersed nature of kerogen observed in SEM images, which was also indicated in the results of the experimental work by Kang et al. (2011). This, in

addition to the fact that the diffusive transport of fluids in the kerogen is expected to be much slower than the advective transport in the natural fractures and microcracks typically seen in the inorganic matrix, indicates that the continuous transport of gas in kerogen can be neglected at simulation scale. I therefore, present a model which allows the kerogen to contribute to transport by releasing gas into the inorganic matrix that is collocated in the same simulation cell, but disallows the continuous transport of gas from cell to cell at simulation scale. Hydraulic and natural fractures are modeled in this work using the Discrete Fracture Model (DFM). The model developed in this work is therefore simpler than the multiple continuum models with several coupling terms between the different continua because only a single coupling term (between the organic and inorganic matrix) needs to be considered explicitly. Furthermore, in contrast to all the publications I have seen in the literature, this work incorporates a petrophysical model that captures the expected reduction in the pore-volume available for free gas in the organic matrix, due to the pore-volume occupied by the gas molecules adsorbed on the organic pore walls. Olorode et al. (2017a) discussed the mathematical model described here within the context of a non-deformable matrix. In this work, a fully coupled geomechanics and compositional gas transport simulator is developed, validated and used to perform several numerical studies.

2.3 Modeling of Molecular Diffusion in Organic-rich Source Rocks

This work is motivated by the general consensus that molecular diffusion in the organic and inorganic matrices can contribute appreciably towards the production performance, and therefore, targets its detailed description in a petrophysical setting that is representative of organic-rich shale formations. Multi-component molecular diffusion theory, hereto referred to as the Maxwell-Stefan diffusion, states that diffusion is a function of pressure, temperature, and composition (Taylor and Krishna, 1993). Since it is common to assume that the shale-gas production process is isothermal, one can ignore the temperature-

dependence of diffusion. However, pressure is known to drop drastically near the fracture faces (and more gently further into the matrix) while the hydrocarbon fluid composition tends to evolve during production (Freeman et al., 2012). These changes in pressure and composition then imply that the diffusion coefficients are not constant.

Yi et al. (2008) introduced the Maxwell-Stefan diffusion to model transport of a binary gas mixture (CH_4-CO_2) in coals. Their interest was to investigate co- and counter-diffusion phenomena of the mixture components in the presence of adsorption with application into enhanced coalbed methane recovery. Hoteit and Firoozabadi (2009) and Hoteit (2011) discussed the proper modeling of the diffusion of multi-component fluids using the full tensor of the Maxwell-Stefan diffusion coefficient instead of just a single diffusion coefficient for each hydrocarbon component. They indicated that this could be important in tight reservoirs, where the matrix permeability values are much lower than in conventional reservoirs. Fathi and Akkutlu (2014) applied the binary Maxwell-Stefan diffusion model to simulate cyclic CO_2 stimulation in depleted shale-gas wells. However, I have not found any other published work showing the use of the Maxwell-Stefan diffusion theory to model the diffusive transport in organic-rich source rocks with more than two hydrocarbon components. This work presents a multi-component multi-continuum shale-gas model that captures the pressure- and composition- dependence of molecular diffusion coefficient using the Maxwell-Stefan diffusion model. According to this model, the diffusive transport introduces new and intricate non-linearities into our shale gas simulation problem, where the diffusion coefficient of each species needs to be computed in each representative elementary volume (or grid block in the numerical model) using the pressure and composition in the volume at the current time-step.

Additionally, I revisit and modify the Akkutlu-Fathi (2012) multi-continuum formulation to capture the discontinuous nature of kerogen. Even though the kerogen may create its own continuous phase in the inorganic matrix, the connectivity of the kerogen at a

larger scale could be still poor. In addition, molecular transport in the interconnected part of the kerogen pore network is relatively a slow process compared to flow of gas in the inorganic matrix. Consequently, it is reasonable to assume that kerogen is discontinuous at the reservoir scale. The next section gives more detailed argument for a discontinuous kerogen network at the scale of a typical reservoir simulation grid-block.

2.4 Modeling of Coupled Geomechanics and Multi-continuum Compositional Gas Transport

Several authors have developed multi-continuum models for the transport of reservoir fluids in non-deformable organic-rich source rocks (Sun et al., 2015; Zhang et al., 2015; Alfi et al., 2015; Akkutlu et al., 2016; Yan et al., 2016). A few authors have also published some work on the coupling of geomechanics with multi-continuum models (Duguid and Lee, 1977; Huyakorn and Pinder, 1983; Wilson and Aifantis, 1982; Valliappan and Khalili-Naghadeh, 1990; Bai et al., 1993). However, there appears to be much less work done in the area of coupling geomechanics with multi-continuum models in a compositional setting. One of these few publications includes Xiong et al. (2015), which involved coupling the geomechanical deformation of the matrix with the compositional flow model through the mean stress.

Chen and Teufel (1997) presented a consistent model for coupling geomechanics and flow simulation in double-porosity reservoirs. The model basically reduces to the single-porosity equivalence when one of the continua is diminished to zero porosity or when the pressure in both continua become equal. Chen and Teufel (2000) reviewed five models for coupled geomechanics and flow simulation in double porosity reservoirs and concluded that the Chen and Teufel (1997) model provides a consistent approach, while the other models are typically not consistent in the limit when the pressure in the two continua are equal, or when the volume fraction of any of the two continua vanishes. The other

models they reviewed include the models by Duguid and Lee (1977) and Huyakorn and Pinder (1983), Wilson and Aifantis (1982), Valliappan and Khalili-Naghadeh (1990) and Bai et al. (1993).

In this dissertation, I adapt the Chen and Teufel (1997) model to the transport of multi-component gas in a deformable shale matrix, which consists of the inorganic and organic matrices. Most of the previous publications on coupled geomechanics and flow simulation use the finite element method to discretize the linear momentum balance equation, and use a mass conservative scheme like the finite volume methods to discretize the mass balance equations. In this work, I used the Control-Volume Finite Element Method (CVFEM) as a natural discretization to solve the fully-coupled equations describing both the compositional gas transport and the mechanical deformation of the shale matrix.

2.5 The Control Volume Finite Element Method (CVFEM)

The Control Volume Finite Element Method (CVFEM) is a numerical discretization scheme that basically combines the advantages of the finite element method with the advantages of the finite volume method. It is locally conservative, like the finite volume methods, and like the finite element methods, it allows the flexibility of gridding with triangular or quadrilateral elements. Lemonnier (1979), Forsyth (1990), Fung et al. (1992), Chen et al. (2006), and others have demonstrated the use of the CVFEM to model fluid flow in petroleum reservoirs. Voller (2009) detailed the use of this method to model solid deformation and fluid flow. Cordazzo et al. (2003), (2005), and Hurtado et al. (2007) showed that the CVFEM can be improved by simply specifying porosity and permeability to be constant over each finite element (instead of having these properties specified at the nodes). This improved form of the CVFEM was shown to give lower truncation errors and better accuracy in the modeling of heterogeneities (Cordazzo et al., 2003). Eymard and Sonier (1994) showed some mathematical and numerical properties of the CVFEM. They

performed some numerical simulations and concluded that the CVFEM has several mathematical and numerical advantages over the conventional control volume finite difference method, and no disadvantages were reported.

The fact that all the primary variables are collocated at the nodes or vertices of the elements in the reservoir domain makes this method a good fit for the fully coupled discretization and solution of the equations describing the flow of multi-component reservoir fluids and the mechanical deformation of the reservoir matrix. Additionally, the geometrical quantities computed in the discretization of the mass balance equations are readily available for re-use in the discretization of the solid linear momentum balance equations. This makes it a relatively efficient numerical discretization procedure.

3. MATHEMATICAL MODEL FOR SIMULATING TRANSPORT IN ORGANIC-RICH SOURCE ROCKS

In this work, I present a model that strives to honor the major storage and transport mechanisms that could be expected in resource shales. Based on observations from SEM images (Figure 2.1 for example), I propose a model that captures the observation that kerogen is typically discontinuous and dispersed in the inorganic matrix at the micron scale. I present two different mathematical models, corresponding to the scenarios where the shale matrix is deformable[1], and when it is not deformable[2].

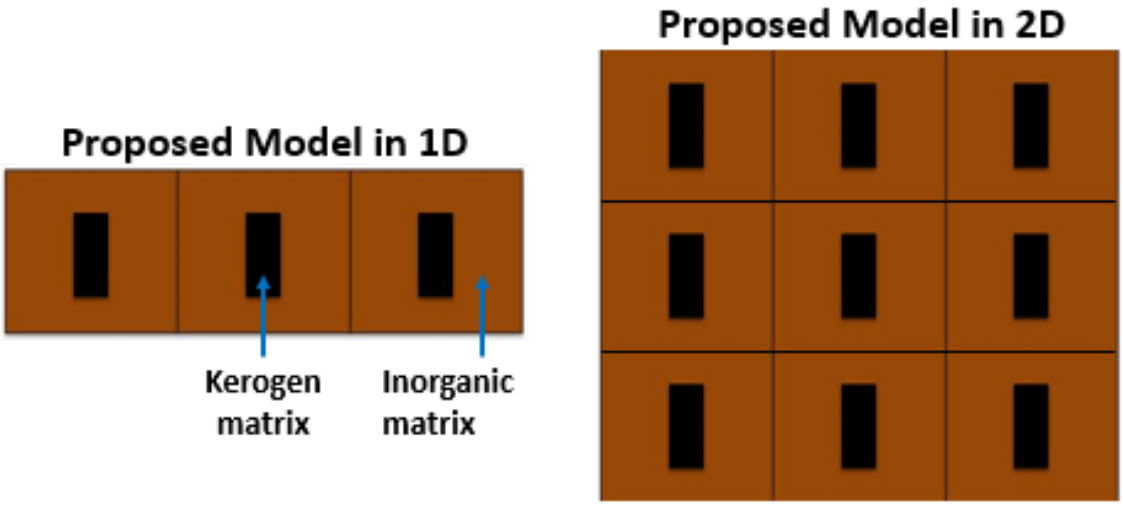

Figure 3.1: The proposed model captures the dispersed nature of kerogen in the inorganic matrix.

[1]Part of the model developed for deformable shales is reprinted with permission from "A Compositional Model for CO_2 Storage in Deformable Organic-Rich Shales" by O. M. Olorode, I. Y. Akkutlu, and Y. Efendiev, 2017. SPE Europec featured at 79th EAGE Conference, Copyright 2017 by SPE.

[2]Part of the model developed for non-deformable shales is reprinted with permission from "Compositional Reservoir-Flow Simulation for Organic-Rich Gas Shale" by O. M. Olorode, I. Y. Akkutlu, and Y. Efendiev, 2017. SPE Journal, Copyright 2017 by SPE.

Using gas permeation experiments and history-matching, Kang et al. (2011) showed that a large portion of injected gas reaches the organic pores through the inorganic pores. They pointed out that this is consistent with SEM images that do not show the connectivity of kerogen on scales larger than tens of microns, and they concluded that the coupling between the inorganic and organic matrices is in series. Given that the REV or reservoir simulation grid-block could easily be up to 5 orders of magnitude larger than SEM images, this work conjectures that these micron-scale "pockets" of kerogen will be discontinuous across the simulation grid blocks. I propose a model with an in-series coupling between the organic and inorganic matrices. Figure 3.1 gives a sketch of the proposed model in 1D and 2D. The figure shows that the kerogen in each grid block is not in direct hydraulic communication with the kerogen in the neighboring grid blocks. The sketch of the model clearly shows that the communication between the organic and inorganic pores are in series. The organic pores release reservoir fluids into the inorganic pores, which in turn release their fluids into the hydraulic and/or natural fractures in the reservoir. This work models both the hydraulic fractures (and discrete fracture networks if present) with the discrete fracture model, which is discussed in a later section.

The matrix of the organic-rich source rocks tend to deform as effective stresses build up during production. The Biot's effective stress is the difference between the total stress and the product of the Biot constant (α) and the pore pressure. Therefore, the effective stress in the vicinity of the fracture surface builts up rapidly as the pore pressure declines rapidly in this region. This effective closure stress could result in significant decrease in fracture aperture and conductivity, leading to a consequent decline in production. This work therefore sets out to study the production of multi-component gas in a deformable shale matrix. To clarify, this dissertation sometimes uses the term "shale(s)" to refer to all organic-rich source rocks, which could include mudrocks, carbonates, etc. The next section starts with a presentation of the mass balance equations for a non-deformable shale

matrix, while the following section extends this to the deformable case, where the coupled geomechanics and flow problem are discussed.

3.1 Mass Balance Equations for Multicomponent Gas in a Non-deformable Shale Matrix

The origin of the multi-component mass balance equations employed in this work could be traced to Akkutlu and Fathi (2012). Some of the specific modifications made in this work are as follows:

1. This work models the organic matrix as a dispersed and discontinuous continuum, as inferred from SEM images.

2. This work extends the developed formulation to a multi-component system, and uses the Maxwell-Stefan diffusion coefficient to capture the pressure-dependence of diffusion.

3. This work implements a modified form of the petrophysical model proposed by Ambrose et al. (2012) and Hartman et al. (2012). The modification made in this dissertation is to correct only the organic pore volume (and not the total pore volume) by the volume occupied by the adsorbed gas molecules because I do not expect significant adsorption in the inorganic pores.

3.1.1 Inorganic Mass Balance Equations for a Non-deformable Shale Matrix

The equation for the mass balance of the gas component in a non-deformable shale matrix is given as:

$$-\nabla \cdot J_i^I + \nabla \cdot \left(y_i^I c^I \frac{k_m}{\mu_g} \nabla p^I \right) + W_{OI}^i = \frac{\partial}{\partial t} \left[(1 - \epsilon_{kp}) \, \phi y_i^I c^I \right] \tag{3.1}$$

where:

$$J_i^I = -\left(1-\epsilon_{kp}\right)\frac{\phi}{\tau}\,D^i\nabla\left(c^I y_i^I\right) \tag{3.2}$$

and

$$W_{OI}^i = l_m^T\frac{\epsilon_{kf}\phi}{\tau}D^{i,O}\left(y_i^O c^O - y_i^I c^I\right) + \left(1-\phi\right)l_m^T D_s^i c_\mu^i + y_i^O\frac{l_m^T\,c^O\,k_m^O}{\mu_g^O}\left(p^O - p^I\right) \tag{3.3}$$

The three terms on the right-hand-side of Eq. 3.3 refer to the transfer of reservoir fluids from the organic to the inorganic matrix by molecular diffusion in the pores, surface diffusion, and advection, respectively. The second term in Eq. 3.3 has been written in terms of the adsorbed concentration in units of gram-mol per reservoir cubic meter of rock.

The adsorbed gas concentration of component, i can be obtained using the Extended Langmuir isotherm as follows:

$$c_\mu^i = \frac{c_{\mu s}^i y_i^O p^O/p_L^i}{1+\sum_{j=1}^{n_c}\left(y_i^O p^O/p_L^i\right)} \tag{3.4}$$

If the maximum adsorbed gas amount is specified in scf/ton, I can convert this value into the corresponding maximum adsorbed concentration in mol/r·m^3 using the equation:

$$c_{\mu_s} = G_{sL}\,\rho_{ma}\left(\frac{n}{V}\right)_{sc}\left(\frac{1\,ton}{907,185\,g}\right)\left(\frac{1\,sm^3}{3.28084^3\,scf}\right) \tag{3.5}$$

The term "$\epsilon_{kf}\phi$" in Eq. 3.3 represents the ratio of the organic free-gas pore volume to the bulk volume. This concept is based on the petrophysical model presented by Ambrose et al. (2012), where the authors presented a model to account for the pore volume occupied by gas molecules adsorbed on the organic pore walls. Their model corrected the effective porosity (ratio of the total pore volume of connected pores to the bulk volume) in shale by subtracting the adsorbed porosity (ratio of the volume occupied by the adsorbed gas to the

bulk volume) from the effective porosity. This work extends their petrophysical model to implement the adsorbed-gas porosity-correction only in the organic pores. This is because virtually all of the adsorbed gases are expected to reside in the organic nanopores with large internal surface areas. I therefore keep the pore volume for free gases in the inorganic pores unchanged, but modify the pore volume available for free gas in kerogen, to account for the space taken up by the adsorbed gas. The free organic porosity (that is, organic pore volume available for free gas divided by bulk volume), $\epsilon_{kf}\phi$ can be obtained by first computing the adsorbed porosity, ϕ_a using Equation (A-4) from Ambrose et al. (2012) which is given as:

$$\phi_a = 1.318x10^{-6} M \frac{\rho_b}{\rho_s} \left(G_{sL} \frac{p}{p + p_L} \right) \tag{3.6}$$

I can write the total organic porosity, $\phi\epsilon_{kp}$ as the sum of the adsorbed porosity $\phi\epsilon_{ka}$ and the free organic porosity $\phi\epsilon_{kf}$:

$$\phi\epsilon_{kp} = \phi\epsilon_{ka} + \phi\epsilon_{kf} \tag{3.7}$$

This implies that $\epsilon_{kp} = \epsilon_{ka} + \epsilon_{kf}$, where ϵ_{kp} is the ratio of the kerogen pore volume to the total pore volume, ϵ_{ka} is the ratio of the adsorbed pore volume to the total pore volume and ϵ_{kf} is the ratio of the free kerogen pore volume to the total pore volume. So, to obtain ϵ_{kf}, I compute ϕ_a using Eq. 3.6, divide ϕ_a by ϕ to obtain ϵ_{ka}, then subtract ϵ_{ka} from ϵ_{kp} to obtain ϵ_{kf}.

In Eq. 3.2, I can substitute the definition for effective diffusivity as a function of porosity and tortuosity. This widely used definition for effective diffusivity comes from the Bruggeman equation:

$$D_{eff} = \frac{\phi}{\tau} D^i \tag{3.8}$$

where ϕ is the total porosity. D^i is the Maxwell-Stefan diffusion coefficient which will

be discussed in the next chapter. Tortuosity, τ is defined as the ratio of the actual length of the flow path in the inorganic matrix to the thickness of the porous medium in the flow direction.

Hu et al. (2015) reported overall tortuosity values ranging from 2 to 12 for some Barnett shale samples. They explained that these high values could be as a result of the poor connectivity in shale formations. In this work, I note that in addition to the poor connectivity, the presence of dispersed kerogen in shales could act as barriers to the continuous fluid transport that would have been expected if the resource shale had larger inorganic pores instead of the organic nanopores.

Although Eq. 3.2 and Eq. 3.3 are written with subscripts i, the products of the diffusion coefficients and the mole fractions are evaluated by taking the matrix-vector product of the Maxwell-Stefan diffusion coefficient matrix and the vector of the mole fractions. This is also how I compute the products of the diffusion coefficients and the mole-fraction gradients.

The mass balance equation for the total mass of the hydrocarbons in the inorganic matrix is given as:

$$-\sum_{i=1}^{n_c} \nabla \cdot J_i^I + \nabla \cdot \left(c^I \frac{k_m}{\mu_g} \nabla p^I \right) + \sum_{i=1}^{n_c} W_{OI}^i = \frac{\partial}{\partial t} \left[(1 - \epsilon_{kp}) \, \phi c^I \right] \tag{3.9}$$

The first term on the left-hand-side represents the molecular diffusion of all the hydrocarbon components. To obtain this value, I simply sum the molecular diffusion of each of the hydrocarbon components given in Eq. 3.2. Since the Maxwell-Stefan diffusion coefficients are computed for $n_c - 1$ components, and relative to the diffusion of the heaviest component, the diffusion of the heaviest component relative to itself is zero, and the sum of the diffusion of all the components defined in this manner is not zero (Taylor and Krishna, 1993). The physical interpretation of this is that the hydrocarbon components are

able to diffuse towards a fractured well in an ultra-low permeability reservoir, and the sum of the molecular diffusion fluxes of each component in each grid-block is not zero in this case. The section on Maxwell-Stefan diffusion gives more details on the computation of the coefficients.

Given that the Maxwell-Stefan diffusion coefficient matrix has a dimension of $(n_c - 1)$ x $(n_c - 1)$, Eq. 3.1 is for the first $n_c - 1$ components of the gas. To obtain the last equation to complete the model, I wrote Eq. 3.9 for the total mass of hydrocarbon instead of the equation for the last hydrocarbon component, n_c. Cao (2002) gives more details on this numerical modeling approach, but it is worth mentioning that I now have n_c inorganic mass balance equations in terms of n_c unknowns– $p^I, y_1, y_2, ..., y_{n_c-1}$.

In this work, gas viscosity, μ_g is computed using the Lee et al. (1966) correlation, while the gas compressibility factor, Z, is computed using the Peng-Robinson Equation of State (Peng and Robinson, 1976). This Z-factor is then substituted into the Real-Gas Equation to obtain the gas molar density, c^I.

3.1.2 Organic Mass Balance Equations for a Non-deformable Shale Matrix

The equation for the mass balance of gas component, i in the organic pores is given as:

$$-W_{OI}^i = \frac{\partial}{\partial t}\left[\epsilon_{kf}\phi y_i^O c^O + (1-\phi)\, c_\mu^i\right] \tag{3.10}$$

The diffusive and advective transport mechanisms (that were modeled in the inorganic mass balance equations) are neglected in the organic matrix. This is based on the in-series model that assumes that the organic matter (or kerogen) in shales are not expected to be continuous over the typical sizes of reservoir simulation grid-blocks, as explained in the section on the proposed multi-continuum model.

The mass balance equation for the total mass of hydrocarbons in the organic pores

could be written as:

$$-\sum_{i=1}^{n_c} W_{OI}^i = \frac{\partial}{\partial t}\left[\epsilon_{kf}\phi c^O + (1-\phi)\sum_{i=1}^{n_c} c_\mu^i\right] \tag{3.11}$$

The organic mass balance equations add another n_c equations and n_c unknowns, so the total number of equations and unknowns is $2n_c$. The unknowns or primary variables are: $p^I, y_1^I, y_2^I, ..., y_{n_c-1}^I, p^O, y_1^O, y_2^O, ..., y_{n_c-1}^O$.

3.2 Transient Coupling Between the Organic and Inorganic Components of Shale

Given that the dispersed kerogen model presented in this work allows the organic matrix to contribute to transport only through its coupling with the inorganic matrix, it is important to accurately estimate the parameters in this coupling term. This section focusses on the estimation of the transient shape factor, l_m^T.

Kazemi et al. (1992) presented an equation for estimating the shape factor for any geometry, in a dual-porosity model. The shape factor, as shown in Eq. 3.12, is estimated based on the volume of the matrix block, the surface open to flow in all directions, and the distances between these surfaces and the center of the matrix block.

$$\sigma_{PSS} = \frac{1}{V}\sum_{i=1}^{n}\frac{A_i}{d_i} \tag{3.12}$$

where σ_{PSS} is the pseudo-steady-state shape factor, V is the volume of the matrix block, A_i is the area of each surface, i of the matrix block, d_i is the distance between the center of the matrix block and each surface, i, and n is the total number of surfaces of the matrix block. Heinemann and Mittermeir (2012) re-derived Eq. 3.12 and concluded that the equation is exact at pseudo-steady-state flow conditions in dual-porosity systems.

In this work, instead of the matrix and fracture continua, I model the organic and

inorganic continua. This implies that V, A_i and d_i in Eq. 3.12 are for kerogen (instead of the matrix, in a dual-porosity system). The kerogen bulk volume can be easily estimated from ϕ, ϵ_{kp} and ϵ_{ks}, as shown in Appendix A. The corresponding equation for the kerogen pseudo-steady-state shape factor, l_m^{PSS} is given as:

$$l_m^{PSS} = \frac{1}{V^k} \sum_{i=1}^{n} \frac{A_i^k}{d_i^k} \tag{3.13}$$

where the superscript, k indicates that these geometric parameters are for the kerogen matrix.

Given the ultra-low permeability of shale, coupled with molecular and surface diffusion in the organic matrix, I do not expect resource shales to reach a pseudo-steady state within the typical productive life of these unconventional resources. However, this implies a need to account for transient flow/transport in shales.

Although, any geometry of kerogen can be modeled, I can simplify the model by assuming that the dispersed kerogen has an approximate shape (like a sphere, cube, cuboid, hexahedra, tetrahedra, etc). Assuming that the approximate geometry of the kerogen is a sphere, and substituting the equations for the volume and total surface area of a sphere into Eq. 3.13, yields:

$$l_m^{PSS} = \frac{3}{r_k^2} \tag{3.14}$$

Making the radius, r_k the subject of the equation for the volume of a sphere, I obtain $r_k = (3V^k/4\pi)^{1/3}$. Introducing V_b^k as the kerogen bulk volume, and substituting the expression for the radius of a sphere into Eq. 3.14 yields:

$$l_m^{PSS} = \frac{3}{\left(3V_b^k/4\pi\right)^{2/3}} \approx 7.8 \left(V_b^k\right)^{-2/3} \tag{3.15}$$

In a similar fashion, I can substitute the equations for the volume, area and the distance

to the centroid of a cube into Eq. 3.13. After making the length of a side of the cube the subject of the equation for its volume, I obtain:

$$l_m^{PSS} = 12\left(V_b^k\right)^{-2/3} \tag{3.16}$$

This approach can be extended to different geometries and presented in the following generic form:

$$l_m^{PSS} = \mathcal{G}_A * \left(V_b^k\right)^{-2/3} \tag{3.17}$$

where $\mathcal{G}_A$ is a geometric factor. So, for a sphere, $\mathcal{G}_A \approx 7.8$ and for a cube, $\mathcal{G}_A$ = 12. Appendix B gives examples of the computation of the geometric factor for some geometries. However, given that it is unrealistic to obtain the exact geometry for all the organic matter in a given shale resource, this parameter is recommended to be used as a history-matching parameter, instead of the transient or pseudo-steady-state shape factor, as is customarily done in dual-porosity reservoir modeling.

This work recognizes the fact that pseudo-steady-state flow is not expected during the typical productive life of shale-gas reservoirs. Therefore, in the coupling term, I use a model based on the Zimmerman transient shape factor (Zimmerman et al., 1993) instead of the Warren-Root pseudo-steady-state shape factor (Warren and Root, 1963). Azom and Javadpour (2012) applied the Zimmerman transient shape factor in terms of pseudo-pressures, while Lu et al. (2008) applied it in terms of concentration (or molar density). In this work, I write the simplified expression for the transient shape factor, presented by Azom and Javadpour (2012), in terms of concentration as follows:

$$l_m^T = \frac{2c_i^O - \left(c_i^O - c^I\right)}{2\left(c_i^O - c^O\right)} l_m^{PSS} \tag{3.18}$$

Here, c_i^O refers to the value of the organic concentration (or molar density) at initial condi-

tions. In order to clearly show that this equation approaches the pseudo-steady-state shape factor when c^O tends to c^I, I simplify the equation further, by expanding the numerator and separating out the two fractions to obtain:

$$l_m^T = \left(0.5 + 0.5\frac{c_i^O - c^I}{c_i^O - c^O}\right) l_m^{PSS} \tag{3.19}$$

I define a transient factor, $\mathcal{T}_f$ to be equal to the bracketed term on the right-hand-side, that is:

$$\mathcal{T}_f = \left(0.5 + 0.5\frac{c_i^O - c^I}{c_i^O - c^O}\right) \tag{3.20}$$

Substituting this as well as Eq. 3.17 into Eq. 3.19 yields:

$$l_m^T = \mathcal{G}_A \mathcal{T}_f \left(V_b^k\right)^{-2/3} \tag{3.21}$$

As demonstrated by Zimmerman et al. (1993), the transient coupling term captures the correct scaling of the matrix pressure (in this case, organic gas concentration) with the square root of time ($t^{1/2}$), while the corresponding pseudo-steady-state coupling term scales incorrectly with time (t). For this reason, the use of the shape-factor as a constant history-matching parameter could be erroneous. The pseudo-steady-state shape factor (and consequently the transient shape factor) for each grid-block, as shown in Eq. 3.13, is a function of its corresponding volume. Therefore, the use of a constant shape-factor in all the grid blocks of a numerical model with varying grid-block sizes could lead to significant errors in the coupling term. This error could be further magnified in models with grid refinements, where the smallest cells could be orders of magnitude smaller than the largest ones.

It is important to note that the remarks on shape factors in this section are also applicable in conventional dual-porosity systems.

3.3 Maxwell-Stefan Diffusion Theory for the Computation of Composition and Pressure-dependent Diffusivity

Most of the published works on molecular diffusion in porous media assume a constant effective diffusion coefficient for each of the hydrocarbon components (Wasaki and Akkutlu, 2015; Sun et al., 2015; Xiong et al., 2015). In this work, I note that the kinetic theory of gases indicates that the diffusion coefficient is inversely proportional to pressure. This implies that the diffusion coefficients for an Eagle Ford shale-gas reservoir with a pressure of about 11,400 psi (Orangi et al., 2011) could be as little as about 35% of that for a Barnett shale-gas reservoir with a pressure of about 4,000 psi (provided that the mole-fractions of the hydrocarbon components are not too different). The use of the Maxwell-Stefan diffusion coefficient provides a means to estimate the diffusion coefficient for any reservoir, given its pressure and gas composition. This enables the modeling of the dependence of diffusion on pressure and composition. Taylor and Krishna (1993) noted that the Maxwell-Stefan diffusion is capable of modeling osmotic diffusion, reverse diffusion, and diffusion at a diffusion barrier, while the Fickian diffusion, as well as the effective diffusion model could be limited in these cases. This work uses the Generalized Maxwell-Stefan Diffusion Equation (GMSE) to estimate the diffusion coefficient for the hydrocarbon components in an open medium. The corrections for a tortuous porous medium were explained in the previous section.

Details on the theory and some applications can be found in Taylor and Krishna (1993). Below, I simply give the final form of the Maxwell-Stefan diffusion equation:

$$J = -c\,\mathcal{B}^{-1}\,\Gamma\,\nabla \mathbf{y} \tag{3.22}$$

Comparing this equation to Fick's law for diffusion, I can obtain a Fickian-type matrix of

coefficients for the Maxwell-Stefan equation. That is,

$$D = \mathcal{B}^{-1}\,\Gamma \tag{3.23}$$

The equations to obtain the drag matrix, $\mathcal{B}$ are given by Taylor and Krishna (1993):

$$\begin{aligned} \mathcal{B}_{ii} &= \frac{y_i^I}{D_{in}} + \sum_{k=1;\ i\neq k}^{n} \frac{y_k}{D_{ik}} \\ \mathcal{B}_{ij} &= -y_i^I \left(\frac{1}{D_{ij}} - \frac{1}{D_{in}}\right) \end{aligned} \tag{3.24}$$

where D_{ij}, D_{in} and D_{ik} are the Maxwell-Stefan diffusion coefficient for any pair of components, and can be obtained from the kinetic theory of gases. In this work, I use the Fuller et al. (1966) correlation, which is based on the kinetic theory of gases. The parameters for this correlation are readily available in Fuller et al. (1969), and this correlation is recommended by Danner and Daubert (1983), and by Reid et al. (1987).

The equation for the thermodynamic factor is given by Walas (1985):

$$\Gamma_{ij} = \delta_{ij} + y_i^I \frac{\partial\, ln\ \Phi_i}{\partial y_j}|_{T,P,\Sigma} \tag{3.25}$$

where Φ in this equation represents the fugacity coefficient, while the subscript Σ indicates that the differentiation of $ln\ \Phi_i$ with respect to mole fraction, y_j should be performed such that the mole fractions of all other components are kept constant, except the nth. The fugacity coefficient is computed using the Peng-Robinson Equation of state (Peng and Robinson, 1976).

It is important to note that the equations for $\mathcal{B}$ given above assume that the sum of the molecular diffusion fluxes of each component is equal to zero. If instead, I define the molecular diffusion relative to the heaviest component in the mixture, n_c, the molecular

diffusion flux of that component will be zero, while the sum of all the other $n_c - 1$ components will be non-zero. To obtain the corresponding $\mathcal{B}$ in this case, I use the modified equation from Taylor and Krishna (1993) :

$$\begin{aligned} \mathcal{B}_{ii}^{n_c} &= \sum_{k=1;\ i \neq k}^{n} \frac{y_k}{D_{ik}} \\ \mathcal{B}_{ij}^{n_c} &= -\frac{y_i^I}{D_{ij}} \end{aligned} \tag{3.26}$$

The equations presented for the computation of the Maxwell-Stefan diffusion coefficient were programmed and validated against several examples given in Taylor and Krishna (1993). Using mole fraction values that could be representative of Barnett shale gas composition, I computed the 2x2 matrix of diffusion coefficients (for a three-component system) at different pressures, ranging from 12,000 to 2,000 psi. Each element of this matrix of diffusion coefficients is then plotted against pressure in Figure 3.2a. The plot shows that the diffusion coefficients increase as the pressure drops. To confirm whether the matrix of diffusion coefficients are strictly inversely proportional to pressure, I plot these diffusion coefficients against the inverse of pressure. The dotted lines shown in Figure 3.2b show rough estimates of the diffusion coefficients assuming a strictly inverse proportionality with respect to pressure, while the solid lines are the results obtained using the code developed based on the rigorous procedure described in this section. The figure shows that this rough approximation could be acceptable given the considerable computational efficiency of this approximation in comparison to the rigorous computation of the diffusion coefficients at each Newton iteration and simulation time-step. It is worth noting that although the kinetic theory of gases and the Fuller's correlation (Fuller et al., 1966) show that the binary diffusion coefficients are strictly inversely proportional to pressure, the deviation of the matrix of diffusion coefficients from this strict proportionality comes from the non-

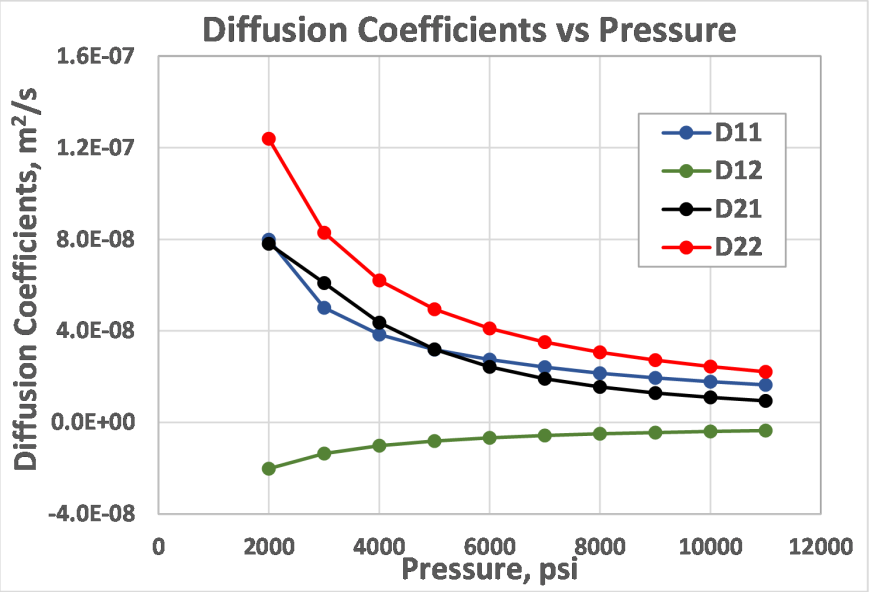

(a) The diffusion coefficient shows a nonlinear relationship with pressure. It increases as the reservoir pressure drops in response to production.

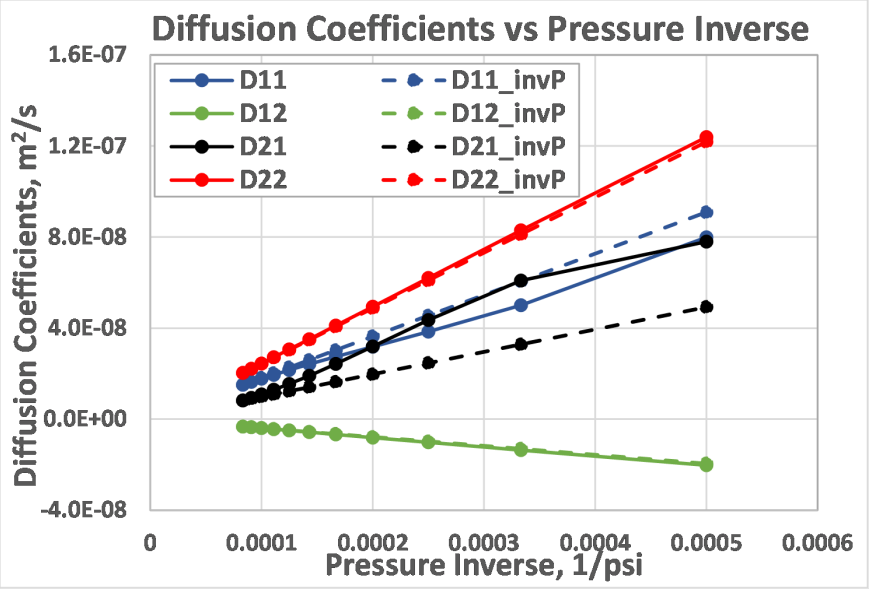

(b) The relatively close proximity of the dotted lines to the solid lines suggests that the diffusion coefficient is roughly inversely proportional to pressure.

Figure 3.2: The diffusion coefficient plots show a strong dependence of the diffusion coefficient on pressure.

linear dependence of the thermodynamic factor, Γ on pressure. Recall that the matrix of diffusion coefficients is a matrix multiplication of the inverse of the drag matrix, $\mathcal{B}$, and the thermodynamic factor, Γ.

The change in the Maxwell-Stefan diffusion coefficients in response to a change in composition (during production) was less than 4% on the diagonal terms. The mole fractions were varied within the range that was observed during the simulation runs, and the diffusion coefficients were computed at 12,000 psi and 2,000 psi. The greatest change in the matrix of diffusion coefficients ($<$29%) was on the second row, first column, while the other off-diagonal element was less than 9%. Comparing these changes in diffusion coefficient to the changes in response to pressure drop, the composition-dependence of the Maxwell-Stefan diffusion coefficients could be neglected in exchange for improved computational efficiency in systems under primary production.

Given that permeability is expected to decrease as pressure decreases during production, I can infer that the contribution of molecular diffusion to production in these ultra-low permeability reservoirs could be more significant, particularly in high-pressure shale reservoirs where I expect a large drop in pressure from the initial reservoir pressure to the flowing bottomhole pressure.

3.4 Mass Balance Equations for Multi-component Gas in a Deformable Shale Matrix

This section provides the mass balance equations for each of the gas hydrocarbon components in the inorganic and organic matrices, which are modeled as deformable continua. The modeling of the fully-coupled geomechanics and multi-component gas transport involves modifying the accumulation term to include the change in accumulation due to the deformation of the matrix. An additional equation is also introduced to model the linear elastic deformation of the matrix. Considering that the transport terms in the mass balance

equations presented in Section 3.1 remain unchanged (in the Lagrangian description of poroelasticity), only the accumulation terms are modified.

3.4.1 Inorganic Mass Balance Equations for a Deformable Shale Matrix

By making analogy to the Chen and Teufel (1997) dual-porosity model for a deformable matrix/fracture system, the equation for the mass balance of each gas component in the deformable inorganic matrix could be written as:

$$-\nabla \cdot J_i^I + \nabla \cdot \left(y_i^I c^I \frac{k_m}{\mu} \nabla p^I \right) + W_{OI}^i = y_i^I c^I b_{11} \frac{\partial p^I}{\partial t} + y_i^I c^I b_{12} \frac{\partial p^O}{\partial t} + y_i^I c^I b_{13} \frac{\partial \epsilon_v}{\partial t} \tag{3.27}$$

where:

$$J_i^I = -\left(1 - \epsilon_{kp}\right) \frac{\phi}{\tau} D^i \nabla \left(c^I y_i^I \right) \tag{3.28}$$

and

$$W_{OI}^i = l_m \frac{\epsilon_{kp} \phi}{\tau_k} D^{i,O} \left(y_i^O c^O - y_i^I c^I \right) + \epsilon_{ks} \left(1 - \phi\right) l_m D_s^i \left(\frac{c_{\mu s}^i y_i^O p_G^O / p_L^i}{1 + \sum_{j=1}^{n_c} \left(y_i^O p_G^O / p_L^i \right)} \right) + y_i^O \frac{l_m \, c^O \, k_m^O}{\mu_g^O} \left(p^O - p^I \right) \tag{3.29}$$

The superscripts "I" and "O" refer to the inorganic and organic matrices, respectively. The inorganic porosity is given as: $\phi^I = \left(1 - \epsilon_{kp}\right) \phi$ while the organic porosity, $\phi^O = \epsilon_{kp} \phi$. ϵ_v represents the volumetric strain, while the terms b_{11}, b_{12} and b_{13} are analogous to those defined in Chen and Teufel (1997), with a modification of the porosity to reflect the

corresponding porosity of the inorganic and organic matrices.

$$\begin{aligned} b_{11} &= \phi\left(1-\epsilon_{kp}\right)\left[c_p^I\left(\beta^I-\alpha^I\right)+\frac{1}{K_g^I}\right] \\ b_{12} &= \phi\left(1-\epsilon_{kp}\right)c_p^I\left(\beta^O-\alpha^O\right) \\ b_{13} &= \frac{\phi\left(1-\epsilon_{kp}\right)c_p^I}{c_b} \end{aligned} \tag{3.30}$$

where K is bulk modulus, which is equivalent to the inverse of compressibility, and c_p and c_b refer to the pore and bulk compressibilities, respectively.

3.4.2 Organic Mass Balance Equations for a Deformable Shale Matrix

Similarly, the equation for the mass balance of the gas component, i in the organic pores could be written as:

$$-W_{OI}^i = y_i^O c^O b_{21}\frac{\partial p^I}{\partial t} + y_i^O c^O b_{22}\frac{\partial p^O}{\partial t} + y_i^O c^O b_{23}\frac{\partial \epsilon_v}{\partial t} + (1-\phi)\frac{Dc_\mu^i}{Dt} \tag{3.31}$$

The terms b_{21}, b_{22} and b_{23} are also defined as in Eq. 3.30:

$$\begin{aligned} b_{21} &= \phi\epsilon_{kp}c_p^O\left(\beta^I-\alpha^I\right) \\ b_{22} &= \phi\epsilon_{kp}\left[c_p^O\left(\beta^O-\alpha^O\right)+\frac{1}{K_g^O}\right] \\ b_{23} &= \frac{\phi\epsilon_{kp}c_p^O}{c_b} \end{aligned} \tag{3.32}$$

The parameters in equations 3.30 and 3.32 can also be derived from analogous parameters in Chen and Teufel (1997), and are given as:

$$\alpha^I = \alpha^* \frac{c_b^*}{c_b} \qquad \alpha^O = \alpha \left(1 - \frac{\alpha^* c_b^*}{\alpha c_b}\right)$$

$$\beta^I = \beta^* \frac{c_p^*}{c_p} \qquad \beta^O = \beta \left(1 - \frac{\beta^* c_p^*}{\beta c_p}\right) \tag{3.33}$$

$$c_p^I = \frac{\phi}{\phi\left(1 - \epsilon_{kp}\right)} c_p^* \qquad c_p^O = \frac{\phi}{\phi \epsilon_{kp}} c_p \left(1 - \frac{c_p^*}{c_p}\right)$$

The parameters with the asterisks are the parameters for a single-continuum shale matrix with no kerogen, while the corresponding parameters without the asterisks are for the dual-continuum shale matrix with both organic and inorganic matrices. These equations could provide a consistent estimation of the inorganic and organic matrix parameters to be used in a dual-continuum model, based on estimates of the corresponding parameters for a shale matrix without the organic pores, and for the shale matrix with the organic pores.

Equations 3.27 and 3.31 are written in the Lagrangian form, where the transport of the hydrocarbon components are specified relative to the initial description of the solid skeleton of the porous medium. Section 3.1 discusses the details of these equations for a non-deformable shale matrix, and the extension of this model to the case where the matrix is deformable provides a coupled geomechanics and flow model that dynamically accounts for the change in free pore volume as pressure is reduced during production, as well as the change in the total pore volume due to the geomechanical deformation of the porous medium.

3.5 Solid Momentum Balance Equation

The linear momentum balance equation is given as:

$$\nabla \cdot \sigma = 0 \tag{3.34}$$

where σ is the total stress, which can be decomposed in terms of the effective stress and pore pressure as follows:

$$\sigma = \sigma' - \alpha^I p^I \mathbf{I} - \alpha^O p^O \mathbf{I} \tag{3.35}$$

σ' is the effective stress, I is the identity matrix, α^O and α^I are the Biot coefficients for the organic and inorganic matrices, respectively. The negative sign of the pore pressure terms is based on the convention that compressive stresses are considered negative.

The Generalized Hooke's Law will be used as the constitutive equation to relate stress and strain. This equation is given as:

$$\sigma'_{ij} = C_{ijkl} : \epsilon_{kl} \tag{3.36}$$

where C is a fourth-order stiffness tensor, and ϵ is the second-order strain tensor.

For an isotropic porous medium, the Generalized Hooke's law for the effective strain can be written as:

$$\sigma' = 2G\epsilon_{ij} + \lambda\epsilon_v \mathbf{I} \tag{3.37}$$

Here, λ and G are the first and second Lame's constants, respectively. G is also called the shear modulus. Substituting Eq. 3.37 into Eq. 3.35 and integrating over a control volume, Ω gives:

$$\int_\Omega \nabla \cdot \left(2G\epsilon_{ij} + \lambda\epsilon_v \mathbf{I} - \alpha^I p^I \mathbf{I} - \alpha^O p^O \mathbf{I}\right) \, \mathrm{d}\Omega = 0 \tag{3.38}$$

Given that integration is a linear operator, I can separate the effective stress from the pore-

pressure terms, and then apply the Gauss divergence theorem to the effective stress term to obtain:

$$\int_S (2G\epsilon_{ij} + \lambda\epsilon_v \mathbf{I}) \cdot \mathbf{n}\, \mathrm{d}S - \int_\Omega \nabla \cdot \left(\alpha^I p^I \mathbf{I} + \alpha^O p^O \mathbf{I}\right)\, \mathrm{d}\Omega = 0 \tag{3.39}$$

Substituting the expressions for λ, G, ϵ_{ij} and ϵ_v, I can express Eq. 3.39 in 2D as follows:

$$\begin{aligned}\int_S \left[\frac{E}{1-\nu^2}\left(\frac{\partial u_x}{\partial x} + \nu\frac{\partial u_y}{\partial y}\right)\right] \cdot \mathbf{n_x} + \left[\frac{E}{2\,(1+\nu)}\left(\frac{\partial u_y}{\partial x} + \frac{\partial u_x}{\partial y}\right)\right] \cdot \mathbf{n_y}\, \mathrm{d}S \\ - \int_\Omega \left(\alpha^I \frac{\partial p^I}{\partial x} + \alpha^O \frac{\partial p^O}{\partial x}\right)\, \mathrm{d}\Omega = 0\end{aligned} \tag{3.40}$$

$$\begin{aligned}\int_S \left[\frac{E}{2\,(1+\nu)}\left(\frac{\partial u_y}{\partial x} + \frac{\partial u_x}{\partial y}\right)\right] \cdot \mathbf{n_x} + \left[\frac{E}{1-\nu^2}\left(\nu\frac{\partial u_x}{\partial x} + \frac{\partial u_y}{\partial y}\right)\right] \cdot \mathbf{n_y}\, \mathrm{d}S \\ - \int_\Omega \left(\alpha^I \frac{\partial p^I}{\partial y} + \alpha^O \frac{\partial p^O}{\partial y}\right)\, \mathrm{d}\Omega = 0\end{aligned} \tag{3.41}$$

3.6 Simplifications for compositional gas flow in deformable shale-gas reservoirs

Considering that this work focusses on the numerical modeling of multi-component gas in a deformable porous medium, it is reasonable to assume that the compressibility of the gas phase will be orders of magnitude larger than that of the shale matrix. This suggests that I can neglect the compressibility of the solid grain, and obtain simplified expressions for the parameters in equations 3.30, 3.32 and 3.33 as follows:

$$\begin{gathered} b_{11} = \phi^I \frac{1}{K_g^I}; \qquad b_{12} = b_{21} = 0 \\ b_{13} = \frac{c_b^*}{c_b}; \qquad b_{22} = \phi_f^O \frac{1}{K_g^O}; \qquad b_{23} = 1 - \frac{c_b^*}{c_b} \end{gathered} \tag{3.42}$$

$$\alpha^I = \beta^I = \frac{c_b^*}{c_b}; \qquad \alpha^O = \beta^O = 1 - \frac{c_b^*}{c_b}$$

$$c_p^I = \frac{c_b^*}{\phi^I}; \qquad c_p^O = \frac{c_b - c_b^*}{\phi_f^O} \tag{3.43}$$

Substituting these parameters into equations 3.27 and 3.31 yields:

$$-\nabla \cdot J_i^I + \nabla \cdot \left(y_i^I c^I \frac{k_m}{\mu} \nabla p^I \right) + W_{OI}^i = \phi^I \frac{1}{K_g^I} y_i^I c^I \frac{\partial p^I}{\partial t} + y_i^I c^I b_{13} \frac{\partial \epsilon_v}{\partial t} \tag{3.44}$$

$$-W_{OI}^i = \phi_f^O \frac{1}{K_g^O} y_i^O c^O \frac{\partial p^O}{\partial t} + y_i^O c^O b_{23} \frac{\partial \epsilon_v}{\partial t} + (1 - \phi) \frac{D c_\mu^i}{Dt} \tag{3.45}$$

Given that the total organic content (TOC) of resource shales are generally less than 12%, the contribution of the organic matrix to the bulk volume of the shale matrix is very small in comparison to the contribution of the inorganic matrix. Furthermore, the assumption that the kerogen is discontinuous and dispersed within the inorganic matrix indicates that its mechanical contribution to the deformation of the shale matrix could be limited. The lower depletion of the organic pore pressures (in comparison to the inorganic pore pressures) also indicates that the contribution of the organic matrix to the effective stresses induced during production could be limited. Based on these premises, Equations 3.44 and 3.45 could be further simplified such that the mechanical deformation of the shale matrix is controlled by the mechanical properties of the inorganic matrix only. Eq. 3.44 therefore simplifies to:

$$-\nabla \cdot J_i^I + \nabla \cdot \left(y_i^I c^I \frac{k_m}{\mu} \nabla p^I \right) + W_{OI}^i = \phi^I \frac{1}{K_g^I} y_i^I c^I \frac{\partial p^I}{\partial t} + \phi^I y_i^I c^I \alpha^I \frac{\partial \epsilon_v}{\partial t} \tag{3.46}$$

Eq. 3.45 on the other hand yields:

$$-W_{OI}^{i} = \phi_f^O \frac{1}{K_g^O} y_i^O c^O \frac{\partial p^O}{\partial t} + (1-\phi)\frac{Dc_\mu^i}{Dt} \tag{3.47}$$

The momentum balance equation given in Eq. 3.35 also yields:

$$\nabla \cdot \sigma = \sigma' - \alpha^I p^I \mathbf{I} \tag{3.48}$$

Lewis and Schrefler (1998) showed that the expression for the first term on the right-hand-side of Eq.3.46 or Eq. 3.47 was obtained from the substitution of the definition of compressibility. Without making this substitution into the equation, the balance equations can be written in terms of the change in molar density with respect to time as:

$$-\nabla \cdot J_i^I + \nabla \cdot \left(y_i^I c^I \frac{k_m}{\mu} \nabla p^I \right) + W_{OI}^i = \phi^I \frac{D}{Dt}\left(y_i^I c\right) + \phi^I y_i^I c^I \alpha^I \frac{\partial \epsilon_v}{\partial t} \tag{3.49}$$

$$-W_{OI}^{i} = \frac{D}{Dt}\left(\phi_f^O y_i^O c^O\right) + (1-\phi)\frac{Dc_\mu^i}{Dt} \tag{3.50}$$

where ϕ^I is the ratio of the inorganic pore volume to the bulk volume, and ϕ^O is the ratio of the organic pore volume to the bulk volume. These two porosities can be defined as follows:

$$\phi^I = \phi\left(1 - \epsilon_{kp}\right) \tag{3.51}$$

$$\phi^O = \phi\epsilon_{kp} \tag{3.52}$$

As discussed in Ambrose et al. (2012) and Hartman et al. (2012), the pore volume available for the storage and transport of gas molecules in the organic pores is reduced by the pore volume occupied by the adsorbed gas molecules. During production, pressure decreases and some adsorbed gas molecules can be produced, leading to an increase in the pore

volume available for the transport and storage of gas molecules in the free-gas state. From Eq. 3.7, this free pore volume can be defined as follows:

$$\phi_f^O = \phi\epsilon_{kf} = \phi\epsilon_{kp} - \phi_a \tag{3.53}$$

It is important to note that the free organic porosity (in the first term on the right-hand-side of Eq. 3.50) is not modeled as a constant with respect to time because the adsorbed porosity is time-dependent. This also makes the free organic porosity time-dependent, as indicated by Eq. 3.53. Substituting Eq. 3.53 into Eq. 3.50 and simplifying yields:

$$-W_{OI}^i = \phi_f^O \frac{D}{Dt}\left(y_i^O c^O\right) - y_i^O c^O \frac{D\phi_a}{Dt} + (1-\phi)\frac{Dc_\mu^i}{Dt} \tag{3.54}$$

Equations 3.49, 3.54, and 3.48 can then be solved as detailed in the previous sections. Hydraulic fractures are modeled using the discrete fracture model, which is discussed in the next chapter.

3.7 Modeling of Proppant Embedment

This section focuses on the modeling of the embedment of proppants, as well as the elastic deformation of the propped hydraulic fractures in resource shales. From the definition of the Biot's effective stress, the sharp drop in pore pressures expected near the hydraulic fracture surfaces generally leads to a corresponding sharp increase in the effective stresses that are induced near these fractures. This induced stresses, which are compressive, tends to result in the closing of the matrix on the proppants in the hydraulic fractures. To avoid the crushing of these proppants under these stresses, the proppants are generally designed to be harder than the shale matrix. This could lead to the embedment of these proppants into the matrix, and lead to a significant loss in the fracture conductivity. The time-dependent (or creep) deformation of these proppants, during proppant embed-

ment could be modeled using the viscoelastic model proposed by Guo and Liu (2012). This model is written as:

$$\Delta w_f = w_f \left[\frac{(1-\nu^2)}{E} \sigma'_{xx}(t) + \frac{1}{4\eta} \left(1 + \frac{(1-2\nu)^2}{3} \right) \int_0^t \sigma'_{xx}(t)\ \mathrm{d}t \right] \tag{3.55}$$

where, w_f is the initial fracture width, ν is the viscoelastic shear coefficient, and $\sigma'_{xx}(t)$ is the time-dependent effective closure stress that acts on the hydraulic fracture surface.

4. CONTROL-VOLUME FINITE ELEMENT METHOD

This chapter explains the discretization of the coupled partial differential equations presented in the previous chapter. I employ the control-volume finite element method to discretize all the equations presented in this work. The method is particularly suitable for the discretization of the coupled geomechanical and flow equations because it is a mass conservative scheme, where all primary variables (pressure, composition, and displacements) are colocated at the nodes or vertices of the finite elements used in the meshing of the domain. Some parts of the models presented in this chapter were presented in Olorode et al. (2017a)[1], Olorode et al. (2017b)[2], and Olorode et al. (2017c)[3].

4.1 Control-volume finite element discretization of the multi-component gas mass balance equation for a non-deformable shale reservoir

Eq. 3.27 and Eq. 3.10 can be written in a general form:

$$\nabla \cdot F_i^{\mu} + B_i^{\mu} = \frac{\partial}{\partial t} M_i^{\mu} \tag{4.1}$$

where μ represents the inorganic and organic matrices ($\mu = I, O$), $B_i^I = W_{OI}$, $B_i^O = -W_{OI}$, $F_i^O = 0$, $F_i^I = J_i^I + y_i c^I \frac{k_m}{\mu_g} \nabla p^I$, and M_i^{μ} represents the mass accumulation terms on the right-hand-side of equations 3.27 and 3.10.

[1]Part of the numerical model for non-deformable shales is reprinted with permission from "Compositional Reservoir-Flow Simulation for Organic-Rich Gas Shale" by O. M. Olorode, I. Y. Akkutlu, and Y. Efendiev, 2017. SPE Journal, Copyright 2017 by SPE.

[2]Part of the numerical model for deformable shales is reprinted with permission from "Modeling of Compositional Gas Transport in Shale as a Deformable Porous Medium" by O. M. Olorode, I. Y. Akkutlu, and Y. Efendiev, 2017. Poromechanics, VI, 1984-1991, Copyright 2017 by American Society of Civil Engineers.

[3]Part of the numerical model for the storage of CO_2 in depleted and deformable organic source rocks is reprinted with permission from "A Compositional Model for CO_2 Storage in Deformable Organic-Rich Shales" by O. M. Olorode, I. Y. Akkutlu, and Y. Efendiev, 2017. SPE Europec featured at 79th EAGE Conference, Copyright 2017 by SPE.

The simplification of F_i^O to zero is because I assume that kerogen is typically dispersed or discontinuous at the reservoir scale, as explained in the section on the proposed model.

Note that the simplification of F_i^O to zero is based on the assumption that kerogen appears to be discontinuous at the reservoir simulation scale (based on SEM images). Another reason is that the rate of transport of reservoir fluids through the nanoporous kerogen is expected to be much slower than the advective transport of hydrocarbons through the inorganic pores.

First, I perform temporal discretization independently of space. The time-dependent term on the right-hand side is discretized using the implicit Euler scheme to obtain:

$$\nabla \cdot F_i^\mu + B_i^\mu = \frac{M_i^{\mu,k+1} - M_i^{\mu,k}}{\Delta t} \tag{4.2}$$

I then proceed to integrate the conservative equation in space, over a 3D control volume, Ω_{ink}:

$$\int_\Omega \nabla \cdot F_i^\mu \, \mathrm{d}\Omega + \int_\Omega B_i^\mu \, \mathrm{d}\Omega = \int_\Omega \frac{M_i^{\mu,k+1} - M_i^{\mu,k}}{\Delta t} \, \mathrm{d}\Omega \tag{4.3}$$

Recall the Divergence theorem:

$$\int_V \nabla \cdot F \, \mathrm{d}V = \int_S F \cdot \mathbf{n} \, \mathrm{d}S \tag{4.4}$$

Using the Divergence theorem to convert the volume integral in the first term on the left-hand-side of Eq. 4.3 to a surface integral yields:

$$\int_{\partial\Omega} F_i^\mu \cdot \mathbf{n} \, \mathrm{d}S + \int_\Omega B_i^\mu \, \mathrm{d}\Omega = \int_\Omega \frac{M_i^{\mu,k+1} - M_i^{\mu,k}}{\Delta t} \, \mathrm{d}\Omega \tag{4.5}$$

Figure 4.1 illustrates the construction of a control volume centered at m. The volume integrals in Eq. 4.5 correspond to evaluating the corresponding integrals over the control

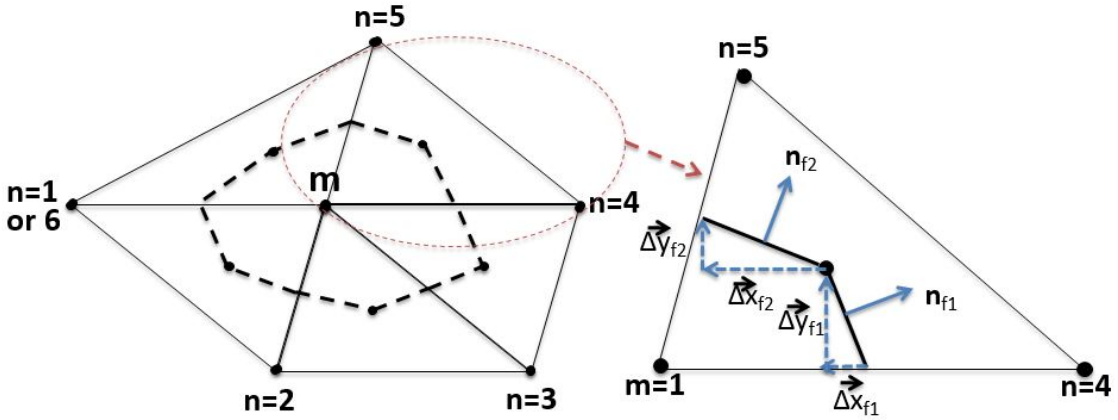

Figure 4.1: Control volume centered at m, showing its region of support, n=1,..,6. Subscripts $f1$ and $f2$ refer to face 1 and face 2 of the control volume (centered at m) within the element m,4,5

volume, circumscribed by the black dotted lines in the figure. The integration of the second term on the left-hand-side of Eq. 4.3 can be done using nodal lumping to obtain:

$$\int_{\Omega} B_i^{\mu} \, \mathrm{d}\Omega \approx B_{i,m}^{\mu} V_m \tag{4.6}$$

The integration of the mass accumulation terms on the right-hand side of Eq. 4.3 can also be performed using nodal lumping as follows:

$$\int_{\Omega} M_i^{\mu,k+1} \, \mathrm{d}\Omega \approx M_{i,m}^{\mu,k+1} V_m \tag{4.7}$$

$$\int_{\Omega} M_i^{\mu,k} \, \mathrm{d}\Omega \approx M_{i,m}^{\mu,k} V_m \tag{4.8}$$

For the control volume centered at m, I can evaluate the surface integral as follows:

$$\int_{\partial\Omega} F_i^{\mu} \cdot \mathbf{n} \, \mathrm{d}S = \sum_{n=1}^{n_m} \int_{A^n} F_i^{\mu} \cdot \mathbf{n} \, \mathrm{d}A \tag{4.9}$$

where A^n refers to the area of the faces of the control volume in the n-th element of support. This equation basically states that the net total of the diffusive flux going into the control volume centered at m is zero. For each n-th element of support in this equation, I can express the integral within the summation term as a sum of the integrals over the two faces in each element within the region of support of the control volume centered at m:

$$\int_{A^n} F_i^\mu \cdot \mathbf{n}\, \mathrm{d}A = \int_{A^n, face1} F_i^\mu \cdot \mathbf{n}\, \mathrm{d}A + \int_{A^n, face2} F_i^\mu \cdot \mathbf{n}\, \mathrm{d}A \tag{4.10}$$

These integral over the faces of the element, n can be approximated using the midpoint integration rule to obtain:

$$\int_{A^n} F_i^\mu \cdot \mathbf{n}\, \mathrm{d}A \approx F_i^\mu \cdot \mathbf{n}\ A^n|_{f1} + F_i^\mu \cdot \mathbf{n}\ A^n|_{f2} \tag{4.11}$$

To solve this equation in 2D, I introduce shape functions, ϕ_1, ϕ_2 and ϕ_3, which are defined such that:

$$\phi_m(x,y) = \begin{cases} 1, & \text{at node m} \\ 0, & \text{at all points on the opposite side of node m.} \end{cases} \tag{4.12}$$

and

$$\phi_1(x,y) + \phi_2(x,y) + \phi_3(x,y) = 1, \text{ at all points in the element} \tag{4.13}$$

Using these shape functions, any continuous variable ψ at any point in the domain can be estimated from a linear combination of the discrete values of the variable at nodes, m=1,2,3:

$$\psi(x,y) \approx \sum_{m=1}^{3} \phi_m(x,y)\, \Psi_m \tag{4.14}$$

In this formulation, ψ can represent the continuous variables– $y_i^I, c^I, p^I, y_i^O, c^O$ and p^O.

Note that these include both primary and secondary variables. The primary variables are the reference pressures in the organic and inorganic matrices (p^I and p^O) and the mole fractions in both matrices (y_i^I and y_i^O). All other variables listed are obtained from flash computations using the primary variables and a constant temperature, T as the inputs.

Figure 4.2 shows a piece-wise linear triangular finite element, with nodes at the vertices 1, 2 and 3. The area of triangle 1,2,3 can be written in the determinant form below:

$$A^{123} = \frac{1}{2} \begin{vmatrix} 1 & x_1 & y_1 \\ 1 & x_2 & y_2 \\ 1 & x_3 & y_3 \end{vmatrix} \tag{4.15}$$

Evaluating the determinant yields:

$$A^{123} = \frac{1}{2} \left[(x_2 y_3 - x_3 y_2) - x_1 (y_3 - y_2) + y_1 (x_3 - x_2) \right] \tag{4.16}$$

From Figure 4.2, three sub-triangles are formed by connecting each edge of the triangle with any point, P(x,y) within the triangle. I can also compute the areas of each of these

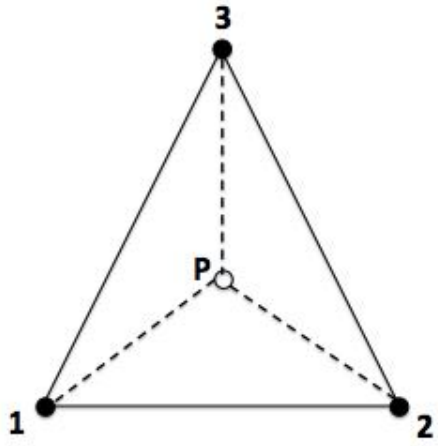

Figure 4.2: A triangular finite element

sub-triangles using the determinant form:

$$A^{P23} = \frac{1}{2}\begin{vmatrix} 1 & x & y \\ 1 & x_2 & y_2 \\ 1 & x_3 & y_3 \end{vmatrix} = \frac{1}{2}\left[(x_2y_3 - x_3y_2) - x\left(y_3 - y_2\right) + y\left(x_3 - x_2\right)\right] \tag{4.17}$$

$$A^{P31} = \frac{1}{2}\begin{vmatrix} 1 & x & y \\ 1 & x_3 & y_3 \\ 1 & x_1 & y_1 \end{vmatrix} = \frac{1}{2}\left[(x_3y_1 - x_1y_3) - x\left(y_1 - y_3\right) + y\left(x_1 - x_3\right)\right] \tag{4.18}$$

$$A^{P12} = \frac{1}{2}\begin{vmatrix} 1 & x & y \\ 1 & x_1 & y_1 \\ 1 & x_2 & y_2 \end{vmatrix} = \frac{1}{2}\left[(x_1y_2 - x_2y_1) - x\left(y_2 - y_1\right) + y\left(x_2 - x_1\right)\right] \tag{4.19}$$

Shape functions, ϕ_1, ϕ_2 and ϕ_3 can now be defined as follows:

$$\begin{aligned} \phi_1\left(x,y\right) &= \frac{A^{P23}}{A^{123}} = \frac{1}{2A^{123}}\left[(x_2y_3 - x_3y_2) - x\left(y_3 - y_2\right) + y\left(x_3 - x_2\right)\right] \\ \phi_2\left(x,y\right) &= \frac{A^{P31}}{A^{123}} = \frac{1}{2A^{123}}\left[(x_3y_1 - x_1y_3) - x\left(y_1 - y_3\right) + y\left(x_1 - x_3\right)\right] \\ \phi_3\left(x,y\right) &= \frac{A^{P12}}{A^{123}} = \frac{1}{2A^{123}}\left[(x_1y_2 - x_2y_1) - x\left(y_2 - y_1\right) + y\left(x_2 - x_1\right)\right] \end{aligned} \tag{4.20}$$

Since the sum of the areas of the three sub-triangles is equal to the area of the triangle–1,2,3, it is easy to see that these definitions of shape functions ϕ_1, ϕ_2 and ϕ_3 ensure that Eq. 4.13 is satisfied.

If point, P is moved to any of the three vertices (m=1,2 or 3), the m-th shape function, corresponding to that vertex will be equal to 1 because the area in the numerator of Eq. 4.20 will be equal to A^{123}. The other two shape functions will be zero because the area subtended between point P (which is at a vertex, m) is zero, making the numerator zero. These two statements basically confirm that Eq. 4.12 is satisfied.

To evaluate the gradient of the continuous variables $\nabla\psi$ I differentiate Eq. 4.14 to obtain:

$$\nabla\psi\left(x,y\right) \approx \sum_{m=1}^{3} \nabla\phi_m\left(x,y\right)\ \Psi_m \tag{4.21}$$

It is important to note that ψ is continuous with respect to space while Ψ is constant, and is specified at the nodes, m. In two dimensions, $\nabla\phi_m = \frac{\partial\phi_m}{\partial x} + \frac{\partial\phi_m}{\partial y}$. Substituting this into Eq. 4.21 yields:

$$\nabla\psi\left(x,y\right) \approx \left(\frac{\partial\phi_1}{x} + \frac{\partial\phi_1}{\partial y}\right)\ \Psi_1 + \left(\frac{\partial\phi_2}{\partial x} + \frac{\partial\phi_2}{\partial y}\right)\ \Psi_2 + \left(\frac{\partial\phi_3}{\partial x} + \frac{\partial\phi_3}{\partial y}\right)\ \Psi_3 \tag{4.22}$$

For brevity, I introduce the subscipt notation for the derivative of the shape functions with respect to x and y. Using this notation Eq. 4.22 can be written as:

$$\nabla\psi\left(x,y\right) \approx \left(\phi_{1x} + \phi_{1y}\right)\ \Psi_1 + \left(\phi_{2x} + \phi_{2y}\right)\ \Psi_2 + \left(\phi_{3x} + \phi_{3y}\right)\ \Psi_3 \tag{4.23}$$

The partial derivatives of each of the shape functions with respect to x and y can be obtained by differentiating Eq. 4.20 with respect to x and y to obtain:

$$\begin{aligned}
\phi_{1x} &= \frac{1}{2A^{123}}\left(y_2 - y_3\right); & \phi_{1y} &= \frac{1}{2A^{123}}\left(x_3 - x_2\right) \\
\phi_{2x} &= \frac{1}{2A^{123}}\left(y_3 - y_1\right); & \phi_{2y} &= \frac{1}{2A^{123}}\left(x_1 - x_3\right) \\
\phi_{3x} &= \frac{1}{2A^{123}}\left(y_1 - y_2\right); & \phi_{3y} &= \frac{1}{2A^{123}}\left(x_2 - x_1\right)
\end{aligned} \tag{4.24}$$

The $\Delta\overrightarrow{x}$ and $\Delta\overrightarrow{y}$ terms in Figure 4.1 can be computed from the x and y co-ordinates of the vertices of each support element. This is done by first estimating the x and y co-ordinates of the barycenter of the triangle, then estimating the co-ordinates of the point where the faces intersect the edges of the support elements.

For the support element shown on the right of Figure 4.1, the x and y co-ordinates of

the barycenter are obtained by an arithmetic average of the corresponding co-ordinate of the three vertices at m=1, n=4, and n=5. That is,

$$\begin{aligned} x_c &= \frac{1}{3}\left(x_1 + x_2 + x_3\right) \\ y_c &= \frac{1}{3}\left(y_1 + y_2 + y_3\right) \end{aligned} \tag{4.25}$$

It is important to note that I have employed the local numbering from m=1 to 3 (in the counter-clockwise direction) within the support element with vertices at m=1, n=4 and n=5.

Since the control volume faces are formed by connecting the mid-point of the edges of the support vertices and the barycenter of the elements in the region of support, I can compute the co-ordinates of these midpoints as simple arithmetic averages of the two nodes that define each edge. Hence, for face 1:

$$\begin{aligned} x_{f1} &= \frac{1}{2}\left(x_1 + x_2\right) \\ y_{f1} &= \frac{1}{2}\left(y_1 + y_2\right) \end{aligned} \tag{4.26}$$

and for face 2,

$$\begin{aligned} x_{f2} &= \frac{1}{2}\left(x_1 + x_3\right) \\ y_{f2} &= \frac{1}{2}\left(y_1 + y_3\right) \end{aligned} \tag{4.27}$$

To obtain $\Delta\overrightarrow{x}$ and $\Delta\overrightarrow{y}$ for face 1, I simply subtract Eq. 4.26 from Eq. 4.25 to obtain:

$$\begin{aligned} \Delta\overrightarrow{x}_{f1} = x_c - x_{f1} &= \frac{1}{3}\left(x_1 + x_2 + x_3\right) - \frac{1}{2}\left(x_1 + x_2\right) = \frac{1}{6}\left(2x_3 - x_2 - x_1\right) \\ \Delta\overrightarrow{y}_{f1} = y_c - y_{f1} &= \frac{1}{3}\left(y_1 + y_2 + y_3\right) - \frac{1}{2}\left(y_1 + y_2\right) = \frac{1}{6}\left(2y_3 - y_2 - y_1\right) \end{aligned} \tag{4.28}$$

To obtain $\Delta\overrightarrow{x}$ and $\Delta\overrightarrow{y}$ for face 2, I subtract Eq. 4.25 from Eq. 4.27 to obtain:

$$\begin{aligned}\Delta\overrightarrow{x}_{f2} &= x_{f2} - x_c = \frac{1}{2}(x_1 + x_3) - \frac{1}{3}(x_1 + x_2 + x_3) = \frac{1}{6}(x_1 - 2x_2 + x_3) \\ \Delta\overrightarrow{y}_{f2} &= y_{f2} - y_c = \frac{1}{2}(y_1 + y_3) - \frac{1}{3}(y_1 + y_2 + y_3) = \frac{1}{6}(y_1 - 2y_2 + y_3)\end{aligned} \tag{4.29}$$

I can then use Pythagoras theorem to calculate the length, l of face 1 and face 2 as follows:

$$\begin{aligned}l_{f1} &= \sqrt{\Delta\overrightarrow{x}_{f1}^2 + \Delta\overrightarrow{y}_{f1}^2} \\ l_{f2} &= \sqrt{\Delta\overrightarrow{x}_{f2}^2 + \Delta\overrightarrow{y}_{f2}^2}\end{aligned} \tag{4.30}$$

Assuming a constant thickness of Δz, the area of face 1 and face 2 can be computed by simply multiplying Eq. 4.30 through by Δz to obtain:

$$\begin{aligned}A_{f1} &= \Delta z\sqrt{\Delta\overrightarrow{x}_{f1}^2 + \Delta\overrightarrow{y}_{f1}^2} \\ A_{f2} &= \Delta z\sqrt{\Delta\overrightarrow{x}_{f2}^2 + \Delta\overrightarrow{y}_{f2}^2}\end{aligned} \tag{4.31}$$

The x and y components of the unit normal pointing outwards from the control volume on face 1 are given as:

$$n_x^{f1} = \frac{\Delta\overrightarrow{y}_{f1}}{A_{f1}}; \qquad\qquad n_y^{f1} = -\frac{\Delta\overrightarrow{x}_{f1}}{A_{f1}} \tag{4.32}$$

Similarly, the x and y components of the unit normal pointing outwards from the control volume on face 1 are given as:

$$n_x^{f2} = \frac{\Delta\overrightarrow{y}_{f2}}{A_{f2}}; \qquad\qquad n_y^{f2} = -\frac{\Delta\overrightarrow{x}_{f2}}{A_{f2}} \tag{4.33}$$

To simplify the formulation for evaluating the flux terms in Eq. 4.1, I introduce a generic nonlinear coefficient $q(\psi)$ to represent any of the nonlinear coefficients in these two equa-

tions. When this term is not strongly direction-dependent, a simple evaluation of $q(\psi)$ at the mid-point of the interface between any two control volumes should be sufficient. In cases where $q(\psi)$ is strongly nonlinear and direction-dependent, the upwinding scheme discussed in Zhao (2012) could be more suitable. Zhao (2012) opined that this method keeps the flux across the interface between two subcontrol volumes continuous, and ensures local mass balance. The method is implemented as follows:

$$q_f(\psi) = \begin{cases} q_f(\Psi_m), & \text{if } \nabla\Psi \cdot \mathbf{n} A_f \leq 0 \\ q_f(\Psi_n), & \text{if } \nabla\Psi \cdot \mathbf{n} A_f > 0. \end{cases} \tag{4.34}$$

Equation 4.34 is written out for any face, f. This is because the equation applies for both faces f1 and f2. The only difference is the support node, n, that is used at each face $f1$ or $f2$, and the corresponding unit outward normal vector $\mathbf{n}$ for each face.

One more point to note is that at any node m or n, the shape function at that node is equal to 1. This means that ψ and Ψ are equivalent at the nodes.

Using the definition for the generic nonlinear coefficient, I introduce a generic flux, F defined as $F = q\nabla\psi$. Evaluating Eq. 4.11 in terms of these generic functions yields:

$$\int_{A^n} q\nabla\psi \cdot \mathbf{n}\, \mathrm{d}A \approx q\nabla\psi \cdot \mathbf{n}\ A^n|_{f1} + q\nabla\psi \cdot \mathbf{n}\ A^n|_{f2} \tag{4.35}$$

I now proceed to evaluate Eq. 4.35 using the derived geometric equations. Substituting Eq. 4.22 into Eq. 4.35 yields:

$$\begin{aligned} &\int_{A^n} q\nabla\psi \cdot \mathbf{n}\, \mathrm{d}A \approx q\nabla\psi \cdot \mathbf{n}\ A^n|_{f1} + q\nabla\psi \cdot \mathbf{n}\ A^n|_{f2} \\ &= q_{f1}\left[(\phi_{1x} + \phi_{1y})\ \Psi_1 + (\phi_{2x} + \phi_{2y})\ \Psi_2 + (\phi_{3x} + \phi_{3y})\ \Psi_3\right] \cdot \mathbf{n^{f1}}\ A^j_{f1} \\ &+ q_{f2}\left[(\phi_{1x} + \phi_{1y})\ \Psi_1 + (\phi_{2x} + \phi_{2y})\ \Psi_2 + (\phi_{3x} + \phi_{3y})\ \Psi_3\right] \cdot \mathbf{n^{f2}}\ A^j_{f2} \end{aligned} \tag{4.36}$$

Expressing n^{f1} and n^{f2} in terms of their x and y components and collecting like terms yields:

$$\begin{aligned}\int_{A^j} q\nabla\psi\cdot\mathbf{n}\,\mathrm{d}A = \\ q_{f1}\left[\left(\phi_{1x}\,\Psi_1+\phi_{2x}\,\Psi_2+\phi_{3x}\,\Psi_3\right)\cdot\mathbf{n_x^{f1}}+\left(\phi_{1y}\,\Psi_1+\phi_{2y}\,\Psi_2+\phi_{3y}\,\Psi_3\right)\cdot\mathbf{n_y^{f1}}\right]A^j_{f1} \\ +q_{f2}\left[\left(\phi_{1x}\,\Psi_1+\phi_{2x}\,\Psi_2+\phi_{3x}\,\Psi_3\right)\cdot\mathbf{n_x^{f2}}+\left(\phi_{1y}\,\Psi_1+\phi_{2y}\,\Psi_2+\phi_{3y}\,\Psi_3\right)\cdot\mathbf{n_y^{f2}}\right]A^j_{f2}\end{aligned} \tag{4.37}$$

Substituting Eq. 4.32 and Eq. 4.33 into Eq. 4.37 yields:

$$\begin{aligned}\int_{A^j} q\nabla\psi\cdot\mathbf{n}\,\mathrm{d}A = \\ q_{f1}\left[\left(\phi_{1x}\,\Psi_1+\phi_{2x}\,\Psi_2+\phi_{3x}\,\Psi_3\right)\Delta\overrightarrow{y}_{f1}-\left(\phi_{1y}\,\Psi_1+\phi_{2y}\,\Psi_2+\phi_{3y}\,\Psi_3\right)\Delta\overrightarrow{x}_{f1}\right] \\ +q_{f2}\left[\left(\phi_{1x}\,\Psi_1+\phi_{2x}\,\Psi_2+\phi_{3x}\,\Psi_3\right)\Delta\overrightarrow{y}_{f2}-\left(\phi_{1y}\,\Psi_1+\phi_{2y}\,\Psi_2+\phi_{3y}\,\Psi_3\right)\Delta\overrightarrow{x}_{f2}\right]\end{aligned} \tag{4.38}$$

Rearranging the equations such that the coefficients of Ψ_1, Ψ_2 and Ψ_3 are grouped together yields:

$$\begin{aligned}\int_{A^j} q\nabla\psi\cdot\mathbf{n}\,\mathrm{d}A = \\ \left[q_{f1}\left(\phi_{1x}\Delta\overrightarrow{y}_{f1}-\phi_{1y}\Delta\overrightarrow{x}_{f1}\right)+q_{f2}\left(\phi_{1x}\Delta\overrightarrow{y}_{f2}-\phi_{1y}\Delta\overrightarrow{x}_{f2}\right)\right]\Psi_1 \\ +\left[q_{f1}\left(\phi_{2x}\Delta\overrightarrow{y}_{f1}-\phi_{2y}\Delta\overrightarrow{x}_{f1}\right)+q_{f2}\left(\phi_{2x}\Delta\overrightarrow{y}_{f2}-\phi_{2y}\Delta\overrightarrow{x}_{f2}\right)\right]\Psi_2 \\ +\left[q_{f1}\left(\phi_{3x}\Delta\overrightarrow{y}_{f1}-\phi_{3y}\Delta\overrightarrow{x}_{f1}\right)+q_{f2}\left(\phi_{3x}\Delta\overrightarrow{y}_{f2}-\phi_{3y}\Delta\overrightarrow{x}_{f2}\right)\right]\Psi_3\end{aligned} \tag{4.39}$$

Introducing variables a_1, a_2 and a_3 to replace the coefficients of Ψ_1, Ψ_2 and Ψ_3 in Eq. 4.39 yields:

$$\int_{A^j} q\nabla\psi\cdot\mathbf{n}\,\mathrm{d}A = a_1\Psi_1+a_2\Psi_2+a_3\Psi_3 \tag{4.40}$$

where,

$$
\begin{aligned}
a_1 &= q_{f1}\left(\phi_{1x}\Delta\overrightarrow{y}_{f1} - \phi_{1y}\Delta\overrightarrow{x}_{f1}\right) + q_{f2}\left(\phi_{1x}\Delta\overrightarrow{y}_{f2} - \phi_{1y}\Delta\overrightarrow{x}_{f2}\right) \\
a_2 &= q_{f1}\left(\phi_{2x}\Delta\overrightarrow{y}_{f1} - \phi_{2y}\Delta\overrightarrow{x}_{f1}\right) + q_{f2}\left(\phi_{2x}\Delta\overrightarrow{y}_{f2} - \phi_{2y}\Delta\overrightarrow{x}_{f2}\right) \\
a_3 &= q_{f1}\left(\phi_{3x}\Delta\overrightarrow{y}_{f1} - \phi_{3y}\Delta\overrightarrow{x}_{f1}\right) + q_{f2}\left(\phi_{3x}\Delta\overrightarrow{y}_{f2} - \phi_{3y}\Delta\overrightarrow{x}_{f2}\right)
\end{aligned}
\tag{4.41}
$$

Note that in these equations, index 1 corresponds to the index of the control volume center, i, while local nodes 2 and 3 correspond to the other two nodes (n=4 and n=5 for the expanded element in Figure 4.1) in any element within the region of support of node, m. For any element having the other two nodes at any global n value, Eq. 4.40 can be written as:

$$
\int_{A^j} q\nabla\psi\cdot\mathbf{n}\,\mathrm{d}A = a_m\Psi_m + a_n\Psi_n + a_{n+1}\Psi_{n+1} \tag{4.42}
$$

This equation, written for just one element in the region of support of a node m, can then be summed for all the elements in the region of support of any node, m using Eq. 4.9:

$$
\begin{aligned}
\int_{\partial\Omega} F\cdot\mathbf{n}\,\mathrm{d}S &= \sum_{n=1}^{n_n}\int_{A^n} F\cdot\mathbf{n}\,\mathrm{d}A \\
&= \sum_{n=1}^{n_n}\left(a_m^j\Psi_m + a_n^j\Psi_n + a_{n+1}^j\Psi_{n+1}\right)
\end{aligned}
\tag{4.43}
$$

where I have written the equation in terms of each of the transport mechanisms. So, for the gas-phase advection term in the inorganic matrix for instance, $a_m\Psi_m = a^{adv}P_m^I$.

To set up the full problem in matrix form, I start by multiplying both sides of Eq.4.5 by Δt to obtain:

$$
\Delta t\int_{\partial\Omega} F\cdot\mathbf{n}\,\mathrm{d}S + \Delta t\int_{\Omega} B\,\mathrm{d}\Omega = \int_{\Omega} M^{k+1}\,\mathrm{d}\Omega - \int_{\Omega} M^{k}\,\mathrm{d}\Omega \tag{4.44}
$$

The residual of this equation at the p^{th} Newton Raphson Iteration can then be written as:

$$R_i^p = \Delta t \int_{\partial\Omega} F_i^\mu \cdot \mathbf{n}\, \mathrm{d}S + \Delta t \int_\Omega B_i^\mu \, \mathrm{d}\Omega - \int_\Omega M_i^{\mu,k+1} \, \mathrm{d}\Omega + \int_\Omega M_i^{\mu,k} \, \mathrm{d}\Omega = 0 \tag{4.45}$$

Substituting equations 4.6, 4.7, 4.8 and 4.43 into Eq. 4.45 yields:

$$R_i^p = \Delta t \sum_{n=1}^{n_n} \left(a_m^j \Psi_m + a_n^j \Psi_n + a_{n+1}^j \Psi_{n+1} \right) + \Delta t B_{i,m}^\mu V_m - M_{i,m}^{\mu,k+1} V_m + M_{i,m}^{\mu,k} V_m \approx 0 \tag{4.46}$$

To complete the formulation of this equation in matrix form, I need to express the volume, V_m in terms of the sum of the volumes coming from each element in the region of support of the control volume centered at m. The volume of an element within the region of support of a node, m, can be expressed as a product of the area of the element and its thickness, Δz, assuming a constant thickness. Hence from Eq. 4.16, the the volume of triangle 123 is given by:

$$V^{123} = \frac{\Delta z}{2} \left[(x_2 y_3 - x_3 y_2) - x_1 (y_3 - y_2) + y_1 (x_3 - x_2) \right] \tag{4.47}$$

A triangle within the region of support for a node, m, contributes only a third of its area (or volume, assuming a constant thickness) to the control volume centered at m. Therefore, the control volume centered at m, as a volume:

$$V_m = \sum_{n=1}^{n_n} \frac{1}{3} V^{m,n,n+1} \tag{4.48}$$

Substituting this into Eq. 4.46 and writing the equation for the inorganic matrix yields:

$$R_i^I = \Delta t \left[\sum_{n=1}^{n_n} \left(a_m^j \Psi_m + a_n^j \Psi_n + a_{n+1}^j \Psi_{n+1} \right) \right]^I + \Delta t B_{i,m}^I \sum_{n=1}^{n_n} \frac{1}{3} V^{m,n,n+1} \\ - M_{i,m}^{I,k+1} \sum_{n=1}^{n_n} \frac{1}{3} V^{m,n,n+1} + M_{i,m}^{I,k} \sum_{n=1}^{n_n} \frac{1}{3} V^{m,n,n+1} \approx 0 \tag{4.49}$$

where all the Ψ_m, Ψ_n and Ψ_{n+1} terms are evaluated at the p-th Newton Raphson Iteration and at the current time-step, $k+1$, except the last term, Ψ_m^k, which is simply the value of Ψ_m at the previous time step, k.

Going through an identical procedure, the residual of the organic mass balance equation can be obtained as:

$$R_i^O = \Delta t B^O \sum_{n=1}^{n_n} \frac{1}{3} V^{m,n,n+1} - M_{i,m}^{O,k+1} \sum_{n=1}^{n_n} \frac{1}{3} V^{m,n,n+1} + M_{i,m}^{O,k} \sum_{n=1}^{n_n} \frac{1}{3} V^{m,n,n+1} \approx 0 \tag{4.50}$$

I substitute the total mass of the hydrocarbon in place of the n-th hydrocarbon species mass balance, to obtain the following equations for the inorganic and organic matrices, respectively:

$$R_H^I = \Delta t \left[\sum_{n=1}^{n_n} \left(a_m^H \Psi_m + a_n^H \Psi_n + a_{n+1}^H \Psi_{n+1} \right) \right]^I + \Delta t B_{H,m}^I \sum_{n=1}^{n_n} \frac{1}{3} V^{m,n,n+1} \\ - M_{H,m}^{I,k+1} \sum_{n=1}^{n_n} \frac{1}{3} V^{m,n,n+1} + M_{H,m}^{I,k} \sum_{n=1}^{n_n} \frac{1}{3} V^{m,n,n+1} \approx 0 \tag{4.51}$$

$$R_H^O = \Delta t B_{H,m}^O \sum_{n=1}^{n_n} \frac{1}{3} V^{m,n,n+1} - M_{H,m}^{O,k+1} \sum_{n=1}^{n_n} \frac{1}{3} V^{m,n,n+1} + M_{H,m}^{O,k} \sum_{n=1}^{n_n} \frac{1}{3} V^{m,n,n+1} \approx 0 \tag{4.52}$$

where the superscript or subscript, H, refers to the equation for the total mass of hydrocarbon. Therefore, Ψ refers to the inorganic matrix pressure in Eq. 4.51, while the a's correspond to the mobility term, which are the coefficients of the pressure gradient in Eq.

3.9. Note that the first term on the right-hand-side of Eq. 4.51 is missing in Eq. 4.52. This is because of the assumption that the kerogen is discontinuous in the reservoir domain as explained in Chapter 2.

From Taylor series expansion:

$$R^{k+1}\left(X+\Delta X\right)=R^{k+1}\left(X\right)+\Delta X\frac{\partial R^{k+1}}{\partial X}+...\approx 0 \tag{4.53}$$

where X represents the vector of primary variables (p^I, y_i^I, p^O, y_i^O) .

Since $R^{k+1}\approx 0$, I can rearrange the Taylor series expansion equation to obtain:

$$\frac{\partial R^{k+1}}{\partial X}\Delta X=-R^{k+1}\left(X\right) \tag{4.54}$$

This presents the linearized system of equations in the form Ax = b, where for a cell at a global index m, the equation can be written in the matrix form:

$$\begin{bmatrix} \frac{\partial R^I_{P^I}}{\partial p^I} & \frac{\partial R^I_{P^I}}{\partial p^O} & \frac{\partial R^I_{P^I}}{\partial y^I_1} & \frac{\partial R^I_{P^I}}{\partial y^O_1} & .. & \frac{\partial R^I_{P^I}}{\partial y^I_{n_c-1}} & \frac{\partial R^I_{P^I}}{\partial y^O_{n_c-1}} \\ \frac{\partial R^O_{P^O}}{\partial p^I} & \frac{\partial R^O_{P^O}}{\partial p^O} & \frac{\partial R^O_{P^O}}{\partial y^I_1} & \frac{\partial R^O_{P^O}}{\partial y^O_1} & .. & \frac{\partial R^O_{P^O}}{\partial y^I_{n_c-1}} & \frac{\partial R^O_{P^O}}{\partial y^O_{n_c-1}} \\ \frac{\partial R^I_1}{\partial p^I} & \frac{\partial R^I_1}{\partial p^O} & \frac{\partial R^I_1}{\partial y^I_1} & \frac{\partial R^I_1}{\partial y^O_1} & .. & \frac{\partial R^I_1}{\partial y^I_{n_c-1}} & \frac{\partial R^I_1}{\partial y^O_{n_c-1}} \\ \frac{\partial R^O_1}{\partial p^I} & \frac{\partial R^O_1}{\partial p^O} & \frac{\partial R^O_1}{\partial y^I_1} & \frac{\partial R^O_1}{\partial y^O_1} & .. & \frac{\partial R^O_1}{\partial y^I_{n_c-1}} & \frac{\partial R^O_1}{\partial y^O_{n_c-1}} \\ : & : & : & : & : & : & : \\ \frac{\partial R^I_{n_c-1}}{\partial p^I} & \frac{\partial R^I_{n_c-1}}{\partial p^O} & \frac{\partial R^I_{n_c-1}}{\partial y^I_1} & \frac{\partial R^I_{n_c-1}}{\partial y^O_1} & .. & \frac{\partial R^I_{n_c-1}}{\partial y^I_{n_c-1}} & \frac{\partial R^I_{n_c-1}}{\partial y^O_{n_c-1}} \\ \frac{\partial R^O_{n_c-1}}{\partial p^I} & \frac{\partial R^O_{n_c-1}}{\partial p^O} & \frac{\partial R^O_{n_c-1}}{\partial y^I_1} & \frac{\partial R^O_{n_c-1}}{\partial y^O_1} & .. & \frac{\partial R^O_{n_c-1}}{\partial y^I_{n_c-1}} & \frac{\partial R^O_{n_c-1}}{\partial y^O_{n_c-1}} \end{bmatrix} \begin{bmatrix} \Delta p^I \\ \Delta p^O \\ \Delta y^I_1 \\ \Delta y^O_1 \\ : \\ \Delta y^I_{n_c-1} \\ \Delta y^O_{n_c-1} \end{bmatrix} = - \begin{bmatrix} \Delta R^I_{p^I} \\ \Delta R^O_{p^O} \\ \Delta R^I_1 \\ \Delta R^O_1 \\ : \\ \Delta R^I_{n_c-1} \\ \Delta R^O_{n_c-1} \end{bmatrix} \tag{4.55}$$

where each term in the linear system of equations is evaluated at the current time step (k+1) and Newton-Raphson iteration level (p).

The solution to this equation gives the change in the primary variables (ΔX) at each Newtonian iteration level, p, for the current time step (k+1). At this same current time step (k+1), the primary variables for the next Newtonian iteration is then calculated as outlined below:

$$p_m^{I,k+1,p+1} = p_m^{I,k+1,p} + \Delta p_m^{I,k+1,p} \tag{4.56}$$

$$p_m^{O,k+1,p+1} = p_m^{O,k+1,p} + \Delta p_m^{O,k+1,p} \tag{4.57}$$

$$y_{i,m}^{I,k+1,p+1} = y_{i,m}^{I,k+1,p} + \Delta y_{i,m}^{I,k+1,p} \tag{4.58}$$

$$y_{i,m}^{O,k+1,p+1} = y_{i,m}^{O,k+1,p} + \Delta y_{i,m}^{O,k+1,p} \tag{4.59}$$

The Newtonian iteration is continued until the system converges. When the system converges, I update the primary variables and then move on to the next time-step.

4.2 Control-volume finite element discretization of the gas mass balance equation for a deformable shale reservoir

In this section, I solve the fully-coupled poroelasticity equations that describe the flow of multicomponent gas in a deformable dual-continuum shale matrix. The use of the CVFEM provides a natural discretization for the simultaneous solution of the mass balance and solid linear momentum balance equations. The data structures and geometric parameters that are required for the numerical solution of the mass balance equations are readily available for use in the solution of the solid linear momentum balance equations. Comparing the mass balance equations for a non-deformable matrix (Eq. 3.1 and 3.10) with those for the deformable matrix (Eq. 3.49 and 3.54), I observe that the main differences are in the accumulation terms on the right-hand-side. Therefore, the results of the CVFE discretization of the transport terms in Eq. 3.1 and 3.10 are the same as those of the transport terms in Eq. 3.49 and 3.54. For a complete discretization of Eq. 3.49 and 3.54, I only need to discretize the accumulation terms in Eq. 3.49 and 3.54.

The evaluation of all the terms on the right-hand-side of Eq. 3.54 and the first term on the right-hand-side of Eq. 3.49 can be obtained by a simple application of nodal lumping, as in Eq. 4.6. However, to evaluate the second term on the right-hand-side of Eq. 3.49, I need a procedure to evaluate the numerical integral of a nodal derivative.

Equation 8.18 of Voller (2009) for the estimation of a nodal derivative was written as:

$$\frac{\partial \Psi}{\partial x}|_1 V_1 = \int_{CV} \frac{\partial \Psi}{\partial x}\,\mathrm{d}A = \oint_{CS} \Psi \cdot n_x\,\mathrm{d}S \approx \sum_{faces} \Psi_{mid} \Delta \overrightarrow{y} \tag{4.60}$$

and from Equation 8.25 of Voller (2009), I obtain:

$$\frac{\partial \Psi}{\partial x}|_1 V_1 = \sum_{support} \frac{V_{ele}}{3} \frac{\partial \Psi}{\partial x}|_{ele} \; ; \qquad \frac{\partial \Psi}{\partial y}|_1 V_1 = \sum_{support} \frac{V_{ele}}{3} \frac{\partial \Psi}{\partial y}|_{ele} \tag{4.61}$$

Recall that from nodal lumping:

$$\int_V \frac{\partial \Psi}{\partial x} \, \mathrm{d}V = \frac{\partial \Psi}{\partial x} V \tag{4.62}$$

So, combining Eq. 4.62 and Eq. 4.61 yields:

$$\int_V \frac{\partial \Psi}{\partial x} \, \mathrm{d}V = \sum_{support} \frac{V_{ele}}{3} \frac{\partial \Psi}{\partial x}|_{ele} \; ; \qquad \int_V \frac{\partial \Psi}{\partial y} \, \mathrm{d}V = \sum_{support} \frac{V_{ele}}{3} \frac{\partial \Psi}{\partial y}|_{ele} \tag{4.63}$$

where

$$\begin{aligned} \frac{\partial \Psi}{\partial x}|_{ele} &= \phi_{1x} \Psi_{x_1} + \phi_{2x} \Psi_{x_2} + \phi_{3x} \Psi_{x_3} \\ \frac{\partial \Psi}{\partial y}|_{ele} &= \phi_{1y} \Psi_{y_1} + \phi_{2y} \Psi_{y_2} + \phi_{3y} \Psi_{y_3} \end{aligned} \tag{4.64}$$

By Eq. 4.63, the integral of the second term on the right-hand-side of Eq. 3.49 over a control volume Ω can be discretized as follows:

$$\begin{aligned} \phi^I y_i^I c^I \alpha^I \int_\Omega \frac{\partial \epsilon_v}{\partial t} \, \mathrm{d}\Omega = \frac{\phi^I y_i^I c^I \alpha^I}{\Delta t} \int_\Omega \left[\left(\frac{\partial u_x}{\partial x} + \frac{\partial u_y}{\partial y} \right)^{k+1} - \left(\frac{\partial u_x}{\partial x} + \frac{\partial u_y}{\partial y} \right)^{k} \right] \mathrm{d}\Omega = \\ \frac{\phi^I y_i^I c^I \alpha^I}{\Delta t} \sum_{support} \frac{V_{ele}}{3} \left[\left(\frac{\partial u_x}{\partial x}|_{ele} + \frac{\partial u_y}{\partial y}|_{ele} \right)^{k+1} - \left(\frac{\partial u_x}{\partial x}|_{ele} + \frac{\partial u_y}{\partial y}|_{ele} \right)^{k} \right] \end{aligned} \tag{4.65}$$

This approach of evaluating the integral of a nodal derivative by applying a lump mass approximation and a Gaussian quadrature to evaluate the volume strain integral was also discussed in Fung (1992). Combining the results from Eq. 4.65 with the CVFE discretiza-

tion results of the transport terms in Eq. 4.49 yields:

$$R_i^I = \Delta t \left[\sum_{n=1}^{n_n} \left(a_m^j \Psi_m + a_n^j \Psi_n + a_{n+1}^j \Psi_{n+1} \right) \right]^I - \phi^I \left(y_i c^I |_m^{k+1} - y_i c^I |_m^k \right) V_m$$
$$- y_i c^I \phi^I \alpha^I \sum_{n=1}^{n_n} \frac{V_{ele}}{3} \left(\frac{\partial u_x}{\partial x}^{k+1} |_{ele} + \frac{\partial u_y}{\partial y}^{k+1} |_{ele} - \frac{\partial u_x}{\partial x}^{k} |_{ele} - \frac{\partial u_y}{\partial y}^{k} |_{ele} \right) \quad (4.66)$$
$$+ \Delta t B_{i,m}^I V_m$$

The expression for determining the x and y components of the volumetric strain over an element can be obtained from Eq. 4.64 as:

$$\frac{\partial u_x}{\partial x}|_{ele} = \phi_{1x} U_{x_i} + \phi_{2x} U_{x_j} + \phi_{3x} U_{x_{j+1}} \quad (4.67)$$

$$\frac{\partial u_y}{\partial y}|_{ele} = \phi_{1y} U_{y_i} + \phi_{2y} U_{y_j} + \phi_{3y} U_{y_{j+1}} \quad (4.68)$$

where the ϕ_i terms are the interpolating functions or shape functions associated with the control volume finite element method, and i, j and $j+1$ are the indices of the three nodes making up each triangular finite element in the region of support of the control volume centered at node, i.

The residual form of the mass balance equations for the hydrocarbon components in the organic pores can be obtained in a similar fashion as follows:

$$R_i^O = \Delta t B_{i,m}^O V_m - \phi_f^O \left(y_i^O c^O |_m^{k+1} - y_i^O c^O |_m^k \right) V_m - y_i^O c^O \left(\phi_a^{k+1} - \phi_a^k \right) V_m$$
$$- (1 - \phi) \left(c_{\mu,i}^{k+1} - c_{\mu,i}^k \right) V_m \quad (4.69)$$

Considering that the Maxwell-Stefan diffusion coefficient matrix is of order $n_c - 1$ for a system with n_c hydrocarbon components, the equations for each component in each continuum with subscript, i is for the first $n_c - 1$ components. To obtain the last equation

to complete the system of equations, I write the mass balance equation for the total mass of hydrocarbons as the sum of all the hydrocarbon components. More details on this numerical modeling approach is given by Cao (2002).

Therefore, to obtain the residual of the total mass of hydrocarbon (which is also referred to as the residual of the pressure equation), I add up the residual equations for each hydrocarbon component to obtain:

$$\begin{aligned} R_H^I = \Delta t \left[\sum_{n=1}^{n_n} \left(a_m^j \Psi_m + a_n^j \Psi_n + a_{n+1}^j \Psi_{n+1} \right) \right]^I - \phi^I \left(c^I|_m^{k+1} - c^I|_m^k \right) V_m \\ -c^I \phi^I \alpha^I \sum_{n=1}^{n_n} \frac{V_{ele}}{3} \left(\frac{\partial u_x}{\partial x}^{k+1} |_{ele} + \frac{\partial u_y}{\partial y}^{k+1} |_{ele} - \frac{\partial u_x}{\partial x}^{k} |_{ele} - \frac{\partial u_y}{\partial y}^{k} |_{ele} \right) \\ + \Delta t B_m^I V_m \end{aligned} \tag{4.70}$$

$$\begin{aligned} R_H^O = \Delta t B_{H,m}^O V_m - \phi_f^O \left(c^O|_m^{k+1} - c^O|_m^k \right) V_m - c^O \left(\phi_a^{k+1} - \phi_a^k \right) V_m \\ - (1-\phi) \left(c_\mu^{k+1} - c_\mu^k \right) V_m \end{aligned} \tag{4.71}$$

It is important to note that all the parameters in each of the residual equations are evaluated at the current time-step, $k+1$, except the parameters shown explicitly at k.

4.3 Control-volume finite element discretization of the momentum balance equation for a deformable shale matrix

Voller (2009) detailed the procedure for discretizing and solving the equations for linear elasticity. This work extends this to the poroelastic case by accounting for the contribution of the fluids in the pore spaces to the support of confining stresses on the porous medium.

Substituting, $\kappa_{xx} = \kappa_{yy} = E/\left(1-\nu^2\right)$ and $\kappa_{xy} = E/\left[2\left(1+\nu\right)\right]$, and following the

CVFE procedure detailed in Voller (2009), I discretize Eq. 3.40 and obtain:

$$\int_S \kappa_{xx}\frac{\partial u_x}{\partial x}\cdot\mathbf{n_x}+\kappa_{xy}\frac{\partial u_x}{\partial y}\cdot\mathbf{n_y}+\nu\kappa_{xx}\frac{\partial u_y}{\partial y}\cdot\mathbf{n_x}+\kappa_{xy}\frac{\partial u_y}{\partial x}\cdot\mathbf{n_y}\,\mathrm{d}S - \int_\Omega \alpha^I\frac{\partial p^I}{\partial x}\,\mathrm{d}\Omega = -\sum_{j=1}^{n_n}\alpha^I\frac{\partial p^I}{\partial x}|_{ele}\frac{V_{ele}}{3} + \sum_{j=1}^{n_n}a^x_{i,j}u_{xS_{i,j}}+\sum_{j=1}^{n_n}b^x_{i,j}u_{yS_{i,j}} \tag{4.72}$$

Similarly, Eq. 3.41 becomes

$$\int_S \kappa_{xy}\frac{\partial u_y}{\partial x}\cdot\mathbf{n_x}+\kappa_{yy}\frac{\partial u_y}{\partial y}\cdot\mathbf{n_y}+\kappa_{xy}\frac{\partial u_x}{\partial y}\cdot\mathbf{n_x}+\nu\kappa_{yy}\frac{\partial u_x}{\partial x}\cdot\mathbf{n_y}\,\mathrm{d}S - \int_\Omega \alpha^I\frac{\partial p^I}{\partial y}\,\mathrm{d}\Omega = -\sum_{j=1}^{n_n}\alpha^I\frac{\partial p^I}{\partial y}|_{ele}\frac{V_{ele}}{3} + \sum_{j=1}^{n_n}a^y_{i,j}u_{yS_{i,j}}+\sum_{j=1}^{n_n}b^y_{i,j}u_{xS_{i,j}} \tag{4.73}$$

where the constants $a_{i,j}$ and $b_{i,j}$ in this equation are defined in a similar fashion as in Voller (2009). It is also worth noting that the evaluation of the integral of the derivative of pore-pressure in equations 4.72 and 4.73 involved using nodal lumping to evaluate the integral of a nodal derivative as discussed in the previous section.

Expressing these two equations in the residual form yields:

$$R^{U_x} = \sum_{j=1}^{n_n}a^x_{i,j}u_{xS_{i,j}}+\sum_{j=1}^{n_n}b^x_{i,j}u_{yS_{i,j}}-\sum_{j=1}^{n_n}\alpha^I\frac{\partial p^I}{\partial x}|_{ele}\frac{V_{ele}}{3} \tag{4.74}$$

$$R^{U_y} = \sum_{j=1}^{n_n}a^y_{i,j}u_{yS_{i,j}}+\sum_{j=1}^{n_n}b^y_{i,j}u_{xS_{i,j}}-\sum_{j=1}^{n_n}\alpha^I\frac{\partial p^I}{\partial y}|_{ele}\frac{V_{ele}}{3} \tag{4.75}$$

The derivatives of pressure over each triangular element can be evaluated using the derivatives of the shape functions as shown in equations 4.67 and 4.68. So, for any pressure, p,

its derivative with respect to x over an element is given as:

$$\frac{\partial p}{\partial x}|_{ele} = \phi_{1x}P_i + \phi_{2x}P_j + \phi_{3x}P_{j+1} \tag{4.76}$$

where P_i is the pressure at a node i, while P_j and P_{j+1} are the pressures at the two neighbors of node i in any triangular element.

4.4 Discrete Fracture Model

All the equations presented up to this point implicitly assume that the matrix is not fractured. In this section, I focus on how I can model hydraulic and natural fractures in shale-gas reservoirs using the Discrete Fracture Model (DFM). The DFM was originally developed as a better alternative to the dual continuum models in naturally-fractured reservoirs, where the properties of the individual fractures in the fracture network vary, and the fractures may be unevenly distributed across the reservoir domain. Additionally, the DFM is computationally efficient because the fractures are modeled at a dimension of $n - 1$, where n is the number of dimensions of the reservoir (Noorishad and Mehran, 1982). An attempt to explicitly model all the natural fractures in a reservoir could be very tedious, unrealistic and unnecessary, given the relative accuracy of the DFM in comparison to an explicit model for the fracture. Kim and Deo (2000) presented some examples of this comparison, albeit in the context of natural fractures. Li and Lee (2008) also used the DFM to model natural fractures in black oil reservoirs, and discussed an implementation of the DFM for long fractures that intersect wells. In the next section, I show a corresponding comparison of the results from DFM to an explicit fracture model for hydraulic fractures.

Given the tendency for shale and tight gas reservoirs to be naturally fractured, the use of the DFM to model these unconventional resources could provide a consistent, efficient and accurate treatment of hydraulic and natural fractures. Multiscale models based on the DFM have also been developed to further improve the computational efficiency in the

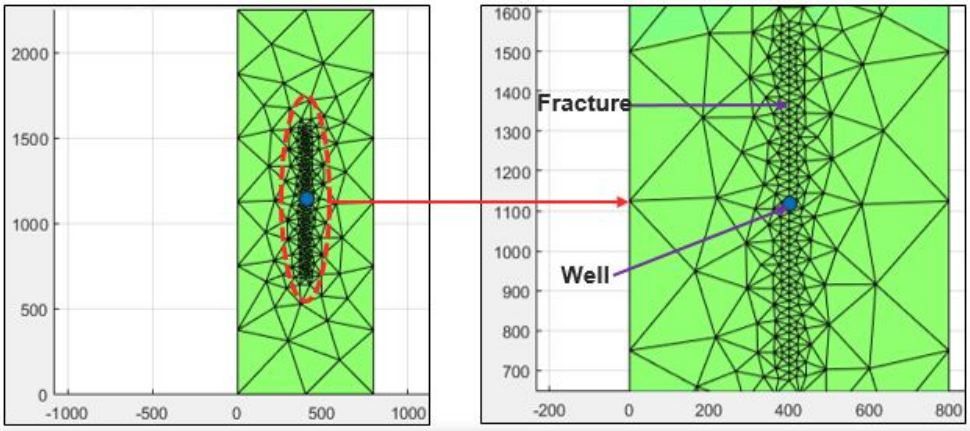

Figure 4.3: This figure shows the unstructured gridding of the reservoir domain with Gmsh. The physical dimension of the reservoir is also shown.

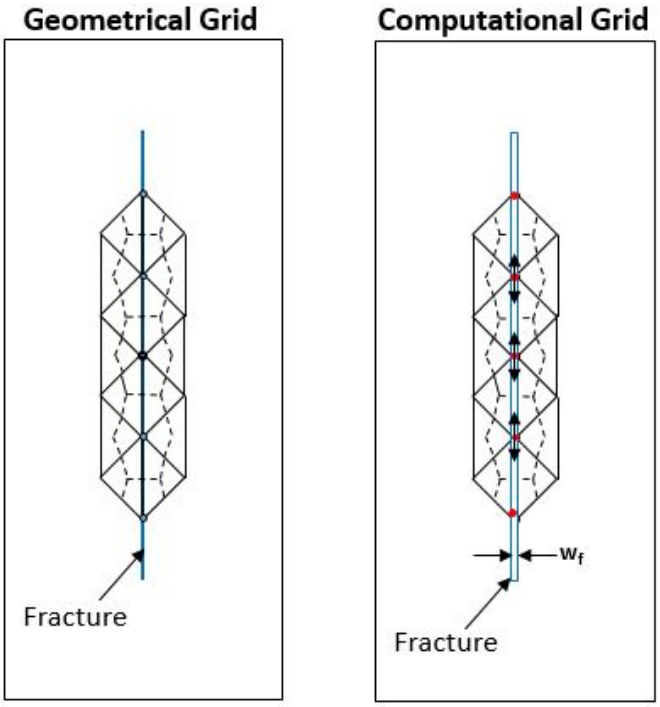

Figure 4.4: The fracture is represented as a line in the geometrical domain, but as a 2D plane with an aperture (and corresponding volume) in the computational domain.

modeling of fractured shale-gas reservoirs (Efendiev et al.,2015; Akkutlu et al.,2016). A simple way of implementing the DFM in a CVFEM simulator involves a linear superposition of the matrix and fracture domains. That is, the total domain could be decomposed into these two subdomains. Programmatically, this means that I add the residual of the mass balance equations of the hydrocarbon components in the inorganic matrix to the mass balance equations of the hydrocarbon components in the fracture. Monteagudo and Firoozabadi (2004) details the application of this approach in a control-volume method.

Figure 4.3 shows the discretization of a single vertical fracture in a reservoir modeled using the DFM, with all dimensions shown in meters. This grid (as well as all other grids used in the simulation studies presented) was generated using "Gmsh", a free 3D finite element grid generator (Geuzaine and Remacle, 2009). Figure 4.4 gives a sketch illustrating how the hydraulic fractures were modeled with the DFM and CVFEM. This sketch focusses only on the finite elements and control volumes in the region near the hydraulic fracture. The triangles are the finite elements used to discretize the domain, while the dotted lines enclose the control volumes that are implicitly or numerically constructed around each node (or vertex) in the domain. In the 2D geometrical domain of the reservoir, the fracture is represented as a line. However, in the computational model, I fully account for the volume of the fractures using the length, width and height of the fracture.

For a 2D reservoir, I can write the residual form of the 1D mass balance equation for each species in the fracture in the same form as Eq. 4.46:

$$R_i^f = \Delta t \sum_{f=1}^{n_f} h\, w_f\, y_i^f c^f \frac{k_f}{\mu_g^f} \left(\frac{p_j^f - p_i^l}{/\bar{ij}/} \right) - h\, l_f\, w_f \left[\left(\phi^f c^f\right)^{k+1} - \left(\phi^f c^f\right)^{k} \right] \approx 0 \quad (4.77)$$

The residual equation for the fracture, given in Eq. 4.77 is simply added to the matrix residual equation, given in Eq. 4.46, and the equation is solved as detailed in the previous section. It is worth noting that this simple addition of the two equations ensures that the

flux across any pair of fracture nodes is added to the flux on the interface between the two control volumes centered on these two nodes. So, the total flux across the surface of any control volume with a fully penetrating fracture includes the additional flux between the control volume and all neighboring control volumes connected by a fracture. To ensure that the accumulation of reservoir fluid in the fracture is correctly modeled, I subtract the volume of each fracture segment from the volume of the control volume in which the fracture segment is located. This reduced volume is the bulk volume of the matrix which is used in Eq. 4.46. Syihab (2009) provides more details on this volume correction, as well as the treatment of the geometrical and computational domains.

5. RESULTS AND ANALYSES

This section discusses the results obtained from the numerical simulations performed in this work. Some of the results presented in this chapter were presented in Olorode et al. (2017a)[1], Olorode et al. (2017b)[2], and Olorode et al. (2017c)[3]. The physical description of the single vertically-fractured shale-gas well modeled is given in Figures 4.3 and 4.4. All the results presented in this section assume that the permeability of the nanoporous organic pores are so small that I do not expect significant advective transport from the organic pores into the inorganic pores, so I neglect the advective term in Eq. 3.3. Furthermore, to avoid the complexities associated with the multi-component surface diffusion from the organic pores into the inorganic pores, I neglect the second term in Eq. 3.3. These two assumptions imply that the simulation results presented are based on the coupling of the organic pores to the inorganic pores by molecular diffusion; but I account for the contribution of the adsorbed fluids to storage in the accumulation terms on the right-hand-side of Eq. 3.10. The degree of coupling between the organic and inorganic pores is therefore controlled by the coefficient of the concentration gradient between these pores. The expression for this "coupling coefficient" ($\mathcal{C}_c$) can be obtained from Eq. 3.3 as:

$$\mathcal{C}_c = l_m^T \frac{\epsilon_{kf}\phi}{\tau} D^{i,O} \tag{5.1}$$

[1]Part of the simulation results for non-deformable shales is reprinted with permission from "Compositional Reservoir-Flow Simulation for Organic-Rich Gas Shale" by O. M. Olorode, I. Y. Akkutlu, and Y. Efendiev, 2017. SPE Journal, Copyright 2017 by SPE.

[2]Part of the simulation results for deformable shales is reprinted with permission from "Modeling of Compositional Gas Transport in Shale as a Deformable Porous Medium" by O. M. Olorode, I. Y. Akkutlu, and Y. Efendiev, 2017. Poromechanics, VI, 1984-1991, Copyright 2017 by American Society of Civil Engineers.

[3]Part of the results for the storage of CO_2 in depleted organic source rocks is reprinted with permission from "A Compositional Model for CO_2 Storage in Deformable Organic-Rich Shales" by O. M. Olorode, I. Y. Akkutlu, and Y. Efendiev, 2017. SPE Europec featured at 79th EAGE Conference, Copyright 2017 by SPE.

Substituting the definition of l_m^T given in Eq. 3.21, I can write Eq .5.1 as:

$$\mathcal{C}_c = \frac{\epsilon_{kf}\phi}{\tau}\,\mathcal{G}_A\mathcal{T}_f\left(V_b^k\right)^{-2/3}\,D^{i,O} \tag{5.2}$$

Given the expected uncertainties in tortuosity, τ and the kerogen geometric factor $\mathcal{G}_A$, I can group these two terms together by defining a coupling constant, ζ as follows:

$$\zeta = \frac{\mathcal{G}_A}{\tau} \tag{5.3}$$

This allows me to perform sensitivity studies on ζ, which is basically an unknown constant in the simulation model. Substituting this definition for ζ into Eq. 5.2 yields:

$$\mathcal{C}_c = \zeta\,\epsilon_{kf}\phi\mathcal{T}_f\left(V_b^k\right)^{-2/3}\,D^{i,O} \tag{5.4}$$

For completeness, note that ϵ_{kf} and ϕ could be estimated from petrophysical analysis and are considered as inputs (specified in Table 5.1) in this work. To estimate the kerogen bulk volume, V_b^k, I use Eq. A.8, which is derived in Appendix A. $\mathcal{T}_f$ is estimated using Eq. 3.20, and $D^{i,O}$ is estimated from the Maxwell-Stefan diffusion model, as described in the section on Maxwell-Stefan Diffusion.

5.1 Model Validation

This section focuses on the validation of the simulator developed for the modeling of multi-component gas in deformable and undeformable source rocks. Table 5.1 outlines the reservoir parameters for the model studied in this work. These parameters are based on Barnett shale-gas reservoir properties obtained from Akkutlu and Fathi (2012), Olorode et al. (2013) and Hu et al. (2015). The sorption parameters were obtained from Ambrose (2011), and the physical dimensions of the reservoir system modeled is given in Figure 4.3.

In all cases simulated, I model the production well as a constant-pressure inner boundary, while the external boundaries of the reservoir are modeled as no-flow boundaries.

Table 5.1: Reservoir and hydraulic fracture parameters

Parameters	**SI Unit**	**Field Unit**
Fracture half-length, x_f	450 m	1476 ft
Fracture width, w_f	3 mm	0.00984 ft
Reservoir thickness, h	100 m	330 ft
Matrix permeability, k_m	1.0 x 10^{-19} m^2	1.0 x $10^{-}4$ md
Fracture permeability, k_f	5.0 x 10^{-11} m^2	5.0 x 10^4 md
Matrix porosity, ϕ	0.04	0.04
Fracture porosity, ϕ_{frac}	0.33	0.33
Temperature, T	50^{o}C	122^{o}F
Well radius, r_w	0.1 m	0.32 ft
Initial pressure, p_i	2.76 x 10^7 Pa	4,000 psia
Initial mole fractions, z_i	[0.899,0.1,0.001]	[0.899,0.1,0.001]
Bottomhole pressure, p_{wf}	6.9 x 10^6 Pa	1,000 psia
TOC	5%	5%
ϵ_{kp}	0.35	0.35
Tortuosity, τ	7	7
$G_{sL,i}$	[184.5, 299.7, 589.6] g-mol/r·m^3	[56, 91, 179] scf/ton
Langmuir Pressure, $p_{L,i}$	[10.8, 5.6, 5.8] x10^6 Pa	[1562, 811, 844] psi
Sorbed Gas Density, $\rho_{s,i}$	[371, 460, 486] kg/m^3	[23.2, 28.7, 30.3] lb/cuft
Bulk Density, ρ_b	2,500 kg/m^3	1.56 x 10^5 lb/cuft
Young's Modulus, E	40 GPa	5.8 x 10^6 psia
Poisson ratio, ν	0.25	0.25
Viscoelastic coefficient, η	3.4 x 10^9 MPa-s	493 x 10^9 psi-s
Biot coefficient, α	0.2	0.2
Initial displacements	0 m	0 ft
Initial stress, σ_x and σ_y	0 Pa	0 psia
Initial fracture width, w_f	0.003 m	0.01 ft

5.1.1 Validation of the simulation model for gas transport in a non-deformable porous medium

In this section, I discuss the validation of the numerical simulator developed (called "TamCVFEM") against Eclipse 300, a commercial compositional reservoir simulator. The model compared corresponds to a tight-gas reservoir with a porosity of 4%, a permeability of 100 nD, and without an organic matrix. Additional details on the tight-gas reservoir can be found in Table 5.1. Figures 5.1a and 5.1b show a comparison of TamCVFEM with Eclipse 300 on rate and cumulative plots, respectively. The differences in the production rates at early time (in Figure 5.1a) could be attributed to numerical differences between the discretization schemes used in the two simulators. The hydraulic fracture is modeled explicitly in Eclipse 300, while the DFM is used in TamCVFEM. These plots show that the developed simulator is capable of modeling a compositional gas reservoir with hydraulic (or discrete) fractures.

5.1.2 Validation of the coupled flow and geomechanics simulation with published analytical solutions

This section focuses on the validation of the coupled geomechanics and flow simulator against known analytical solutions. One of the most popular consolidation problems with published analytical solutions is the Terzaghi's consolidation problem Terzaghi (1943). This problem involves applying a constant overburden stress, σ on a 100% water-saturated soil sample with thickness, 2h. The overburden stress is applied suddenly at time, t = 0, and both the top and bottom of the soil sample are maintained at a constant pressure of zero. The bottom of the soil sample is fixed at a constant vertical displacement of zero. The analytical solution for the Terzaghi problem is sometimes modeled as half of the total thickness (h) as in Verruijt (2016). In this work, the full thickness (2h) of the soil sample is used, and the corresponding analytical solution is discussed in Wan (2002). The details

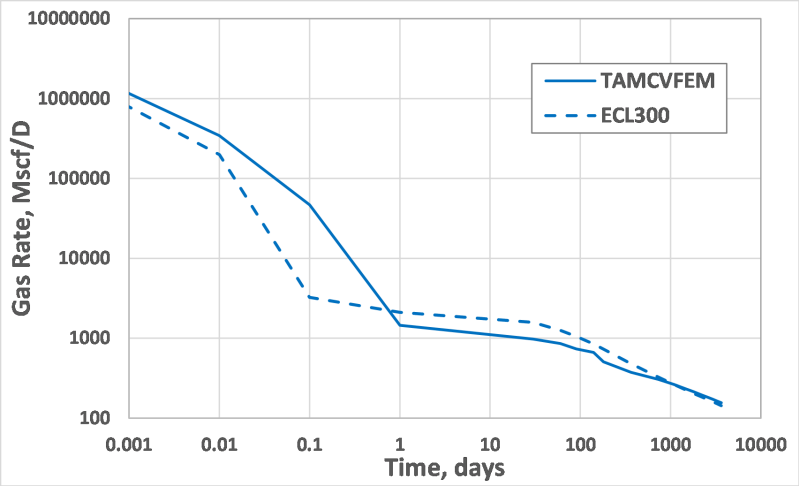

(a) Gas Production Rate Plots.

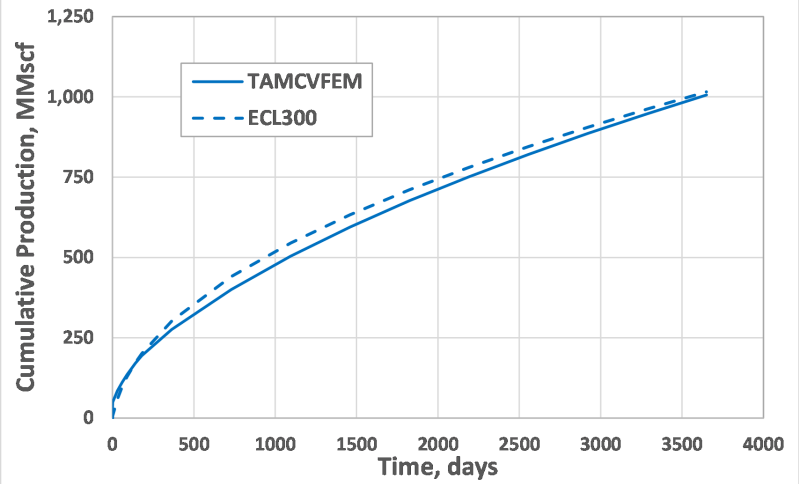

(b) Cumulative Gas Production Plots.

Figure 5.1: Comparison of the production plots validates TamCVFEM against Eclipse 300.

of the derivation of the analytical solution is presented in Terzaghi (1943) and Verruijt (2016). The final form of the analytical solution is given as:

$$\frac{p}{p_0} = \frac{4}{\pi}\sum_{j=1}^{\infty}\left\{\frac{(-1)^{j-1}}{2j-1} cos\left[(2j-1)\frac{\pi\,(h-z)}{2h}\right] exp\left[-(2j-1)^2\frac{\pi^2 c_v t}{4h^2}\right]\right\} \tag{5.5}$$

Table 5.2 outlines the parameters used in the modeling of the Terzaghi problem, while Figure 5.2 presents a sketch of the problem description, as well as the actual grid which is modeled in this work. To model the Terzaghi problem, I modeled single-phase water in a single-porosity matrix instead of the multi-continuum, multi-component simulation of compressible gas, which is modeled in all other cases presented in this dissertation. Figure 5.3 shows the validation of the coupled geomechanics and flow simulator against the analytical solution to the Terzaghi problem. The points in this figure correspond to the numerical solution at specific dimensionless heights in the domain, while the solid curves correspond to the analytical solution presented in Eq. 5.5. The slight differences at early times could be attributed to the fact that the sudden stress to be applied at time, t = 0^+ was only applied over all the time-steps taken in the simulation model. The simulation was run at a dimensionless time ranging between 0 and 1, and in increments of 0.01.

In addition to these validations, Appendix C gives some basic verification of the numerical model by performing sensitivities with respect to the mesh sizes and mesh orientation.

5.2 Study of Storage and Transport Mechanisms in Non-deformable Source Rocks

This section focuses on the numerical study of storage and transport mechanisms in non-deformable source rocks. This implies that the coupled mechanical deformation of the rock matrix and fractures are neglected in the results presented in this section.

Table 5.2: Input Parameters for the Terzaghi Problem

Parameters	**SI Unit**	**Field Unit**
Young modulus, E	1.0 x10^9 Pa	1.45 x10^5 psi
Poisson ratio, ν	0.2	0.2
Biot coefficient, α	1.0	1.0
Fluid viscosity, μ	1 x10^{-3} Pa. s	1 cp
Fluid density, ρ_f	1000 kg/m^3	62.4 lb/cuft
Permeability, k	5.0 x10^{-14} m^2	50 mD
Porosity, ϕ	0.3	0.3
Initial pressure, p_i	0 Pa	0 psi
Overburden stress, σ	2.125 x10^6 Pa	308 psi

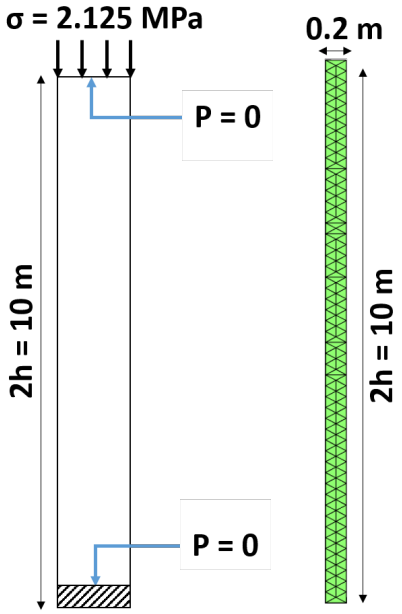

Figure 5.2: The left figure shows a sketch of the Terzaghi Problem while the actual grid used in this work is shown on the right.

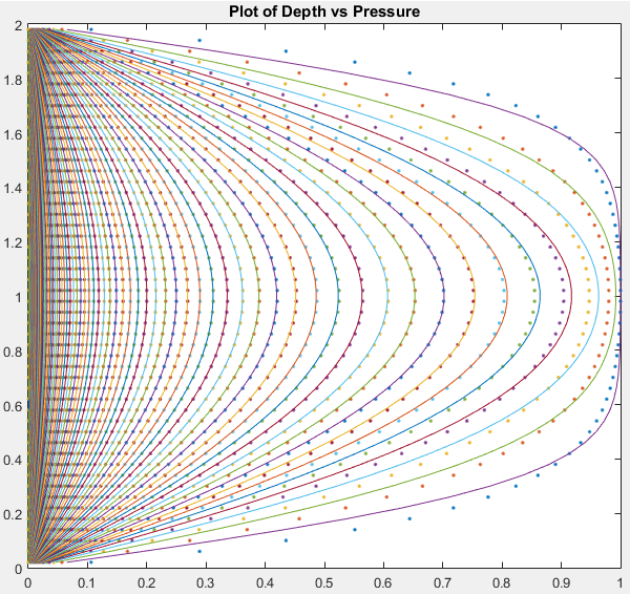

Figure 5.3: Validation of the coupled geomechanics and flow simulator against the analytical solution of the Terzaghi problem. The simulation results are shown as dots, while the analytical solutions are shown as curves.

5.2.1 Contribution of molecular diffusion to transport in the inorganic shale matrix

In the results shown in Figures 5.4a and 5.4b, I model a system that corresponds to the inorganic matrix of a shale-gas reservoir, that is, $\epsilon_{kp} = 0$. The idea is to evaluate the relative contribution of molecular diffusion as a means of transport of fluids in the inorganic matrix of a shale-gas reservoir. The dotted lines in Figure 5.4a correspond to the cases where I model advective transport only, while the solid lines correspond to the scenarios where I model both molecular diffusion and advection. The logarithmic scale in Figure 5.4a tends to amplify the differences between production profiles at very low values, and it compresses or masks the differences at high values of production rate. Figure 5.4a and Figure 5.4b (as well as all other simulations in this work) indicate that the contribution of the diffusive transport in the inorganic pores is negligible at 100 nD, which is the base case that could be representative of a resource shale. The results suggest that the contribution

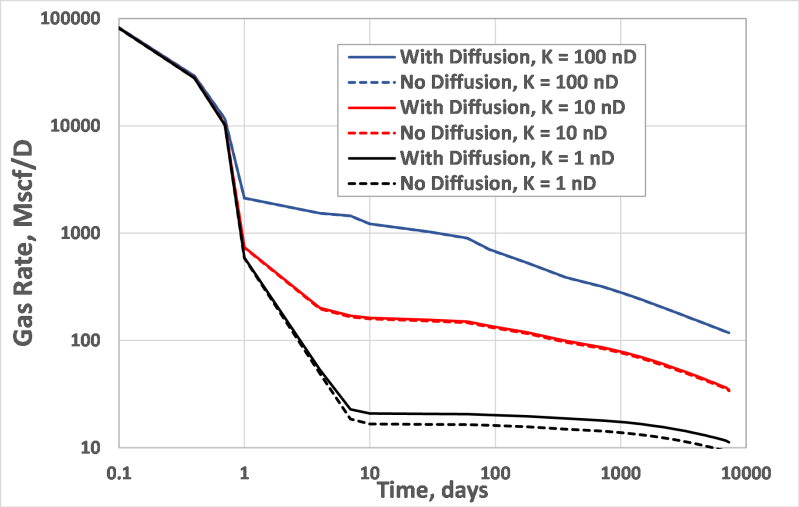

(a) Flow Rate.

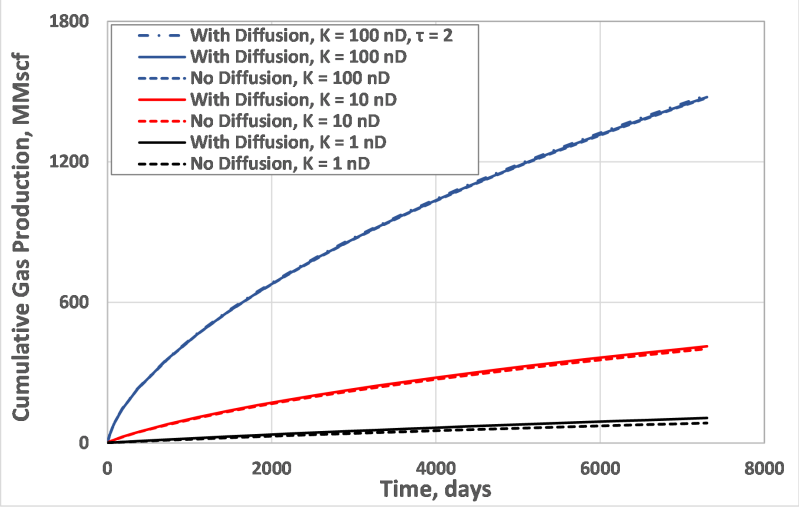

(b) Cumulative Production.

Figure 5.4: Effect of Diffusion on Shale-gas Production. The results indicate that diffusion is not important in the inorganic pores at permeability values of 100 nD or higher.

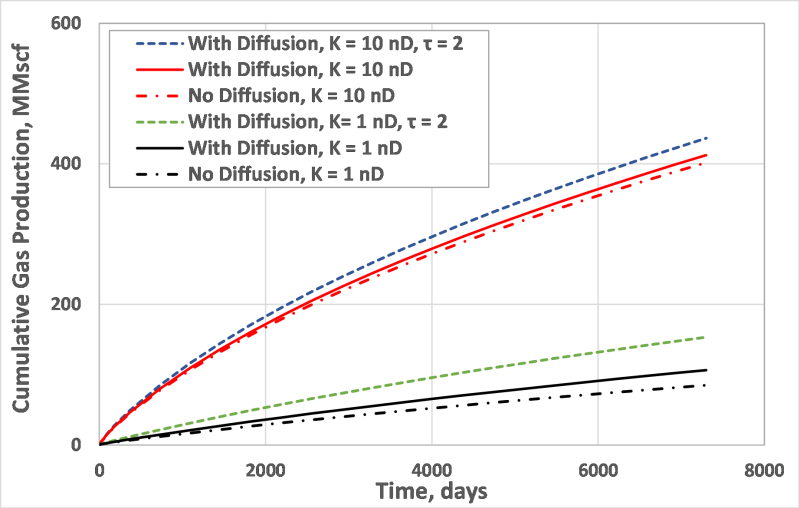

Figure 5.5: The contribution of diffusion to production appears increasingly significant at lower permeability values (10 nD or lower).

of diffusive transport to production could be higher at lower permeability values (10 nD and 1 nD). However, in addition to the production plots with and without diffusion at 100, 10 and 1 nD, I added a case at 100 nD, where the tortuosity was set to 2 (instead of the base-case value of 7), which is the lowest value in the range given in Table 5.1. The result, as well as all other cases at 100 nD showed that advective transport dominates diffusive transport in an inorganic matrix with a permeability of 100 nD.

It is important to point out that the relatively large cumulative production values of the 100 nD case could mask the magnitude of the contribution of molecular diffusion contribution at 10 nD and 1nD. Figure 5.5 gives the corresponding cumulative production curves without the 100 nD cases. Additionally, Figure 5.5 shows the increased contribution of molecular diffusion if the tortuosity is set to 2 instead of the base-case value of 7.

Virtually all the simulation cases performed at 100 nD appeared almost indistinguishable on the log-log rate plots, so all other results presented in this dissertation show the cumulative gas production plots only. To clarify, although the results presented in this sec-

tion show that advective transport dominates molecular diffusion in an inorganic matrix with a permeability of 100 nD, this is not the case in the organic pores where diffusive transport could be the dominant transport mechanism.

5.2.2 Effect of the coupling constant on shale-gas production

I defined the coupling constant, ζ as the ratio of the geometric factor $\mathcal{G}_A$ to the tortuosity, τ in Eq. 5.3. The section on shape factor, as well as Appendix B discusses the computation of the geometric factor, $\mathcal{G}_A$. Figure 5.6 shows the production performance of the representative Barnett shale studied at different values of ζ. I observe that the plot shows observable increase in cumulative production at relatively low values of ζ. At ζ values greater than 27, I do not observe any significant increases in cumulative production. This indicates that beyond a particular level of coupling between the organic and the inorganic matrix, further increases in the magnitude of the coupling does not result in increased production because the organic and inorganic pores could be said to be "fully coupled" at

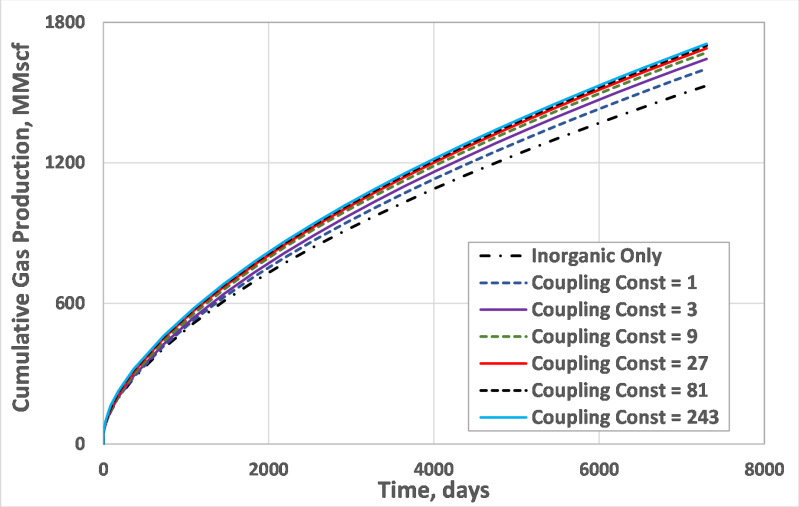

Figure 5.6: The sensitivity runs at increasing values of the coupling constant shows that the increase in cumulative production at increasing levels of the coupling constant becomes less significant at higher values of the coupling constant.

these values of the coupling factor. A possible extension of the interpretation of this result is a hypothesis that further increases in the transport of gases in the nanoporous organic matrix (due to surface diffusion, or additional adsorbed-phase transport) may not lead to any significant increase in gas production if the organic pores are already fully coupled with the inorganic pores.

Figure 5.7 shows the corresponding pressure profiles at the different values of ζ. There was no observable difference in the inorganic pore pressure profiles, so I show only one inorganic pore pressure profile together with the organic pore pressure profiles at the corresponding ζ values. All pressure profiles shown in Figure 5.7 include the correction for the pore volume occupied by the adsorbed gas molecules. Given the negligible contribution of diffusion to transport at a matrix permeability of 100 nD, the simulated changes in the composition of the produced fluid was negligible.

5.2.3 Importance of the nonlinearity in the coupling coefficient

In this section, I study the effect of the nonlinearity in the terms comprising the coupling coefficient. The expression for the coupling coefficient is given in Eq. 5.4. An inspection of the equation shows that the nonlinear terms include the transient factor, $\mathcal{T}_f$ and the diffusion coefficient. The results presented in Figure 5.8 indicate that the nonlinearities in the coupling coefficient result in an increase in the estimated production, and this effect is more significant at lower degrees of coupling between the organic and inorganic matrices. This is expected because the transient factor is always greater than 1, and only gets equal to one at pseudo-steady state. Additionally, the inverse pressure-dependence of the diffusion coefficient is such that the diffusion coefficient increases as pressure drops during production.

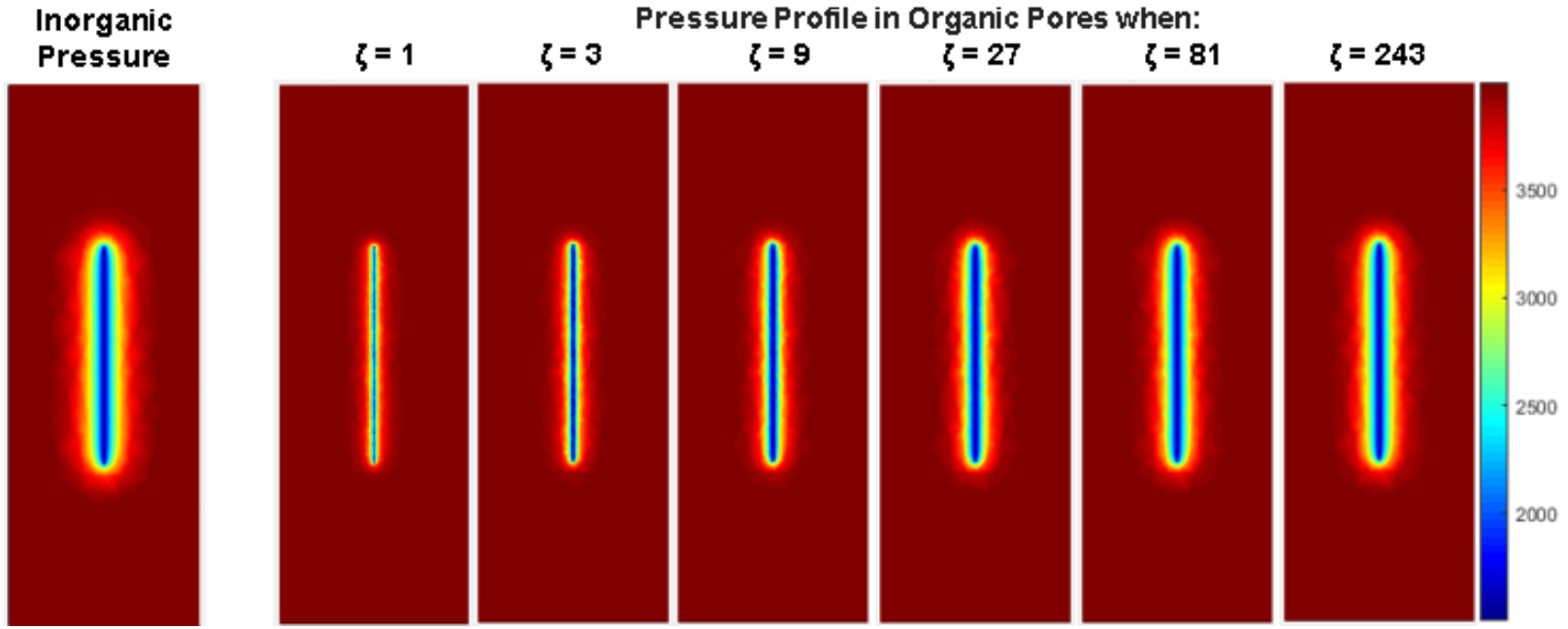

Figure 5.7: Organic pore pressure profile after 20 years of production show that the organic matrix is depleted more at higher values of the coupling constant, ζ. I only show one inorganic matrix pressure profile because there is no observable difference in the inorganic pore pressure profile at the different values of ζ.

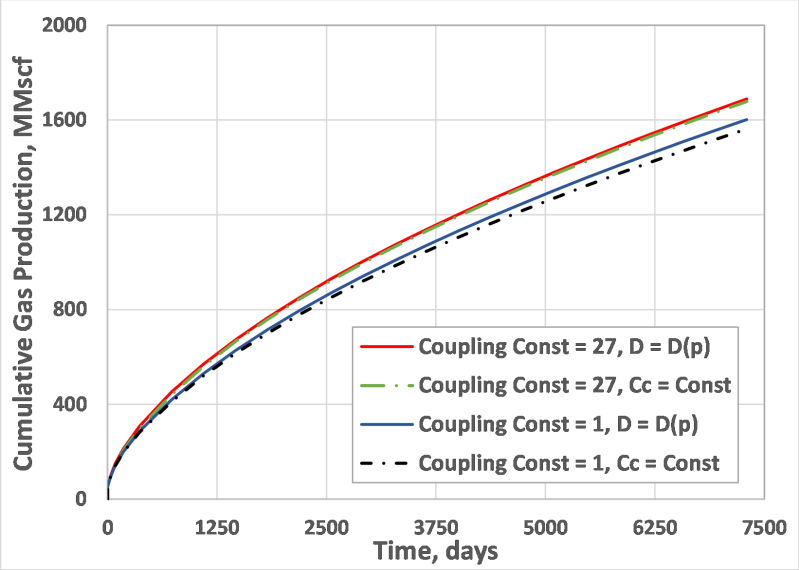

Figure 5.8: The nonlinearities in the coupling factor could be more significant at lower degrees of coupling between the organic and inorganic matrices.

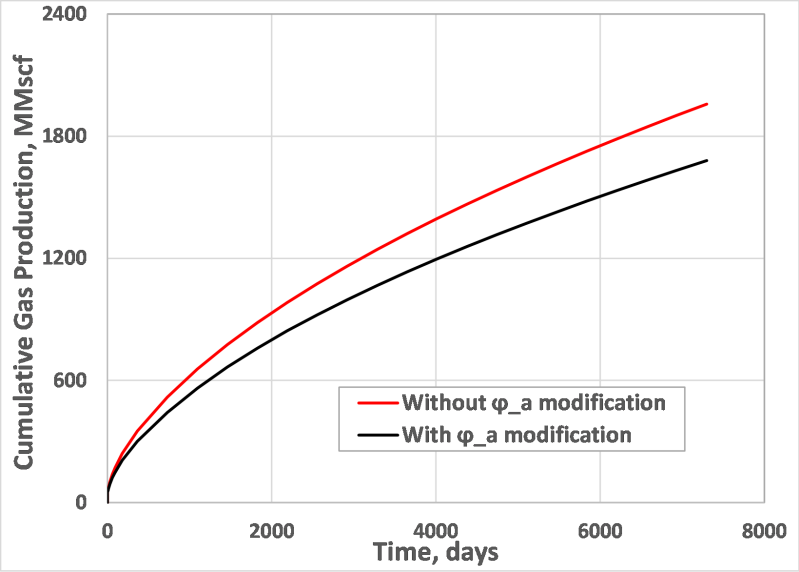

Figure 5.9: Comparison of a simulation run with and without the reduction of the free gas pore volume by the adsorbed gas pore volume shows that the absence of this correction could lead to an over-estimation of the cumulative production by about 17% at a flowing bottomhole pressure of 2,000 psia.

5.2.4 Impact of the correction for the pore volume occupied by sorbed gas molecules

Figure 5.9 shows the impact of the correction of the free gas pore volume to account for the pore volume taken up by the gas molecules adsorbed on the surfaces of the organic pore walls. The comparison of the case with and without the reduction of the free gas pore volume by the adsorbed gas pore volume shows that the absence of this correction could lead to an over-estimation of the cumulative production by about 17%. This is because the pore volume available for gas storage in the free state is implicitly larger by an amount that is equal to the pore volume taken up by the adsorbed gas molecules. From the results shown in Figure 5.9 I can infer that it is important to account for the pore spaces occupied by sorbed gas molecules in organic-rich resource shales. The details on how this correction was implemented is discussed in Section 3.1.

5.2.5 Contribution of kerogen to production in shale-gas reservoirs

Given the definition of ϵ_{kp} as the ratio of the kerogen pore volume to the total pore volume, Figure 5.10 shows the contribution of kerogen to production when the organic pores account for 35% of the total pore volume (in Figure 5.10a) and when the organic pores account for 50% of the total pore volume (in Figure 5.10b). The black dotted lines in both figures correspond to the cases where I essentially take out all of the organic pores, and model production from the inorganic pores only. The solid red lines in both figures correspond to the cases where I model both the organic and inorganic pores at the base-case parameter levels, and with a coupling constant (ζ) of 27. The difference between the solid red line and the dotted black line gives the contribution of the organic pores to the cumulative production. The dotted blue line in both plots show the production performance for a system where the bulk volume occupied by kerogen is replaced by a corresponding inorganic bulk volume. The fact that the dotted-blue line is higher than the solid red line in both plots indicates that for a given bulk volume, the inorganic pores tend to produce more

gas than the organic pores, even though I expect more gas storage in the organic pores (due to adsorption). The higher production from the dotted-blue line in comparison to the solid red line could be attributed to the observation that the fractional recovery from inorganic pores are generally much larger than the corresponding fractional recovery from organic

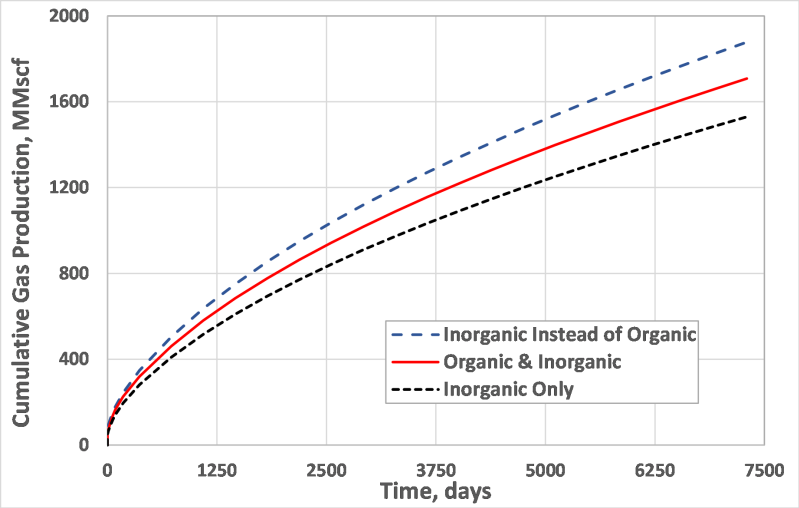

(a) Cumulative gas production plots at ϵ_{kp} = 0.35

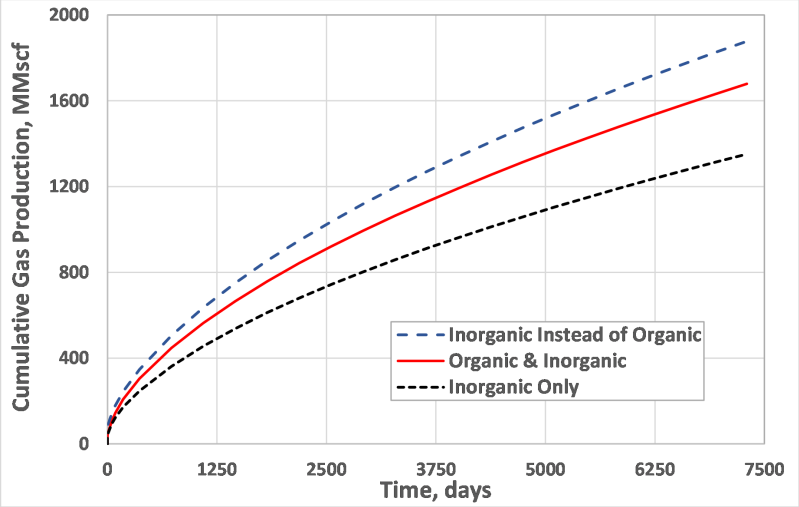

(b) Cumulative gas production plots at ϵ_{kp} = 0.5

Figure 5.10: Cumulative gas production plot shows that the dispersed kerogen in shale-gas reservoirs can contribute appreciably towards production.

pores at typical average reservoir pressures in shale-gas reservoirs. The next section studies the fractional recoveries associated with both free and adsorbed gases, and shows that the contribution of the adsorbed gases in the organic nanopores could be curtailed by the relatively high average reservoir pressures in shales. Another possible reason for the lower production from an organic pore in comparison to an inorganic pore could be related to the curtailment of the production from the organic pores by the degree of coupling between the inorganic and the organic pores. Additionally, note that the advective transport expected in the inorganic matrix, could play a major role in accelerating the rate of production from a reservoir with no organic pores, in comparison to another reservoir with some kerogen. This is because kerogen typically lacks micro-cracks and laminations that could contribute to accelerated advective transport. The observation that advective transport dominates diffusive transport at 100 nD or more, while diffusion gets increasingly more important below 10 nD suggests that we might have predominantly advective transport in the inorganic pores, and predominantly diffusive transport in the organic pores. This difference in the expected transport mechanisms in the organic and inorganic pores suggests that it might be crucial to model these two continua differently, as is done in this work. A simple homogenization of the organic and inorganic continua (using a single-porosity simulation model, for example) without accounting for the distinct storage and transport mechanisms peculiar to each of these continua could lead to inaccurate results. This is because an assumption of advective transport in the homogenized continuum for example, could over-estimate the transport term, and lead to an overestimation of the production performance using such a single-porosity model.

A comparison of Figure 5.10a to Figure 5.10b indicates that the contribution of kerogen towards cumulative production appears to be more significant when more of the pores in the total system is in the kerogen pores. This is expected given that the kerogen tends to hold more free gases in addition to the adsorbed gases at higher values of ϵ_{kp}. It is worth

noting that a high value of ϵ_{kp} values does not automatically imply that the organic pores are continuous at the reservoir simulation grid-block scale. It could however be indicative of a lack of abundance of macropores and/or micro-cracks in the inorganic matrix. The generally low TOCs (usually less than 10%) even when ϵ_{kp} values are high, could indicate that kerogen is still dispersed in the inorganic matrix, which has a much higher volume fraction than the organic matrix.

5.2.6 Analysis of fractional recovery

This section seeks to study the relative contribution of free and adsorbed gases to production, with the idea of explaining the results shown in Figure 5.10a. The results in Figure 5.11a were computed based on the volumetric shale gas-in-place calculations presented by Ambrose et al. (2012) and Hartman et al. (2012). These fractional recoveries were computed by subtracting the free and sorbed gas amounts at any pressure from the corresponding amounts at initial pressure, and dividing the result by the total (free+sorbed) gas amount at the initial conditions. In Figure 5.11b, I focus on the limited range of average reservoir pressure that was observed from the numerical simulations performed. The line plots are the analytical estimates from Figure 5.11a, while the dotted points show the corresponding fractional recoveries estimated from the numerical simulations performed. The average pressure at a given time is calculated using the pressure values within the radius of investigation. The results indicate that the free-gas fractional recoveries are much larger than the sorbed-gas recoveries. At the estimated average reservoir pressure of about 3,300 after 20 years of production, the simulation results indicated that the free-gas fractional recovery is about 6.3 times larger than that of the sorbed gas, while the analytical calculations showed it is about 4.7 times larger. The main difference between the analytical and numerical estimates of fractional recovery is that the numerical estimates account for the resistances to flow (and associated transient flow effects) due to the permeability

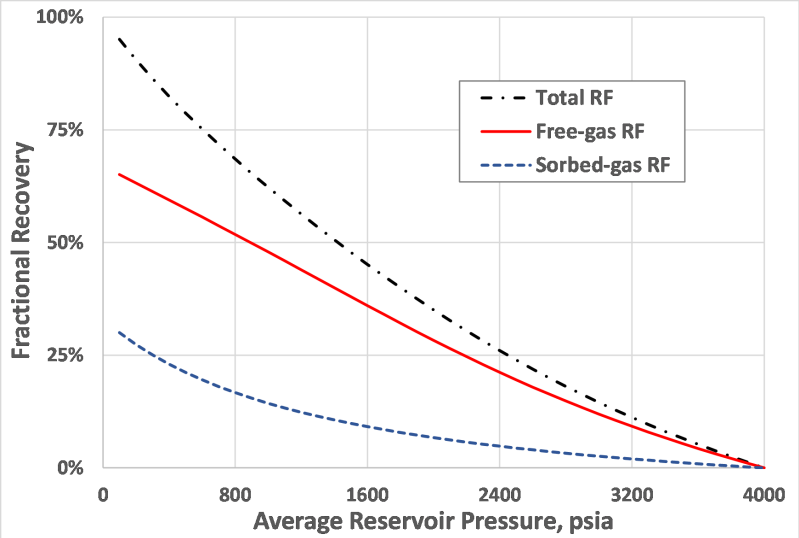

(a) Fractional recoveries estimated from shale-gas in place calculations.

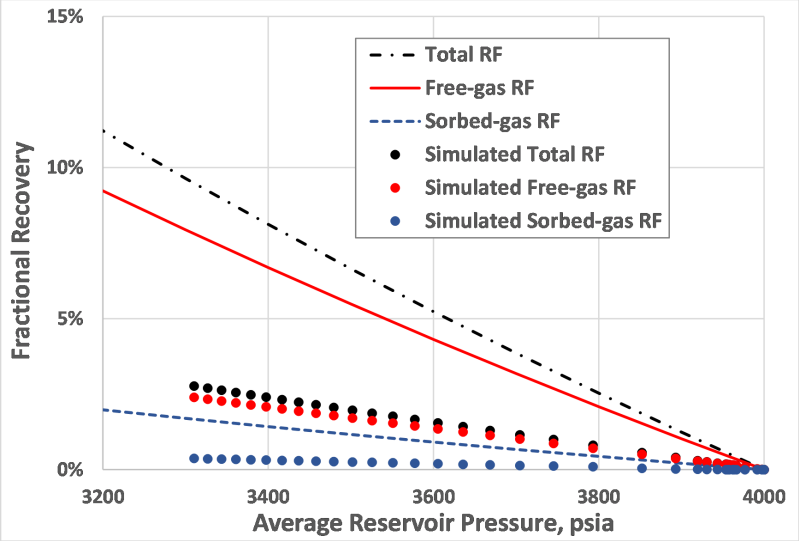

(b) Comparison of analytical to simulation-based fractional recovery estimates.

Figure 5.11: The fractional recoveries indicate that the contribution of sorbed gas to total recovery could be limited at relatively high average reservoir pressures. The increase in this contribution at lower pressures could be related to the shape of the Langmuir Isotherm.

and diffusivity of the system, while the analytical estimates essentially correspond to a "tank-model" that does not account for the resistance and transient effects associated with the transport mechanisms in the reservoir.

It is worth noting that free gas molecules exist in both inorganic and organic pores. Although the free gases in the organic pores could be released at rates similar to the rate of production of free gas from the inorganic pores (if the organic and inorganic pores are fully coupled, with high ζ values), the additional production from desorption could be limited by the low recoveries at the relatively high average pressures expected in strongly-transient shale-gas reservoirs. The shape of a typical adsorption/desorption isotherm is such that the adsorbed gas amount flattens at high pressures, but shows relatively steep declines only at very low pressures, which may be much lower than typical flowing bottomhole pressure values. This explains why the amount of sorbed gas desorbed at typical average reservoir pressures could be much less than the free gas produced. These average reservoir pressures were estimated using a volume-weighted average of the cell pressures in all the grid blocks within the drainage area observed in the simulated pressure profiles.

5.2.7 Contribution of diffusion at lower flowing bottomhole-pressures

In an earlier section, I showed that the contribution of diffusion to flow in the inorganic pores could be dominated by the advective transport. In Figure 5.12a, I show a slightly increased contribution of diffusion to flow at a lower flowing bottom-hole pressure of 500 psia, in a system with both organic and inorganic pores. The profile for the case with a constant diffusion coefficient is practically identical to the case with a pressure-dependent diffusion coefficient at a flowing bottomhole pressure of 1,500 psia, while a slight difference is observed at a pressure of 500 psia. This can be attributed to the increased contribution of desorption to production at lower pressures, as explained in the previous section. I expect this difference to be more significant at an even lower pressure, but it might be un-

realistic to produce a well at a much lower pressure. The typical sharp increase in pressure (shown in Figure 5.7) away from the fracture surface indicates that the increased desorp-

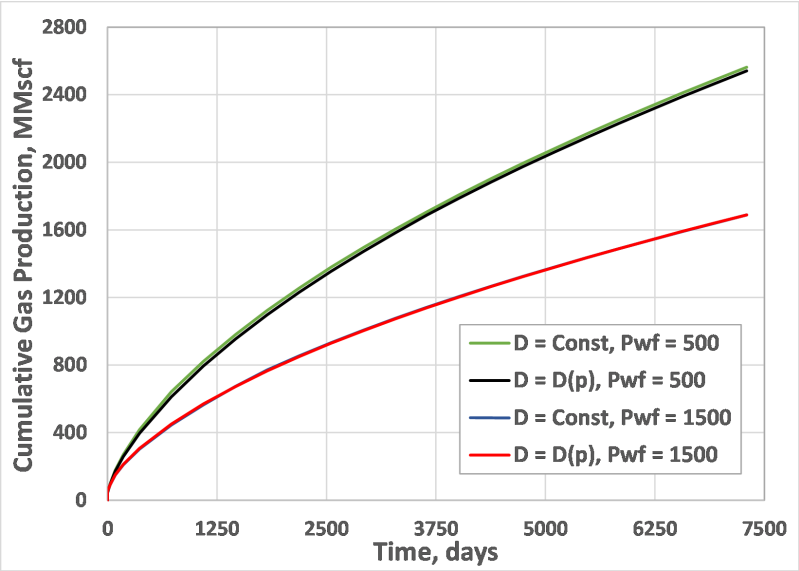

(a) Diffusion contribution increases at lower flowing bottomhole pressures.

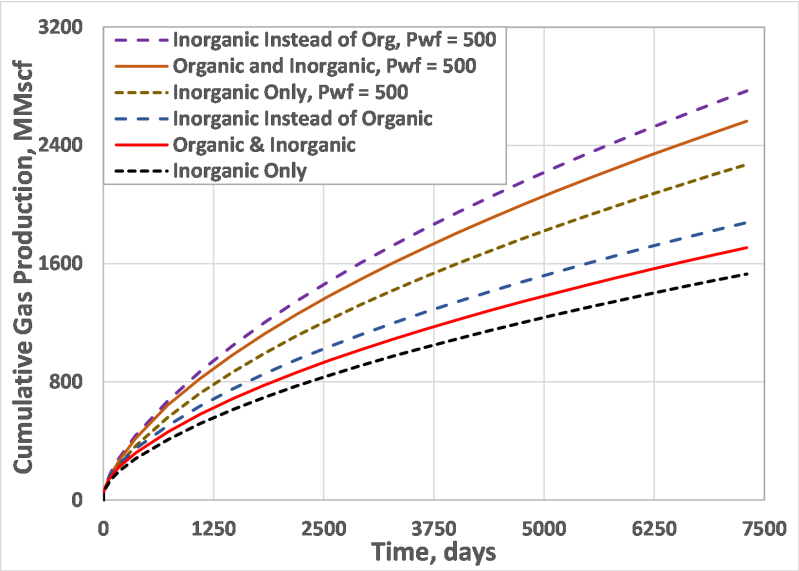

(b) Comparison of production profiles with and without kerogen at flowing bottomhole pressures of 1500 psi and at 500 psi.

Figure 5.12: The simulation results indicate that the contribution of diffusion could be more significant at lower flowing bottomhole pressure values.

tion at the lower pressure of 500 psi could be limited to a small region very close to the fracture faces. Figure 5.12b shows the production performance with and without organic pores at a bottomhole pressure of 500 psia and at the base-case bottomhole pressure of 1,500 psia. The lowest three production profiles correspond to the cases shown in Figure 5.10a, where the bottomhole pressure is maintained at 1,500 psia. The production profile shows higher production at a flowing bottomhole pressure of 500 psia, as expected given the increased pressure drawdown in this case.

5.2.8 Analysis of Péclet number

In this section, I focus on the analysis of the relative contribution of advective and diffusive transport in the base-case simulation model, with a matrix permeability of 100 nD, using Péclet number. By definition, Péclet number is the ratio of the rate of advective transport to the rate of diffusive transport. Figure 5.13a gives the plot of the Péclet number for methane in the inorganic pores versus the orthogonal distance away from the fracture face. Each curve on the plot corresponds to a particular snapshot in time. The relatively high values (greater than 10) of the Péclet number indicates that the rate of advective transport is much faster than the rate of diffusive transport in the inorganic pores. The gradual drop in the curves as time evolves indicates that the contribution of diffusion to transport tends to increase as the duration of the production increases. The observation that the Péclet number decreases in the direction of the fracture surface, indicates that the contribution of diffusion to transport increases in the direction of the fracture surface. This contribution of diffusion is greatest in the proximity of the fracture surface, as indicated by the observation that the Péclet number is lowest right by the fracture surface. A physical explanation for the maximum contribution of diffusive transport at the fracture surfaces is related to the typical sharp drop of the grid-block pressures to the flowing bottomhole pressure in the vicinity of the fracture surface. When this happens, the pressure gradient

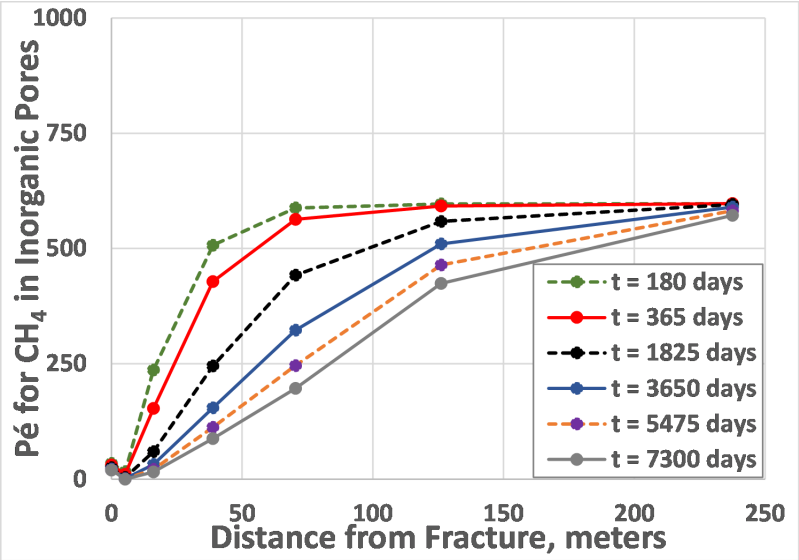

(a) Methane Péclet number in the inorganic pores.

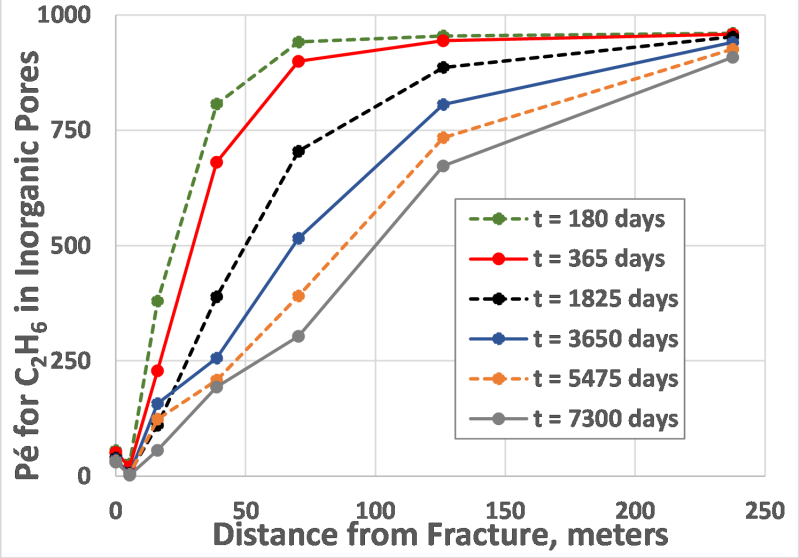

(b) Ethane Péclet number in the inorganic pores.

Figure 5.13: Péclet number for methane and ethane in the inorganic pores indicates that advective transport could be the dominant transport mechanism in the reservoir.

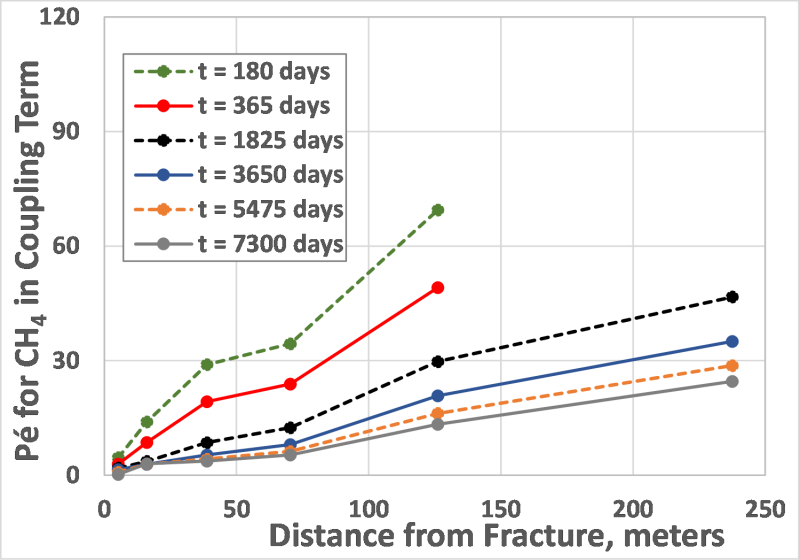

(a) Modified-Péclet number for methane in the coupling term.

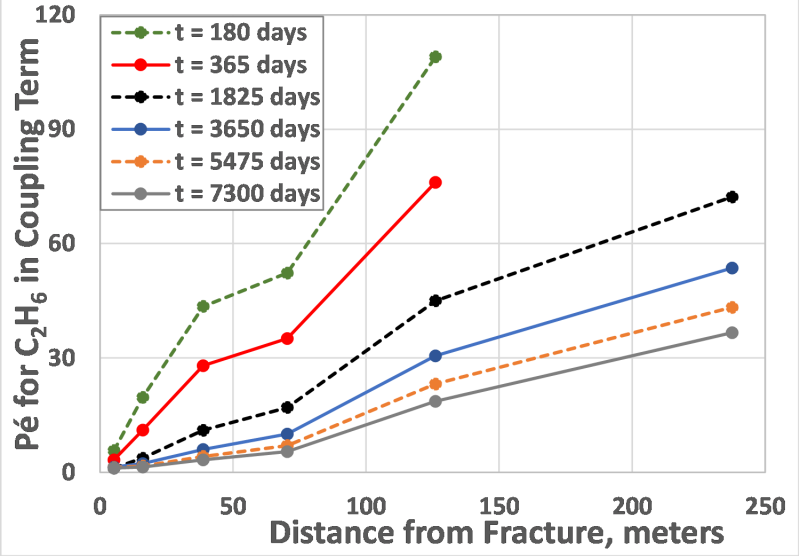

(b) Modified-Péclet number for ethane in the coupling term.

Figure 5.14: The Modified-Péclet numbers for methane and ethane indicate that the rate of advective transport in the inorganic pores is much faster than the rate at which gas is released from the organic pores into the inorganic pores.

term becomes small in magnitude, leading to a reduction in the advective transport, and a consequent decrease in the Péclet number. A similar trend is observed in the Péclet number for ethane, which is given in Figure 5.13b. Comparing Figure 5.13b to Figure 5.13a, I observe that the Péclet numbers for ethane are generally greater than the Péclet numbers for methane. This is expected because methane is lighter than ethane, and its rate of diffusion is generally faster than that of ethane under the same conditions.

In Figure 5.14, I introduce the "modified-Péclet number", which is simply the ratio of the rate of advective transport in the inorganic pores to the rate at which gas is released from the organic pores into the inorganic pores. The results indicate that the rate of advective transport in the inorganic pores is faster than the rate at which gas is released from the organic pores into the inorganic pores. These results are consistent with the results shown in Section 6.8, where I show that the fractional recovery from inorganic pores is generally larger than the fractional recovery from the organic pores. This is because of the higher resistance to flow in the organic pores, the dispersed nature of these organic pores, as well as the curtailed desorption of gas at relatively high pressures, as discussed in Section 6.8. Furthermore, comparing Figure 5.14a with Figure 5.14b, I observe that the modified-Péclet numbers for methane are generally lower than those for ethane, because the rate of diffusion of methane is generally faster than that of ethane under the same conditions.

5.2.9 Effect of the pressure-dependence of permeability and diffusion on production in shale-gas reservoirs

Section 3.3 discussed the modeling of the pressure and composition dependence of molecular diffusion using the Maxwell-Stefan diffusion theory. To model the dependence of the matrix permeability on the stresses in the matrix, I use the Gangi (1978) model,

which is based on a model of a bed of nails. The Gangi model is given as:

$$k = k_o \left[1 - \left(\frac{P_c - \alpha p}{p_1}\right)^m\right]^3 \tag{5.6}$$

where k_o is the matrix permeability at zero confining stress, P_c is the confining stress, α is the Biot constant, p_1 is the maximum stress at which the bed of nail (or micro-crack, in the context of this work) closes completely, and m is a measure of the resistance of the micro-cracks to closure under confining stresses.

Figure 5.15 gives the cumulative production plot for the cases run to study how gas production is affected by the pressure-dependence of the diffusion coefficient, and the stress-dependence of permeability. The dotted lines correspond to the cases where the diffusion coefficients are kept constant, while the solid lines correspond to the cases where the diffusion coefficients are inversely proportional to pressure. As explained in the results on the study of the effect of diffusion, the cases with and without the pressure-dependence of the diffusion coefficient are indistinguishable because diffusive transport appears to be insignificant at a matrix permeability of 100 nD. The inverse proportionality of the Maxwell-Stefan diffusion coefficients comes from the kinetic theory of gases, which was used to obtain the binary diffusion coefficients. In Figure 5.15, the red lines correspond to the cases where I assume that the matrix permeability is constant, while the black lines are representative of the cases where I model the stress-dependence of the matrix permeability using the Gangi's model (Gangi, 1978). The difference in production between the red and the black lines could be attributed to the reduction in matrix permeability in response to pressure depletion during production. Given that the results presented in this section are based on infinite-conductivity hydraulic fractures, I neglect the possible changes in fracture permeability and aperture during production.

All the simulation results presented so far have been based on a single hydraulic frac-

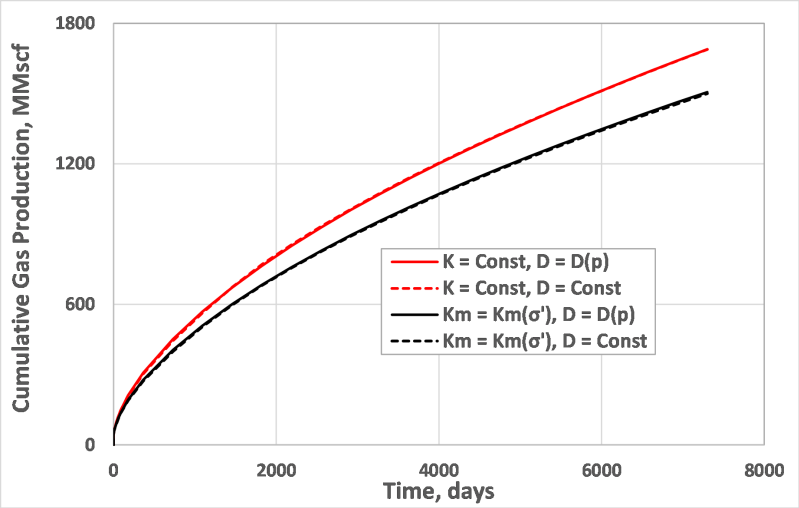

Figure 5.15: Simulation results indicate that the contribution of the pressure-dependence of diffusion is negligible, while the contribution of the stress-dependence of matrix permeability could be significant at an initial reservoir permeability of 100 nD.

ture. To evaluate the stress-sensitivity of the matrix permeability in a more realistic horizontal well with multiple fractures, I generated the meshes presented in Figure 5.16. I simulated 20 years of production from this multiply-fractured horizontal well and the pore-pressure and matrix permeability profiles are given in Figures 5.17 and 5.18, respectively. The pressure profile indicates that fracture interference begins after about three years of production. After this, the pore pressure profile continues to evolve in the Stimulate Reservoir Volume (SRV). The profiles in Figure 5.18 indicate that the matrix permeability reduces from 100 nD to 70 nD during production. This 30% reduction in permeability is dependent on the parameters used in the Gangi model, and are outlined in Table 5.1. It is worth mentioning that this 30% reduction could be significant considering that this takes place mostly near the fracture surface. A comparison of cumulative production with and without the stress-sensitive matrix permeability was presented and discussed in Figure 5.15. When the stencil shown in Figure 5.16 was simulated, and the results were multiplied by ten, the cumulative production profiles were almost identical. However, it suffices

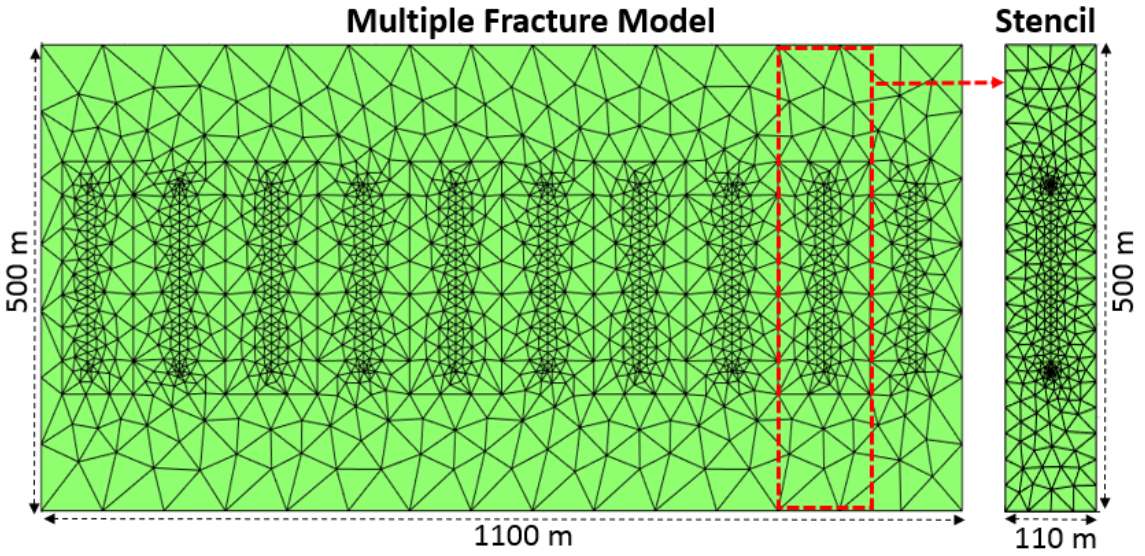

Figure 5.16: This figure shows the unstructured gridding of a horizontal well with multiple fractures using Gmsh. The physical dimension of the reservoir domain is also shown.

to mention that the use of a stencil is limited to the cases were the geometry of the problem features a repetitive fracture pattern.

5.3 Study of coupled geomechanics and transport of multi-component gas in deformable source rocks

This section focuses on the study of the production of multi-component gas from organic-rich source rocks, which are deformable. As seen in the pore-pressure profiles in the previous sections, the production of reservoir fluids typically results in sharp pressure drops near the surfaces of the hydraulic fractures. By the definition of effective stress, these sharp drops in pore-pressure could induce a corresponding increase in the effective stresses near the fracture surfaces. These induced stresses are compressive, and could lead to the elastic deformation, crushing, or embedment of the proppants in the propped hydraulic fractures. Given that the proppants can be designed to withstand crushing under the influence of the stresses in the reservoir, this work focuses on the study of the elastic

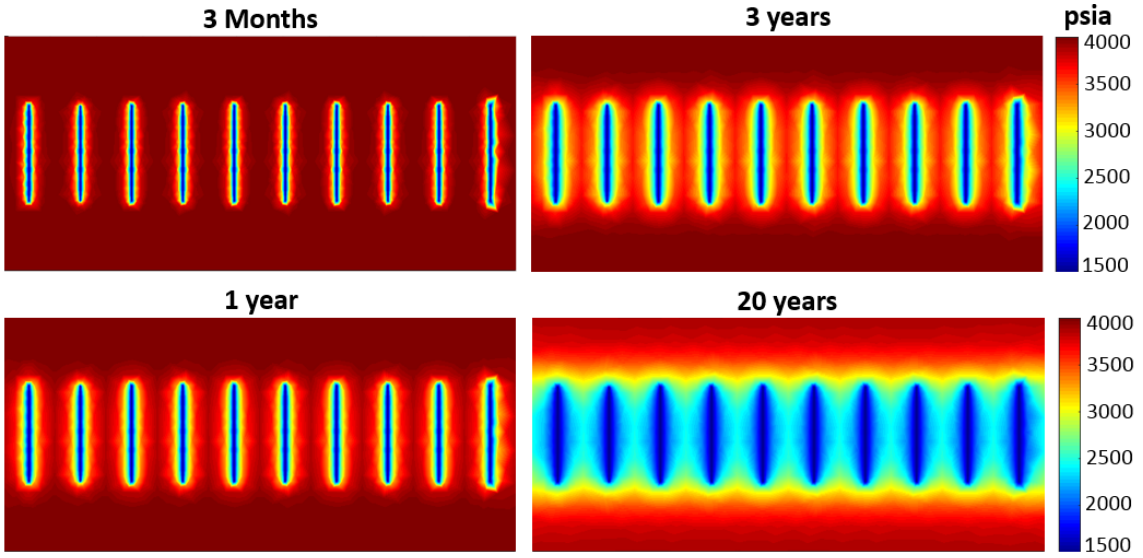

Figure 5.17: The evolution of the pore pressures with time indicates that fracture interference begins in three months. After fracture interference, the pore pressure in the stimulated area around the fractures continues to drop.

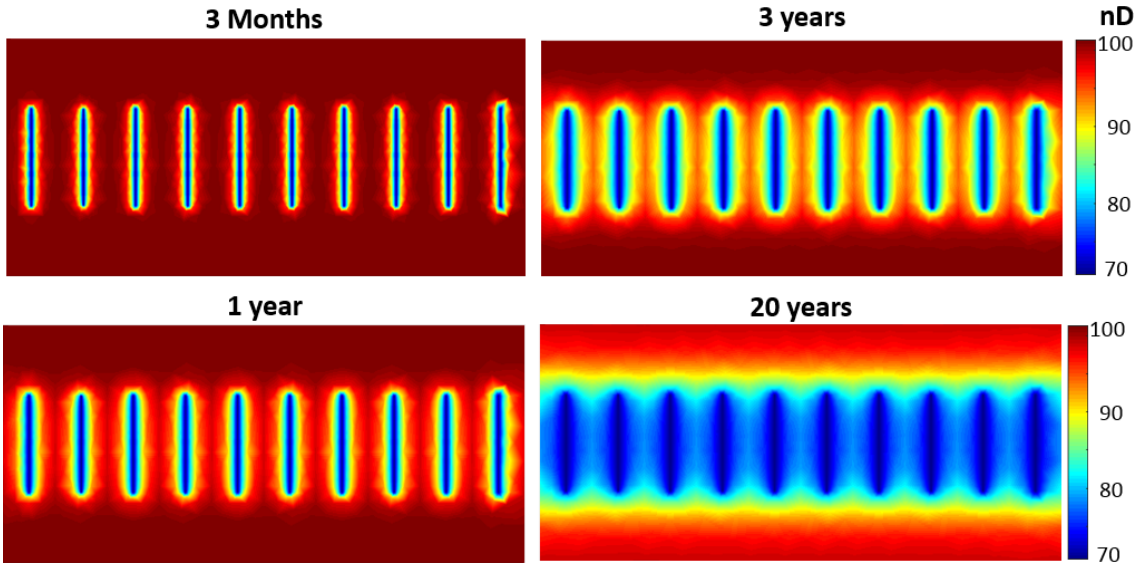

Figure 5.18: This decline in pore pressure in Figure 5.17 leads to increased effective stresses, which in turn result in a decrease in the matrix permeability. The results indicate that the matrix permeability can be reduced from an initial value of 100 nD to 70 nD.

deformation and the potential embedment of the proppants into the shale matrix. Additionally, the abundance of clay in these shales could contribute to the creep deformation or embedment of the proppants into the shale matrix.

5.3.1 Simulation results for compositional gas transport in deformable source rocks

The production well is modeled as a constant-pressure inner boundary, while the external boundaries of the reservoir are modeled as no-flow boundaries. For the geomechanics problem, all the external boundaries of the domain were set to a fixed displacement of zero in the x and y directions. Figure 5.19 shows the pressure profile in the inorganic and organic pores after 20 years of production at a flowing bottom hole pressure of 1,000 psia. The profiles show a sharp drop in pressure from the initial pressure of 4,000 psia to the flowing bottom-hole pressure in the vicinity of the fracture surfaces.

Figure 5.20 gives the profiles for the mole fractions of methane and ethane in the inorganic and organic matrices. It shows that the mole fraction of methane gradually drops during production because methane is the lightest gas component, and it tends to diffuse towards the production well faster than the other components.

Figures 5.21(a) and (b) show the changes in the horizontal and displacement displacement profiles after 20 years of production. To clarify, the initial conditions for the simulation of production corresponds to the situation in the shale matrix, after hydraulic fracturing and flow back. The actual value of the displacement profile is not expected to be zero throughout the domain, because the fracture has a finite width, and the matrix is expected to be displaced away from the fracture surface. However, to focus on the changes in displacement induced during production only, I set the initial displacement to be zero everywhere in the domain. This implies that the displacement profiles shown in Figures 5.21(a) and (b) represent the change in the displacement relative to the condition in the shale matrix prior to gas production. The horizontal displacement solution indicates that

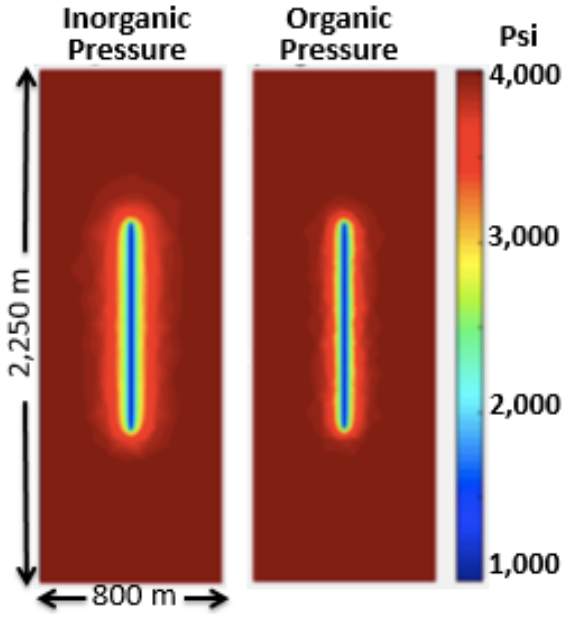

Figure 5.19: Pressure profile (in psi) after 20 years of production.

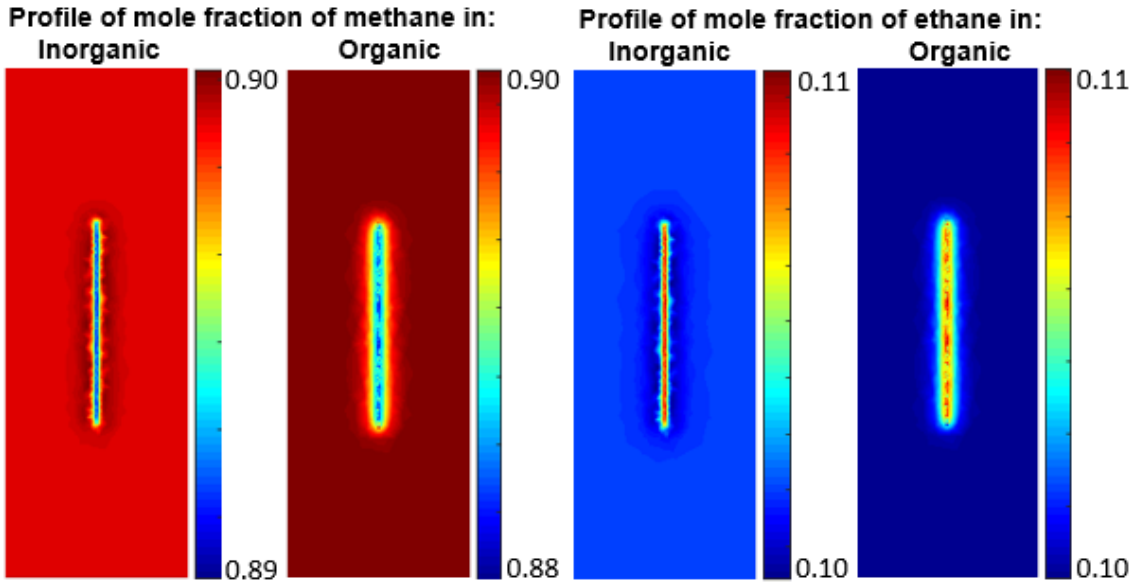

Figure 5.20: Mole-fraction of methane and ethane ($y_{Methane}$ and y_{Ethane}).

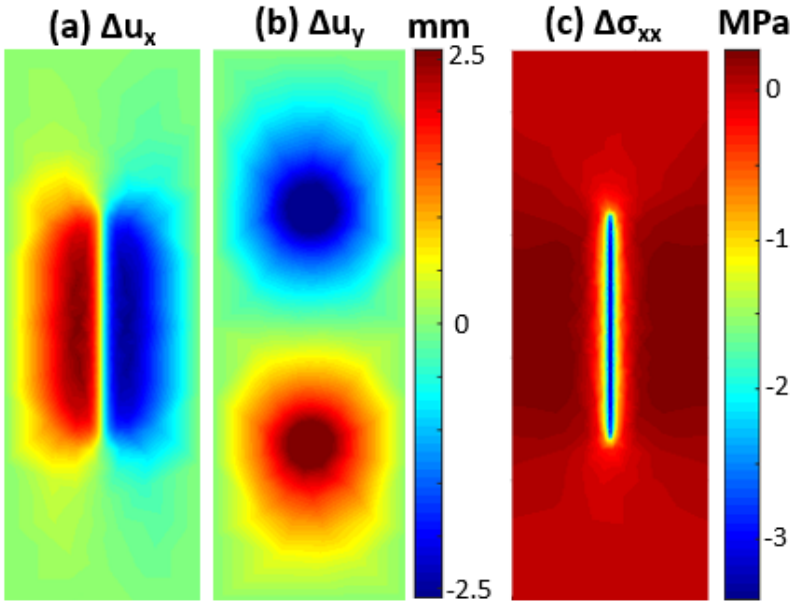

Figure 5.21: The displacement and stress profiles indicate that the fractures tend to close during production.

the simulation of production of reservoir fluids can cause the grid-blocks on the left of the fracture surface to be displaced toward the right (positive x-direction), while the grid-blocks on the right of the fracture surface can be displaced toward the left. Similarly, the vertical displacement profiles indicate that the simulation grid-blocks in the bottom half of the domain can be displaced upwards, while the grid-blocks in the upper half of the domain can be displaced downwards. This implies that the induced horizontal stresses tend to reduce the hydraulic fracture aperture, while the induced vertical stresses tend to reduce the fracture length. Additionally, the maximum upward and downward displacements are centered at the location of the fracture tips.

Figure 5.21(c) gives the profile of the change in the volumetric component of the effective stress (σ'_{xx}) acting in the x-direction after 20 years of production. This is the change in the effective closure stress (relative to the initial condition before production), which acts on the hydraulic fracture to reduce the fracture aperture and conductivity. The profile

shows that this change in closure stress is maximum around the fracture surfaces, and is induced as a result of the pore-pressure drop around the fracture surfaces, shown in Figure 5.19. The negative sign of this change in effective stress is consistent with the convention that compressive stresses are considered negative in this dissertation. Considering that the in-situ stresses in the formation prior to fracturing and production are compressive, the negative change in effective stress implies that the total compressive stresses acting on the hydraulic fracture surface will increase during production. This increased compressive stresses typically leads to proppant deformation, crushing, or embedment during production.

5.3.2 Effect of induced stresses on fracture width, conductivity and production

The change in fracture width is modeled with Guo and Liu (2012) model, as discussed in Section 3.7. The fracture conductivity is then computed as the product of the updated fracture width and fracture permeability. The fracture permeability is scaled as the square of the fracture width. The uncertainty in the creep deformation of the proppants in the hydraulic fracture is reflected in the viscoelastic shear coefficient, which could be treated as a history-matching parameter. To evaluate the impact of this parameter on the hydraulic fracture width, conductivity and production, I performed the numerical simulations at values corresponding to high, mid and low values of the viscoelastic shear coefficient. These values were taken from obtained from Huang et al. (2016).

Figure 5.22 presents the change in induced stress, normalized fracture width and conductivity with time, and shows the effect these have on the cumulative production. The fracture width and conductivity are normalized by dividing with the corresponding values before the production. The results are based on the base-case parameters shown in Tables 5.1 and 5.2. At these base-case values, the fracture conductivity is infinite, with a dimensionless fracture conductivity of about 3,300. Figure 5.22a shows that the fracture

width and conductivity decline during production, while the effective stress acting on the hydraulic fracture surface increases. The sensitivity of these changes in fracture width and conductivity to the viscoelastic shear coefficients indicates that the decline in fracture width and conductivity is more severe at lower values of the viscoelastic shear coefficient. This is expected considering that the change in fracture width is inversely proportional to the viscoelastic shear coefficient ν as given in Eq. 3.55. The high-, mid- and low-case values of the viscoelastic shear coefficient correspond to strong, medium, and weak propped hydraulic fractures. The blue curve in Figure 5.22a represents the magnitude of the change in stress acting on the hydraulic fracture surface. As discussed in the previous subsection, this magnitude of the change in the effective stress increases sharply as the pressure near the fracture surfaces drop rapidly. Only one curve is shown for the closure stress because this was basically unchanged at the different values of the viscoelastic shear coefficient.

Figure 5.22b indicates that the sensitivity of the cumulative production to the viscoelastic shear coefficient is negligible, even though there is considerable drop in fracture width and conductivity, as shown in Figure 5.22a. This is because the initial fracture conductivity is so high that the fracture still behaves as an infinite-conductivity fracture even after the fracture width and conductivity decline as shown in Figure 5.22a. To investigate this further, the simulation study was repeated but at a dimensionless fracture conductivity of 100 instead of 3,300. Figure 5.23 shows the corresponding results. Although, the decline in the fracture width and conductivity in Figure 5.23a are relatively similar in magnitude to those shown in Figure 5.22a, the impact on cumulative production in Figure 5.23b is much more severe than in Figure 5.22b. As expected, the simulation results show that the weak hydraulic fractures give the least cumulative production because they show the most decline in fracture conductivity, while the hydraulic fractures with high values of the viscoelastic coefficient show higher cumulative production because they offer more resistance to viscoelastic deformation. The significant reduction in fracture conductivity and

cumulative production shown in Figures 5.23(a) and (b) could possibly explain the sharp production decline typically observed in shale-gas reservoirs.

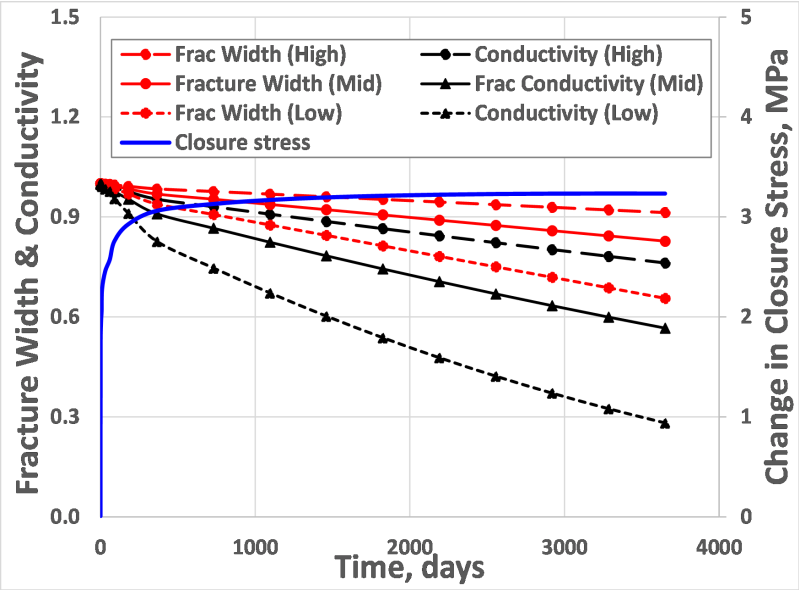

(a) Change in induced stress, normalized fracture width and conductivity with time.

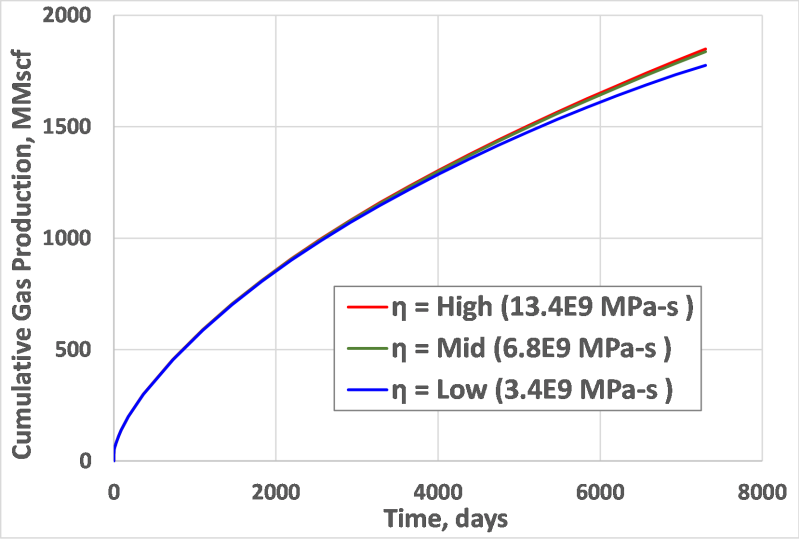

(b) Cumulative production versus time.

Figure 5.22: Results indicate that the induced effective stress increases due to pressure decline during production. This leads to a reduction in the fracture width and conductivity, which consequently results in considerable reduction in production.

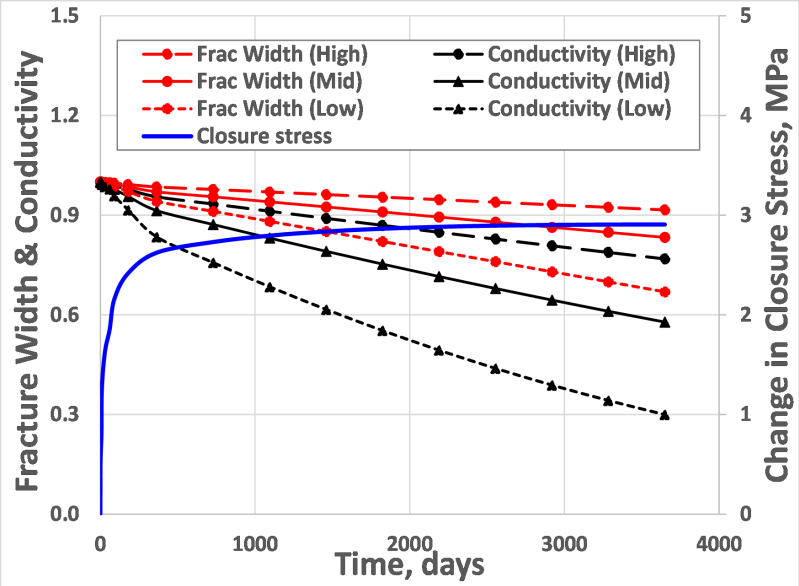

(a) Change in induced stress, normalized fracture width and conductivity with time.

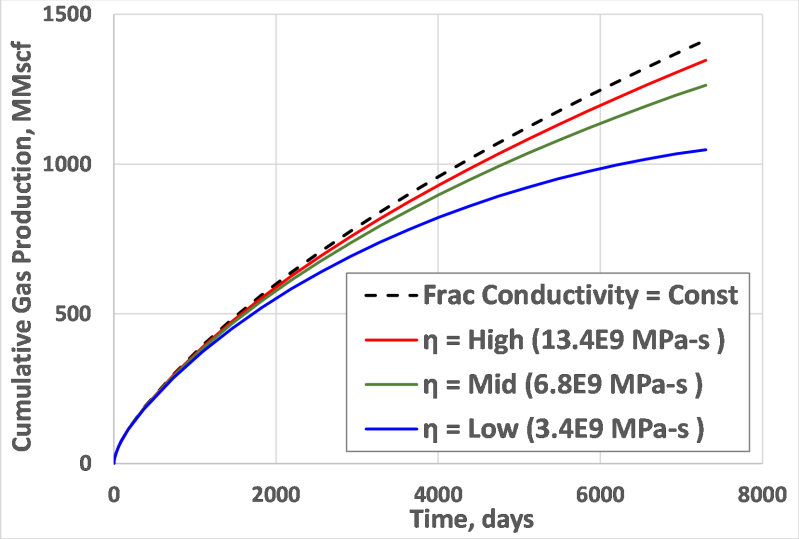

(b) Cumulative production versus time.

Figure 5.23: Results indicate that the induced effective stress increases due to pressure decline during production. This leads to a reduction in the fracture width and conductivity, which consequently results in considerable reduction in production.

Figure 5.24 indicates the decline in fracture width and conductivity as the magnitude of the effective stress change increases. The change in stress in Figure 5.24 refers to the

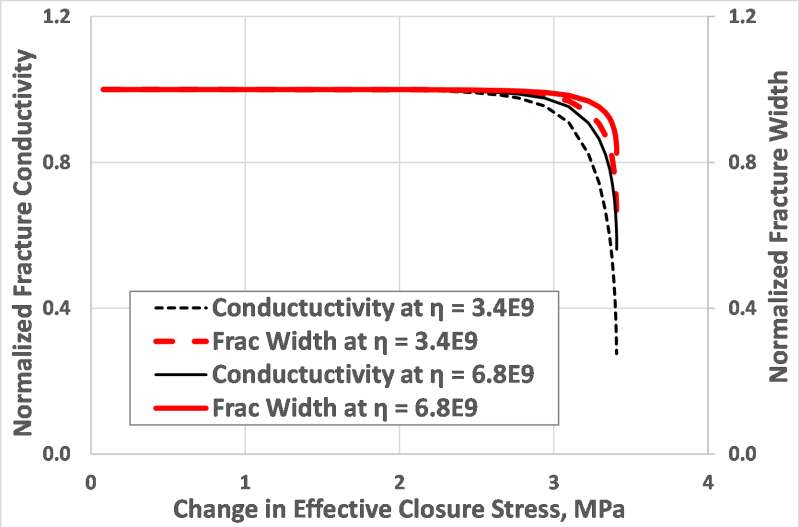

Figure 5.24: The fracture width and conductivity decline as the effective fracture closure stress increases due to pressure decline during production.

increase in the magnitude of the effective stress (in the x-direction) due to the pore-pressure depletion only, excluding the contribution of the initial effective stress before production. The dotted lines show the decline in the fracture width and conductivity at the low-case viscoelastic shear coefficient value of 3.4E9 MPa-s from Huang et al. (2016), while the solid lines represent the corresponding curves at the mid-case values. The fracture width and conductivity decline faster at lower values of this coefficient because strain is inversely proportional to the viscoelastic shear coefficient and Young's Modulus.

5.4 Evaluation of the storage of CO_2 in depleted and deformable source rocks

In this section, the objective is to evaluate the potential of injecting anthropogenic CO_2 into depleted organic-rich source rocks that are located near industrial areas. The simulation is performed in two stages, consisting of a production stage and an injection stage. The simulation results from the production stage are similar to those from the previous section, except that I simulate a four-component system here, whereas the previous sys-

tem involved only three components. The fourth component introduced here is CO_2 at a trace amount of 2% at initial conditions. Figure 5.25 gives the profile of the inorganic and organic pore pressures after 20 years of simulated production. As discussed in the previous section, sharp drops in pore pressures can be seen near the fracture surfaces.

Figure 5.26 gives the profile of the changes in the horizontal displacements, vertical displacements and induced horizontal stresses with respect to the corresponding values at initial conditions (prior to production). Figure 5.26(a) indicates that the production of reservoir fluids could lead to the displacement of the matrix grid-blocks towards the fracture surface. Similarly, Figure 5.26(b) indicates that production could lead to the displacement of the matrix grid-blocks (at the fracture tips) towards the center of the hydraulic fracture. The negative change in stresses observed in Figure 5.26(c) indicates that gas

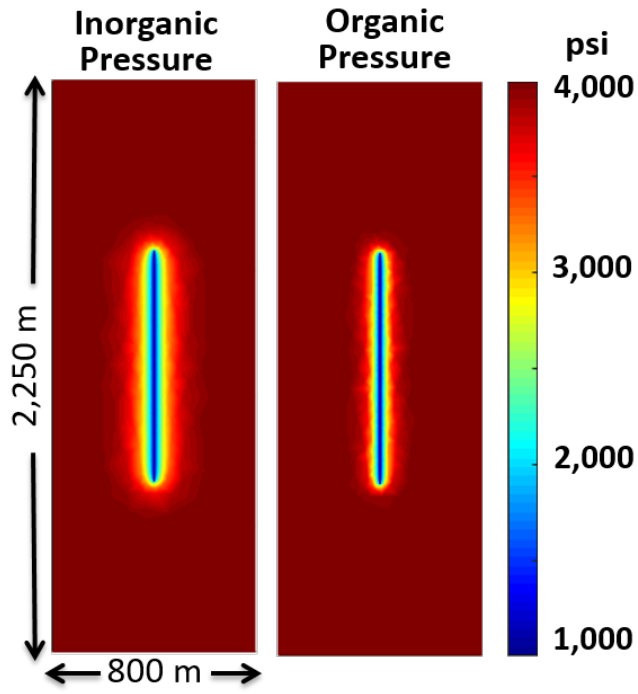

Figure 5.25: Pressure profile (in psi) after 20 years of production.

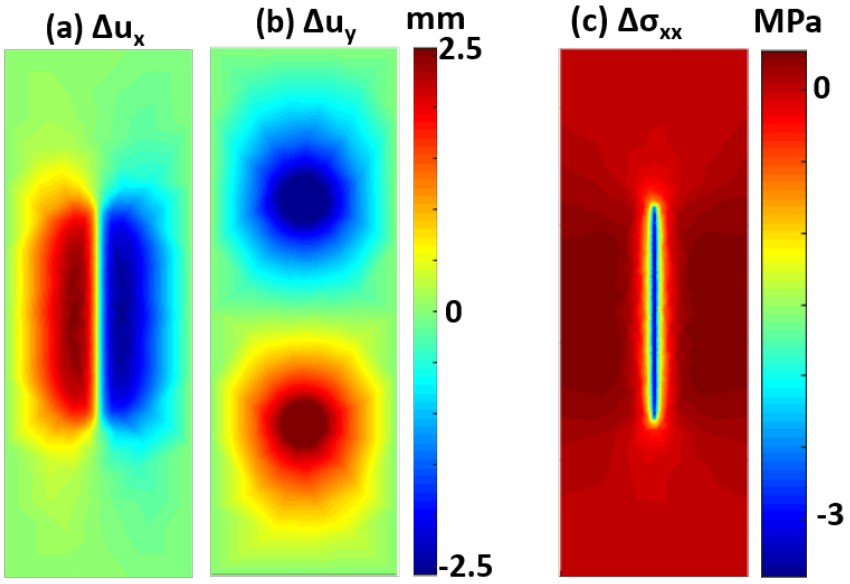

Figure 5.26: The profiles of the change in displacement and stress fields indicate that the fractures tend to close during production.

production could lead to an increase in the magnitude of the compressive stresses, because compressive stresses are considered to be negative.

Figure 5.27 gives the profiles of the methane, ethane and CO_2 compositions after 20 years of production. As in the previous section, the profile shows that the mole fraction of methane gradually drops during production because methane is the lightest gas component, and it tends to diffuse towards the production well faster than the other components. After 20 years of simulated production, CO_2 is then injected into the single vertically fractured shale-gas well at a constant injection pressure of 4,100 psia. The profile of the change in pore pressure after 10 years of injection is shown in Figure 5.28. To clarify, these changes in pore pressure are relative to the pressure profile after 20 years of simulated production. The maximum change in pore-pressure is 3,100 psia because the lowest pressure near the fracture surface was 1,000 psia after production, and the maximum pressure near the fracture surface was 4,100 psia during CO_2 injection. The sharp increase in the inorganic

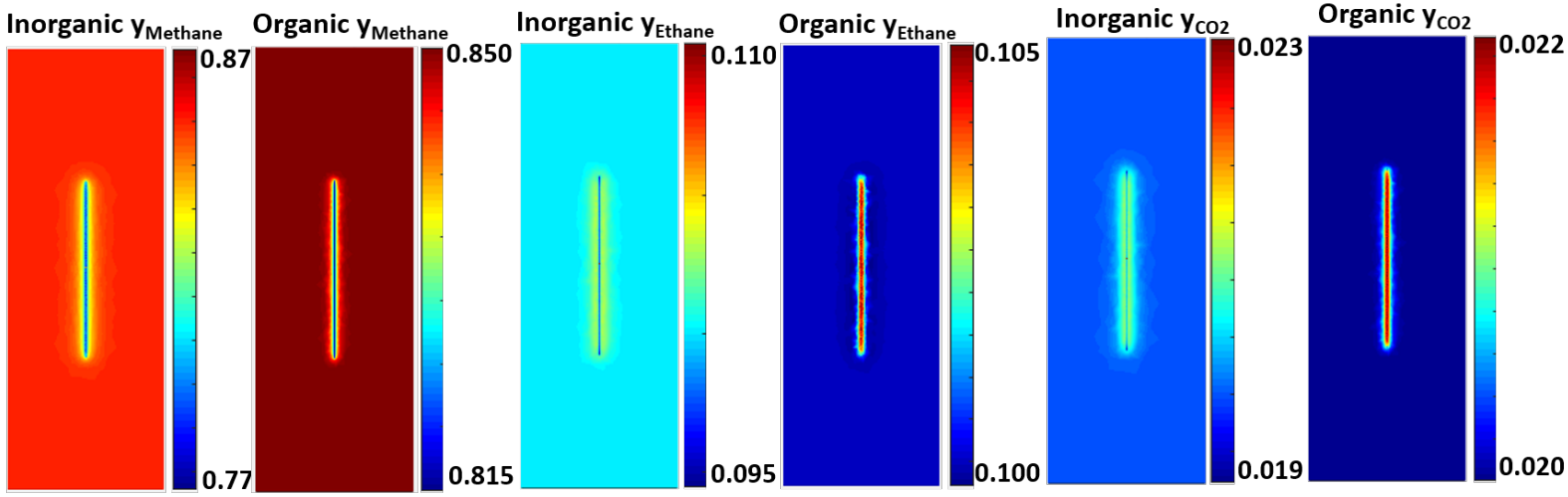

Figure 5.27: Mole-fraction of methane, ethane and CO_2 ($y_{Methane}$, y_{Ethane}, and y_{CO_2}).

pressure near the fracture surface indicates that CO_2 is injected into the formation, while the corresponding sharp increase in the organic pressure indicates that the injected fluid is able to diffuse into the organic matrix.

The change in the horizontal displacements, vertical displacements and induced horizontal stresses are shown in Figure 5.29. These changes are relative to the corresponding profiles in the reservoir after 20 years of simulated production. Figure 5.29(a) indicates that the injection of CO_2 could lead to the displacement of the matrix grid-blocks away from the fracture surface. Similarly, Figure 5.29(b) indicates that the injection of CO_2 could lead to the displacement of the matrix grid-blocks (at the fracture tips) away from fracture tips and into the matrix. The positive change in stresses observed in Figure 5.29(c) indicates that the injection of CO_2 could lead to a reduction in the magnitude of the com-

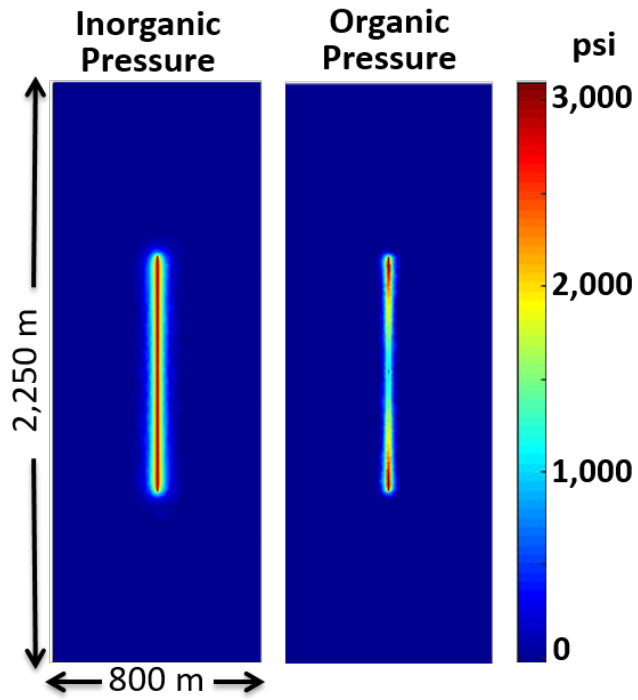

Figure 5.28: Change in the pressure profile (relative to the profile before injection) after 10 years of CO_2 injection.

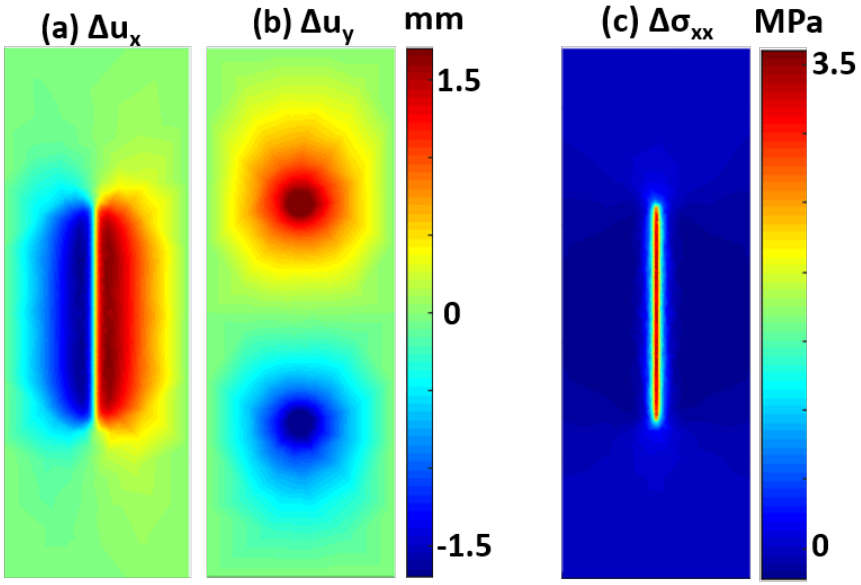

Figure 5.29: The change in displacement and stress profiles indicate that the induced stresses could reduce the magnitude of the effective compressional stresses acting on the propped hydraulic fractures during CO_2 injection.

pressive stresses, because compressive stresses are considered to be negative. Considering that the injection pressure is only 100 psi more than the initial pore-pressure, the pore-pressure is not expected to exceed the minimum horizontal stress, which is compressional. This implies that the actual value of the effective stress acting on the hydraulic fracture surface is still expected to be negative, implying that the fracture width and length do not increase. Additionally, the injected CO_2 is expected to remain within the Stimulated Reservoir Volume (SRV) that was created during hydraulic fracturing, since the injection pressure is less than the minimum horizontal stress in the reservoir.

It is important to emphasize that the changes in the displacement and stress profiles, are relative to the displacement and stress fields after 20 years of production. So, the actual value of the displacement field during CO_2 injection will incorporate the initial displacement field before fracturing, as well as the displacements induced during hydraulic

fracturing, production and injection. Similarly, the actual effective stress that acts on the hydraulic fracture surface during CO_2 injection will include the effect of the initial stress distribution before production, the stresses induced during production, as well as the stresses induced during CO_2 injection. Injecting CO_2 at pressures greater than the sum of the minimum horizontal stresses and the strength of the rock could lead to re-fracturing, and an increase in the fracture width and length. This will require the modeling of hydraulic fracture propagation, and is beyond the scope of this dissertation.

Figure 5.30 gives the profiles of the methane, ethane and CO_2 compositions after 10 years of CO_2 injection. The profile shows an increase in the mole fraction of CO_2 in the organic matrix, which indicates that the injected CO_2 can diffuse into the organic matrix, and could be trapped by adsorption near the large internal organic surfaces. Figure 5.31 shows the injection rates and cumulative injection of CO_2 into the depleted organic-rich source rock modeled. The green, red and blue lines correspond to the cases where the bottomhole pressure was fixed at 5000, 4500 and 4100 psia, respectively. The dotted black line corresponds to a case where the bottomhole pressure was fixed at 4,100 psia, but the organic matrix was artificially removed from the model. The cumulative injection curves indicate that a large amount of CO_2 is injected at very early times, after which the rate of injection of CO_2 slows down remarkably. The large volumes injected at very early times could be explained by the expected rapid injection rates into the depleted hydraulic fractures. The very low pressures around the well and hydraulic fractures (about 1,000 psia as shown in Figure 5.25) imply that the change in pressure during injection will be 4000, 3500 and 3100 psia, when the bottomhole pressure is fixed at 5000, 4500 and 4100 psia, respectively. These large changes in pressure when multiplied with the injectivity yield high injection rates. However, with continued CO_2 injection, the pressure around the well and hydraulic fractures builds up very quickly, leading to sharp drops in the change in pressure, and a consequent drop in the injection rates. Figure 5.32 presents the amount

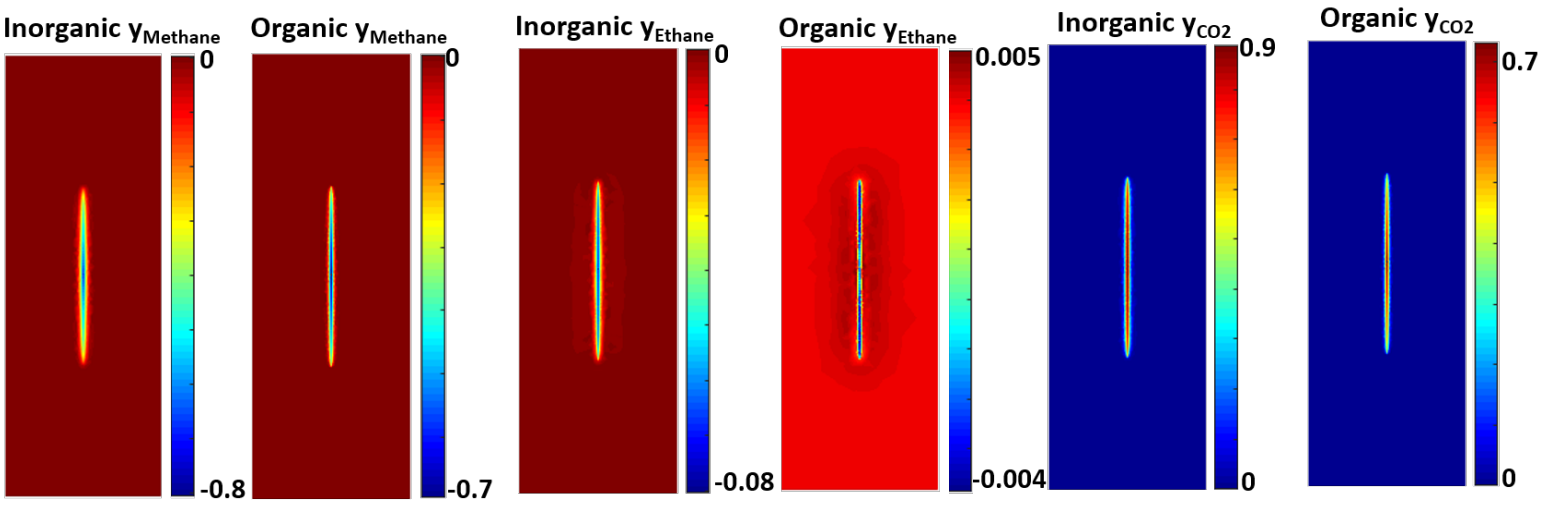

Figure 5.30: Change in the mole-fraction of methane and ethane ($y_{Methane}$, y_{Ethane} and y_{CO2}) after 10 years of CO_2 injection.

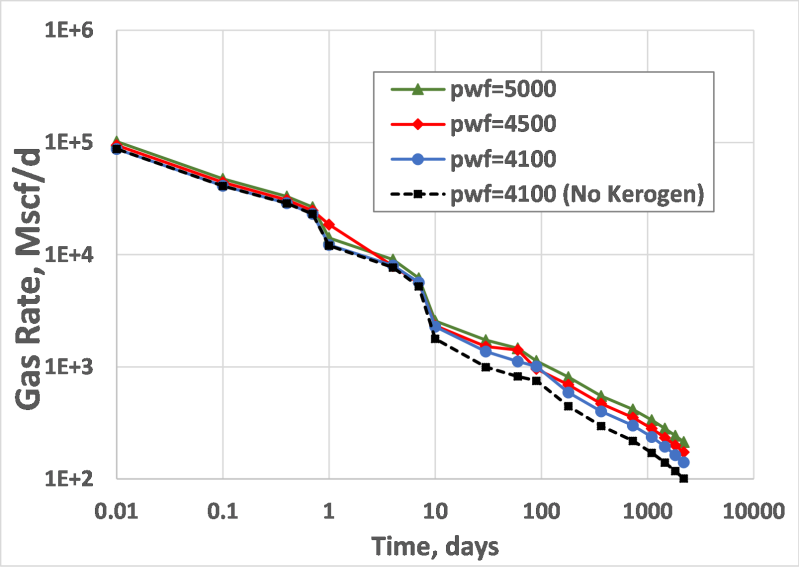

(a) CO_2 Injection Rate Plots.

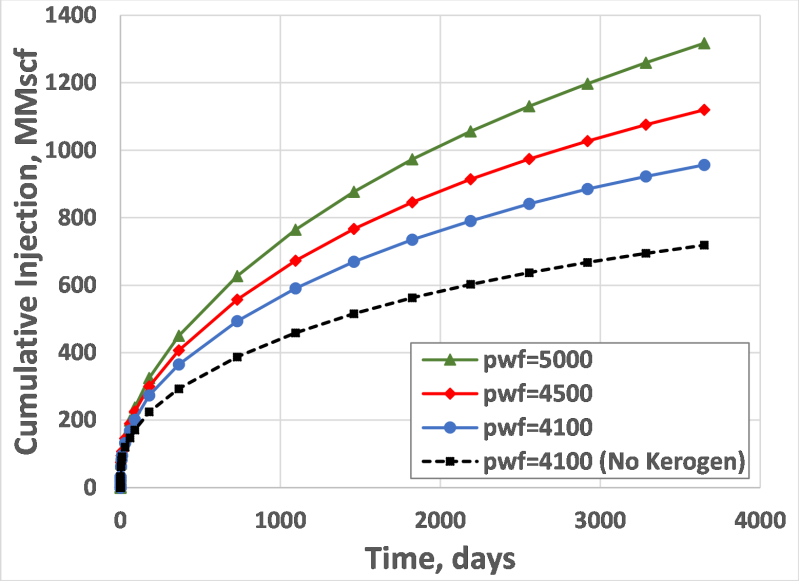

(b) Cumulative CO_2 Injection Plots.

Figure 5.31: Comparison of the injection plots at different bottomhole pressures indicates the amount of CO_2 injected into the depleted shale matrix at these different pressures.

of CO_2 injected in 10 years as a fraction (in percentage) of the amount of gas produced in 20 years. The respective percentages for the four cases shown in Figure 5.31 are given on a yearly basis. The results show that the amount of CO_2 injected within a 10-year period could be significant in comparison to the amount of gas produced over a 20-year period. This suggests that CO_2 injectivity into a depleted shale formation could be comparable to the productivity of gas from the same shale formation.

To access the potential of the organic matrix to trap some of the injected CO_2, I show a plot of the percentage of the injected CO_2 that gets sorbed into the organic matrix (in Figure 5.33). The result shows that about 25% of the total amount of CO_2 injected (in a 10-year time frame) is stored in the sorbed state within the organic matrix. This indicates that the organic matrix could potentially serve as a trapping mechanism for some of the CO_2 that is injected during CO_2 sequestration in depleted organic-rich source rocks.

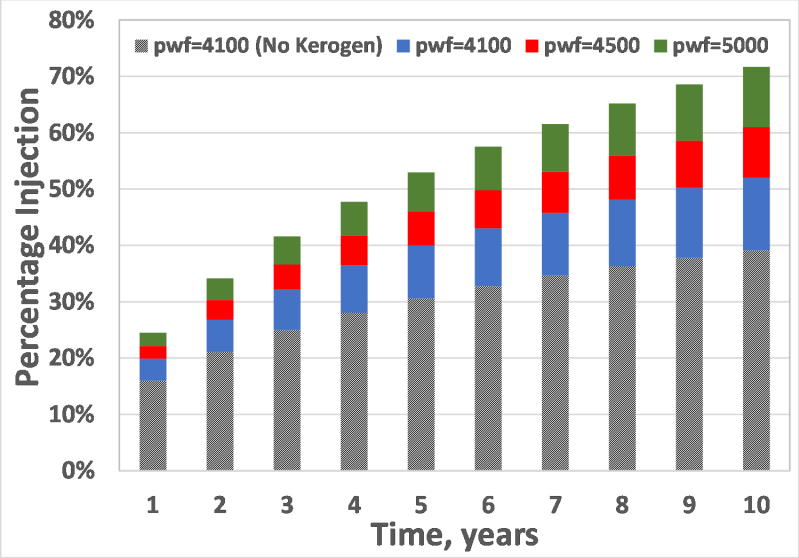

Figure 5.32: Percentage of CO_2 injected in 10 years. The results indicate that the amount of CO_2 injected could be significant in comparison to the amount of gas that was produced over 20 years. This indicates that the CO_2 injectivity into a depleted organic-rich source rock could be significant in comparison to the gas productivity from the same source rock.

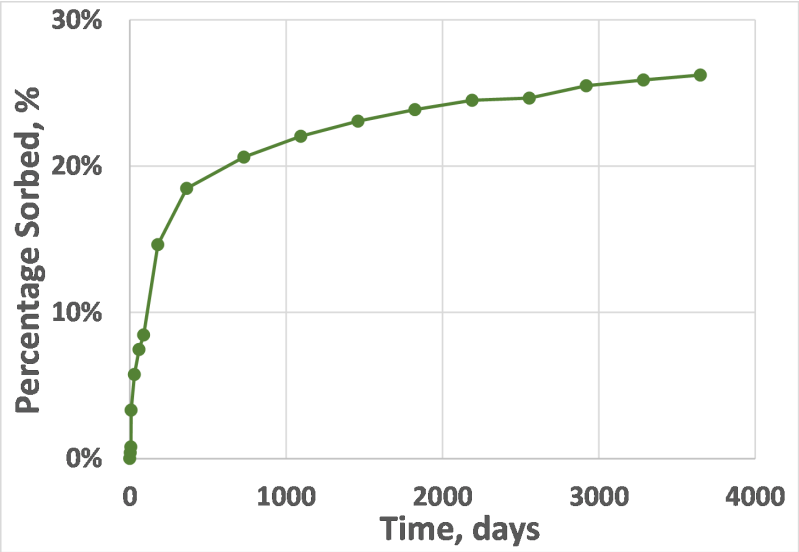

Figure 5.33: Plot of the fraction of injected CO_2 that gets sorbed into the organic matrix. The results indicate that about 25% of the total amount of injected CO_2 gets sorbed into the organic matrix over a 10-year time frame. This indicates that the kerogen in depleted organic-rich source rocks could potentially provide a trapping mechanism for the injected CO_2.

6. SUMMARY AND CONCLUSIONS

6.1 Summary

This work presents a mathematical model and simulator for the transport of multi-component gas in a deformable organic-rich source rock. The coupled partial differential equations presented in this work were discretized using the control volume finite element method, and the fractures in the reservoir domain were modeled using the discrete fracture model. The new contributions provided in this work includes:

1. To develop a mathematical model for the transport of multi-component gas in a shale matrix, consisting of the organic and inorganic matrices. Unlike previous models for transport in shales, this work models the organic matrix (or kerogen) as a dispersed and discontinuous continuum. The rationale behind this dispersed kerogen model is inferred from SEM images, as well as the experimental and history-matching work by Kang et al. (2011), which indicates that kerogen appears to be discontinuous at scales larger than tens of microns, and that the coupling between the organic and inorganic matrices is in series.

2. To present a Maxwell-Stefan formulation for the computation of the pressure- and composition-dependent diffusion coefficients in a multi-component system with more than two components.

3. To develop and implement a time-dependent shape factor to be used in the coupling term that describes the series transport of the multi-component shale gas from the kerogen into the inorganic matrix. This time-dependence of the coupling term was developed based on the time-dependent shape factor presented by (Zimmerman et al., 1993) for a dual-porosity matrix/fracture system. In this work, I focus on a

dual-continuum matrix comprising of the inorganic and organic matrices.

4. To implement a modified form of the petrophysical model proposed by Ambrose et al. (2012) and Hartman et al. (2012). The petrophysical model from Ambrose et al. (2012) and Hartman et al. (2012) basically reduces the pore volume available for the storage of free gas in the shale matrix by the pore volume occupied by the adsorbed gas molecules. The modification made to be made in this work is to correct only the organic pore volume (and not the total pore volume) by the volume occupied by the adsorbed gas molecules because I do not expect any significant adsorption in the inorganic pores.

5. To develop a fully-coupled model for the transport of multi-component gas in a deformable shale matrix. The stress-dependence of the matrix permeability will be modeled using the Gangi's model (Gangi, 1978), while the stress and time-dependence of the propped fracture conductivity will be modeled using an analytical viscoelastic model presented by Guo and Liu (2012).

6. To evaluate the potential of injecting and storing anthropogenic CO_2 in depleted organic-rich source rocks, using the numerical simulator developed.

6.2 Conclusions

This work presents a multiple-continuum model for multi-component gas transport in organic-rich source rocks with a deformable matrix. The model presented captures the dispersed nature of kerogen observed in SEM images, and the consequent series coupling between the organic and inorganic pores. To account for the pressure and composition dependence of molecular diffusion in the nanoporous matrix, I used the multi-component Maxwell-Stefan diffusion formulation. The model accounts for the elastic and creep deformation of the shale formation and its interaction with a propped hydraulic fracture. I

model the free-gas pore-volume increase due to desorption coupled with the pore-volume reduction due to the mechanical deformation of the shale matrix. All the poroelasticity equations were discretized using the CVFEM. A simplified version of the simulator built as part of this work was validated against Eclipse 300 for a multi-component system, without organic pores. I validated the coupled geomechanical and flow simulator by comparing with the analytical solution of the Terzaghi problem.

The numerical studies performed in this work indicates that advective transport dominates diffusive transport in the inorganic pores of the representative Barnett shale-gas reservoir simulated. However, at lower values of permeability (10 nD and lower), the contribution of molecular diffusion to the total transport becomes increasingly significant. This coupled with the expected lack of cracks and large macropores in kerogen suggests that advective transport could be negligible in the organic pores, and the predominant transport mechanism could be diffusive (free-gas and adsorbed gas diffusion). Considering that most commercially-viable unconventional resources are expected to have over 10 nD of matrix permeability, the contribution of molecular diffusion to the transport in these organic-rich source rocks is expected to be negligible. This work argues that it could be crucial to model the organic and inorganic continua separately, given the expected physical differences in the transport mechanisms that prevail in these two continua, and the dispersed nature of kerogen.

The results of this work shows the importance of correcting the free-gas pore volume for the pore volume occupied by the gas molecules adsorbed on the organic pore walls. The comparison of a shale-gas simulation model to a similar model with all the organic pores replaced by inorganic pores indicates that although organic pores could contribute significantly towards the total storage in resource shales, the contribution of these organic pores to the cumulative gas production (during the typical production life of these unconventional resources) could be severely curtailed by the generally lower recoveries

associated with desorption at relatively high average reservoir pressures, as well as the degree of coupling between the organic and inorganic pores. This further supports the argument that the micro-scale nature of resource shales could be important and should not be ignored because this could result in an overestimation of the contribution of the discontinuous organic matter. The sensitivity studies on the degree of coupling between the organic and inorganic pores indicates that the contribution of the organic pores to total production peaks off at a particular value of the coupling constant. The study of the effect of the stress-dependence of matrix permeability indicates that the cumulative production could be reduced significantly because of the reduction in permeability as the pore pressure decreases during production.

The studies of coupled geomechanics and compositional gas simulation in this work indicate that the production of fluids from fractured shale-gas reservoirs could result in compressive stresses that could lead to the closing of the hydraulic fractures. This could in turn lead to considerable decline in production. The simulator developed in this work was used to evaluate the potential injection and storage of anthropogenic CO_2 in depleted resource shales. The results indicate that the effective stress induced during production and subsequent injection of CO_2 will depend on the magnitudes of initial stresses in the shale formation prior to fracturing, the stresses induced during hydraulic fracturing, the compressive stresses induced during production, as well as the tensile stresses that could be induced if CO_2 is injected at pressures higher than the in situ stresses. Additionally, the studies performed in this work indicate that CO_2 could be potentially injected and stored in depleted organic-rich source rocks.

6.3 Recommendations for Further Work

This work focused on the development of mathematical models that describe important mechanisms of storage and transport in organic-rich shale gas reservoirs. A 2D coupled

geomechanics and flow simulator was developed based on the assumption of linear elasticity. I would strongly recommend the extension of this model to three dimensions, with a transversely isotropic shale matrix and a plasticity model for the deformation of the matrix. Other further extensions of this model could include the extension to multiple phases and the incorporation of multiphase flash with confinement effects. For improved computational efficiency, the code developed could be parallelized to take advantage of parallel computing on multicore, and other parallel computers.

REFERENCES

I. Y. Akkutlu, Yalchin Efendiev, and Maria Vasilyeva. Multiscale model reduction for shale gas transport in fractured media. *Computational Geosciences*, pages 1–21, 2016. doi: 10.1007/s10596-016-9571-6.

I. Yucel Akkutlu and Ebrahim Fathi. Multiscale gas transport in shales with local kerogen heterogeneities. 2012. doi: 10.2118/146422-PA.

Masoud Alfi, Bicheng Yan, Yang Cao, Cheng An, John E. Killough, and Maria A. Barrufet. Microscale porosity models as powerful tools to analyze hydrocarbon production mechanisms in liquid shale. *Journal of Natural Gas Science and Engineering*, 26:1495 – 1505, 2015. ISSN 1875-5100. doi: http://doi.org/10.1016/j.jngse.2015.08.002.

Raymond J. Ambrose. Micro-structure of gas shales and its effects on gas storage and production performance. *ProQuest Dissertations and Theses*, page 179, 2011.

Raymond J. Ambrose, Robert C. Hartman, Mery Diaz-Campos, I. Yucel Akkutlu, and Carl H. Sondergeld. Shale gas-in-place calculations part i: New pore-scale considerations. *SPE Journal*, 2012. doi: 10.2118/131772-PA.

Prince Nnamdi Azom and Farzam Javadpour. Dual-continuum modeling of shale and tight gas reservoirs. 2012. doi: 10.2118/159584-MS.

Mao Bai, Derek Elsworth, and Jean-Claude Roegiers. Multiporosity/multipermeability approach to the simulation of naturally fractured reservoirs. *Water Resources Research*, 29(6):1621–1633, 1993. doi: 10.1029/92WR02746. URL `http://dx.doi.org/10.1029/92WR02746`.

Hui Cao. Development of techniques for general purpose simulators. 2002. URL https://pangea.stanford.edu/ERE/pdf/pereports/PhD/Cao02.pdf.

H. Chen and L. W. Teufel. Coupling fluid-flow and geomechanics in dual-porosity modeling of naturally fractured reservoirs. 1997.

H. Chen and L. W. Teufel. Coupling fluid-flow and geomechanics in dual-porosity modeling of naturally fractured reservoirs - model description and comparison. 2000.

Z. Chen, G. Huan, and Y. Ma. *Computational Methods for Multiphase Flows in Porous Media*. Society for Industrial and Applied Mathematics, 2016/08/10 2006. ISBN 978-0-89871-606-1. doi: doi:10.1137/1.9780898718942.

J. Cordazzo, F. S. V. Hurtado, C. R. Maliska, and A. F. C. da Silva. Numerical techniques for solving partial differential equations in heterogeneous media. *XXIV Iberian Latin-American Congress on Computational Methods in Engineering*, 2003.

J. Cordazzo, C. Maliska, A. F. C. da Silva, and F. S. V. Hurtado. An element based conservative scheme using unstructured grids for reservoir simulation. *WPC*, 2005.

R. P. Danner and T. E. Daubert. *Manual for predicting chemical process design data : data prediction manual*. New York, N.Y. : American Institute of Chemical Engineers, 1983. ISBN 0816903298 (ch. 5).

James O. Duguid and P. C. Y. Lee. Flow in fractured porous media. *Water Resources Research*, 13(3):558–566, 1977. doi: 10.1029/WR013i003p00558. URL http://dx.doi.org/10.1029/WR013i003p00558.

Y. Efendiev, S. Lee, G. Li, J. Yao, and N. Zhang. Hierarchical multiscale modeling for

flows in fractured media using generalized multiscale finite element method. 2015. doi: 10.1007/s13137-015-0075-7.

Robert Eymard and Fernand Sonier. Mathematical and numerical properties of control-volumel finite-element scheme for reservoir simulation. *SPE Journal*, 1994. doi: 10.2118/25267-PA.

Ebrahim Fathi and I. Yucel Akkutlu. Multi-component gas transport and adsorption effects during co2 injection and enhanced shale gas recovery. *International Journal of Coal Geology*, 123:52 – 61, 2014. ISSN 0166-5162. doi: http://dx.doi.org/10.1016/j.coal.2013.07.021.

Peter A. Forsyth. A control-volume, finite-element method for local mesh refinement in thermal reservoir simulation. *SPE Reservoir Engineering*, 1990. doi: 10.2118/18415-PA.

Craig Freeman, George J. Moridis, Dilhan Ilk, and Tom Blasingame. A numerical study of transport and storage effects for tight gas and shale gas reservoir systems. 2010. doi: 10.2118/131583-MS. URL `https://doi.org/10.2118/131583-MS`.

Craig Freeman, George J. Moridis, Gerard Eric Michael, and Thomas Alwin Blasingame. Measurement, modeling, and diagnostics of flowing gas composition changes in shale gas wells. 2012. doi: 10.2118/153391-MS.

Edward N. Fuller, Paul D. Schettler, and J. Calvin. Giddings. New method for prediction of binary gas-phase diffusion coefficients. *Industrial & Engineering Chemistry*, 58(5): 18–27, 1966. doi: 10.1021/ie50677a007.

Edward N. Fuller, Keith Ensley, and J. Calvin Giddings. Diffusion of halogenated hydro-

carbons in helium. the effect of structure on collision cross sections. *The Journal of Physical Chemistry*, 73(11):3679–3685, 1969. doi: 10.1021/j100845a020.

L. S. K. Fung. A coupled geomechanic-multiphase flow model for analysis of in situ recovery in cohesionless oil sands. *The Journal of Canadian Petroleum Technology*, 1992. doi: 10.2118/92-06-06.

L. S. K. Fung, A. D. Hiebert, and L. X. Nghiem. Reservoir simulation with a control-volume finite-element method. *SPE Reservoir Engineering*, 1992. doi: 10.2118/21224-PA.

Anthony F. Gangi. Variation of whole and fractured porous rock permeability with confining pressure. *International Journal of Rock Mechanics and Mining Sciences & Geomechanics Abstracts*, 15(5):249–257, 1978. doi: http://dx.doi.org/10.1016/0148-9062(78)90957-9.

C. Geuzaine and J. F. Remacle. Gmsh: a three-dimensional finite element mesh generator with built-in pre- and post-processing facilities. *International Journal for Numerical Methods in Engineering*, 2009.

J. Guo and Y. Liu. Modeling of proppant embedment: Elastic deformation and creep deformation. 2012. doi: 10.2118/157449-MS.

Robert Chad Hartman, Raymond Joseph Ambrose, I. Yucel Akkutlu, and C. R. Clarkson. Shale gas-in-place calculations part ii - multicomponent gas adsorption effects. *SPE Journal*, 2012. doi: 10.2118/144097-MS.

Zoltán E. Heinemann and Georg M. Mittermeir. Derivation of the kazemi–gilman–elsharkawy generalized dual porosity shape factor. *Transport in Porous Media*, 91(1): 123–132, 2012. ISSN 1573-1634. doi: 10.1007/s11242-011-9836-4.

Hussein Hoteit. Proper modeling of diffusion in fractured reservoirs. 2011. doi: 10.2118/141937-MS.

Hussein Hoteit and Abbas Firoozabadi. Numerical modeling of diffusion in fractured media for gas-injection and -recycling schemes. *SPE Journal*, 2009. doi: 10.2118/103292-PA.

Qin-Hong Hu, Xian-Guo Liu, Zhi-Ye Gao, Shu-Gen Liu, Wen Zhou, and Wen-Xuan Hu. Pore structure and tracer migration behavior of typical american and chinese shales. *Petroleum Science*, 12(4):651–663, 2015. ISSN 1995-8226. doi: 10.1007/s12182-015-0051-8.

Jixiang Huang, Changdong Yang, Xu Xue, and Akhil Datta-Gupta. Simulation of coupled fracture propagation and well performance under different refracturing designs in shale reservoirs. 2016. doi: 10.2118/180238-MS.

F. S. V. Hurtado, C. R. Maliska, A. F. C. da Silva, and J. Cordazzo. A quadrilateral element-based finite-volume formulation for the simulation of complex reservoirs. 2007. doi: 10.2118/107444-MS.

P.S. Huyakorn and G.F. Pinder. *Computational methods in subsurface flow*. Monograph Series. Academic Press, 1983. URL `https://books.google.com/books?id=5-JRAAAAMAAJ`.

Seung Mo Kang, Ebrahim Fathi, Ray J. Ambrose, I. Yucel Akkutlu, and Richard F. Sigal. Carbon dioxide storage capacity of organic-rich shales. *SPE Journal*, 2011. doi: 10.2118/134583-PA.

Hossein Kazemi, J. R. Gilman, and A. M. Elsharkawy. Analytical and numerical solution of oil recovery from fractured reservoirs with empirical transfer functions (in-

cludes associated papers 25528 and 25818). *SPE Reservoir Engineering*, 1992. doi: 10.2118/19849-PA.

Jong-Gyun Kim and Milind D. Deo. Finite element, discrete-fracture model for multiphase flow in porous media. *AIChE Journal*, 46(6):1120–1130, 2000. doi: 10.1002/aic.690460604.

Anthony L. Lee, Mario H. Gonzalez, and Bertram E. Eakin. The viscosity of natural gases. *Industrial Engineering Chemistry Fundamentals*, 1966. doi: 10.2118/1340-PA.

Patrick A. Lemonnier. Improvement of reservoir simulation by a triangular discontinuous finite element method. 1979. doi: 10.2118/8249-MS.

R. W. Lewis and B. A. Schrefler. The finite element method in the static and dynamic deformation and consolidation of porous media. *Communications in Numerical Methods in Engineering*, 16(5):377–377, 1998. ISSN 1099-0887.

Liyong Li and Seong H. Lee. Efficient field-scale simulation of black oil in a naturally fractured reservoir through discrete fracture networks and homogenized media. *SPE Reservoir Evaluation & Engineering*, 2008. doi: 10.2118/103901-PA.

Robert G. Loucks, Robert M. Reed, Stephen C. Ruppel, and Daniel M. Jarvie. Morphology, genesis, and distribution of nanometer-scale pores in siliceous mudstones of the mississippian barnett shale. *Journal of Sedimentary Research*, 79(12):848, 11 2009.

Robert G. Loucks, Robert M. Reed, Stephen C. Ruppel, and Ursula Hammes. Spectrum of pore types and networks in mudrocks and a descriptive classification for matrix-related mudrock pores. *AAPG Bulletin*, 96(6):1071, 06 2012.

Huiyun Lu, Ginevra Di Donato, and Martin J. Blunt. General transfer functions for multiphase flow in fractured reservoirs. *SPE Journal*, 2008. doi: 10.2118/102542-PA.

J. E. P. Monteagudo and A. Firoozabadi. Control-volume method for numerical simulation of two-phase immiscible flow in two- and three-dimensional discrete-fractured media. *Water Resources Research*, 40(7), 2004. ISSN 1944-7973. doi: 10.1029/2003WR002996. W07405.

George J. Moridis, Thomas Alwin Blasingame, and Craig Freeman. Analysis of mechanisms of flow in fractured tight-gas and shale-gas reservoirs. 2010. doi: 10.2118/139250-MS.

Jahan Noorishad and Mohsen Mehran. An upstream finite element method for solution of transient transport equation in fractured porous media. *Water Resources Research*, 18 (3):588–596, 1982. doi: 10.1029/WR018i003p00588.

O. M. Olorode, C. M. Freeman, G. J. Moridis, and T. A. Blasingame. High-resolution numerical modeling of complex and irregular fracture patterns in shale-gas reservoirs and tight gas reservoirs. *SPE Reservoir Evaluation & Engineering*, 16(04):443–455, 2013.

O. M. Olorode, I. Y. Akkutlu, and Y. Efendiev. Compositional reservoir flow simulation for organic-rich gas shale. *SPE Journal*, 2017a. doi: 10.2118/182667-PA.

O. M. Olorode, I. Y. Akkutlu, and Y. Efendiev. *Modeling of Compositional Gas Transport in Shale as a Deformable Porous Medium*, pages 1984–1991. 2017b. doi: 10.1061/9780784480779.246. URL http://ascelibrary.org/doi/abs/10.1061/9780784480779.246.

O. M. Olorode, I. Y. Akkutlu, and Y. Efendiev. A compositional model for co2 storage in deformable organic-rich shales. 2017c. doi: 10.2118/185792-MS. URL https://doi.org/10.2118/185792-MS.

Abdollah Orangi, Narayana Rao Nagarajan, Mehdi Matt Honarpour, and Jacob J. Rosenzweig. Unconventional shale oil and gas-condensate reservoir production, impact of rock, fluid, and hydraulic fractures. 2011. doi: 10.2118/140536-MS.

Ding-Yu Peng and Donald B. Robinson. A new two-constant equation of state. *Industrial & Engineering Chemistry Fundamentals*, 15(1):59–64, 1976. doi: 10.1021/i160057a011.

R.C. Reid, J.M. Prausnitz, and B.E. Poling. *The Properties of Gases and Liquids*. Chemical engineering series. McGraw-Hill, 1987. ISBN 9780070517998.

Hao Sun, Adwait Chawathe, Hussein Hoteit, Xundan Shi, and Lin Li. Understanding shale gas flow behavior using numerical simulation. *SPE Journal*, 2015. doi: 10.2118/167753-PA.

Zuher Syihab. Simulation of discrete fracture network using flexible voronoi gridding. 2009. URL `http://hdl.handle.net/1969.1/ETD-TAMU-2009-12-7592`.

R. Taylor and R. Krishna. *Multicomponent mass transfer*. New York, NY (United States); John Wiley and Sons, Inc., Jan 1993.

Karl Terzaghi. *Theoretical Soil Mechanics*. Wiley, 1943. ISBN 0471853054.

S. Valliappan and N. Khalili-Naghadeh. Flow through fissured porous media with deformable matrix. *International Journal for Numerical Methods in Engineering*, 29(5):1079–1094, 1990. doi: 10.1002/nme.1620290512. URL `http://dx.doi.org/10.1002/nme.1620290512`.

A. Verruijt. *Theory and Problems of Poroelasticity*. 2016. URL `http://geo.verruijt.net`.

Vaughan R. Voller. *Basic Control Volume Finite Element Methods for Fluids and Solids*, volume 1 of *IISc Research Monographs Series*. World Scientific, 2009. ISBN 978-981-283-498-0. doi: 10.1142/7027.

Stanley M. Walas. Phase equilibria in chemical engineering. In Stanley M. Walas, editor, *Phase Equilibria in Chemical Engineering*. Butterworth-Heinemann, 1985. ISBN 978-0-409-95162-2. doi: http://dx.doi.org/10.1016/B978-0-409-95162-2.50009-9.

J. Wan. *Stabilized Finite Element Methods for Coupled Geomechanics and Multiphase Flow*. Stanford University, 2002. URL `https://books.google.com/books?id=29cJHQAACAAJ`.

J. E. Warren and P. J. Root. The behavior of naturally fractured reservoirs. *SPE Journal*, 1963. doi: 10.2118/426-PA.

Asana Wasaki and I. Yucel Akkutlu. Permeability of organic-rich shale. *SPE Journal*, 2015. doi: 10.2118/170830-PA.

R. K. Wilson and Elias C. Aifantis. On the theory of consolidation with double porosity. *International Journal of Engineering Science*, 20(9):1009–1035, 1982. doi: http://dx.doi.org/10.1016/0020-7225(82)90036-2.

Yi Xiong, Phil Winterfeld, Cong Wang, Zhaoqin Huang, and Yu-Shu Wu. Effect of large capillary pressure on fluid flow and transport in stress-sensitive tight oil reservoirs. 2015. doi: 10.2118/175074-MS.

Bicheng Yan, Masoud Alfi, Cheng An, Yang Cao, Yuhe Wang, and John E. Killough. General multi-porosity simulation for fractured reservoir modeling. *Journal of Natural Gas Science and Engineering*, 33:777 – 791, 2016. ISSN 1875-5100. doi: http://doi.org/10.1016/j.jngse.2016.06.016.

J. Yi, I. Y. Akkutlu, and C. V. Deutsch. Gas transport in bidisperse coal particles: Investigation for an effective diffusion coefficient in coalbeds. 2008. doi: 10.2118/08-10-20.

Min Zhang, Jun Yao, Hai Sun, Jian-lin Zhao, Dong-yan Fan, Zhao-qin Huang, and Yueying Wang. Triple-continuum modeling of shale gas reservoirs considering the effect of kerogen. *Journal of Natural Gas Science and Engineering*, 24:252–263, 5 2015. doi: http://dx.doi.org/10.1016/j.jngse.2015.03.032.

Nan Zhao. Integration of reservoir simulation and geomechanics. 2012. URL `http://cdmbuntu.lib.utah.edu/utils/getfile/collection/etd3/id/1109/filename/1108.pdf`.

Robert W. Zimmerman, Gang Chen, Teklu Hadgu, and Gudmundur S. Bodvarsson. A numerical dual-porosity model with semianalytical treatment of fracture/matrix flow. *Water Resources Research*, 29(7):2127–2137, 1993. ISSN 1944-7973. doi: 10.1029/93WR00749.

APPENDIX A

ESTIMATION OF KEROGEN BULK VOLUME

Here, I show the derivation of an expression for the kerogen bulk volume in terms of input parameters– $\epsilon_{ks}, \epsilon_{kp}, \phi$ and bulk volume (V_b).

By definition:

$$\epsilon_{ks} = \frac{GV_k}{GV} \tag{A.1}$$

This implies that:

$$GV_k = \epsilon_{ks}\, GV \tag{A.2}$$

Similarly, from the definition of ϵ_{kp} as the ratio of the kerogen pore volume to the total pore volume (PV), I obtain:

$$PV_k = \epsilon_{kp}\, PV \tag{A.3}$$

By volume balance,

$$V_b^k = PV_k + GV_k \tag{A.4}$$

Substituting Eq. A.2 and Eq. A.3 into Eq.A.4 yields:

$$V_b^k = \epsilon_{kp}\, PV + \epsilon_{ks}\, GV \tag{A.5}$$

Since porosity is defined as the ratio of pore volume to bulk volume, I can write pore volume PV as:

$$PV = \phi\, V_b \tag{A.6}$$

Similarly, I can express the grain volume, GV as:

$$GV = (1 - \phi)\, V_b \tag{A.7}$$

Substituting Eq.A.6 and Eq. A.7 into Eq. A.5 yields:

$$V_b^k = \epsilon_{kp}\, \phi\, V_b + \epsilon_{ks}\ (1 - \phi)\, V_b \tag{A.8}$$

APPENDIX B

COMPUTATIONS OF GEOMETRIC FACTOR

I already showed how to compute the geometric factor for a sphere with radius r and a cube with sides, x. Here, I proceed to show the computation of some rectangular geometries with sides that are functions of x. The idea is to show the effect of these aspect ratios on the estimated geometrical factors that go into the computation of the shape factor. Figure B.1 shows the cube, whose geometric factor was determined in the dissertaion, together with two other cuboids with different aspect ratios. Following the procedure explained in the section on the estimation of shape factors, the geometric factor, $\mathcal{G}_A$ for Cuboid 1 is 21, while that for Cuboid 2 is 68.25. This shows that the geometric factor increases significantly as the kerogen geometry gets flatter and longer. The comparison of the geometric factor of the cube to that of the sphere (given in the section on the estimation of shape factors) indicates that the shape factor for a flat surface is less than that for a convex surface. We also expect that the shape factor for a concave surface will be further less than that for a flat surface.

In comparison to the shape factors for conventional dual-porosity models for matrix and fractures , we expect the shape factors for kerogen in shales to be much larger because

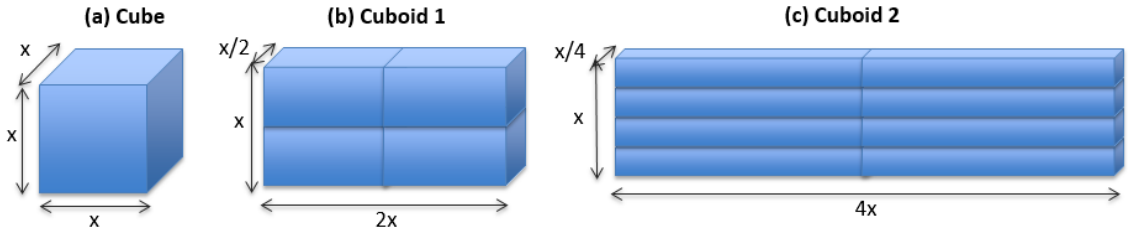

Figure B.1: Illustration of the effect of aspect ratios on geometric factors

of the rather dispersed nature in which kerogen is deposited in shales, as seen in SEM images. The dispersed kerogen matrix is expected to give larger shape factors than the rather large and blocky matrices that are typically seen in the illustrations of the Warren and Root model (Warren and Root, 1963).

APPENDIX C

MESH SENSITIVITY STUDIES

As part of the model validation studies performed in this work, I performed sensitivity studies to evaluate the sensitivity of the model to mesh sizes and mesh orientation. All the sensitivity studies shown in this appendix were based on the result from a single "stencil", as shown and discussed in Figure 5.16. Considering that the size of the smallest elements in the reservoir domain are located around the surface of the hydraulic fractures, I generated increasingly larger meshes by specifying the sizes of the smallest finite elements. The size of the other elements in the domain generally increase away from the fracture surface. Using Gmsh, I created different meshes with the size of the smallest element increasing

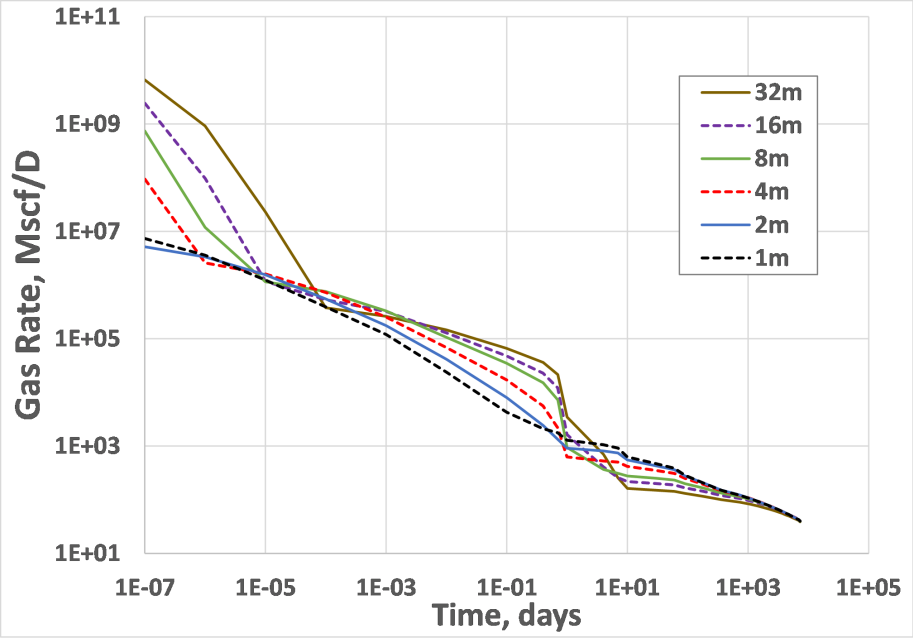

Figure C.1: Illustration of the effect of mesh size on the model estimates of production rate.

from 1 through 32 meters, each case having a size that is two times bigger than the previous one. The production rates from all of these cases are shown in Figure C.1. The cases with the smallest mesh sizes greater than 4 meters show distinct humps between 0.1 and 10 days. These humps could be interpreted as numerical artifacts related to the effect of adding the residual of the mass balance equations of the hydraulic fractures to those of the control volumes in which the hydraulic fracture segment is located (as explained in Section 4.4 on the "discrete fracture model"). At smaller mesh sizes, this effect is less significant as expected.

Table C.1 gives a quantitative analysis of the errors associated with the estimated production rates shown in Figure C.1. The estimated production rates from the domain with the finest mesh is used as the reference solution. In Table C.1, h is the size of the smallest mesh size in the domain, while $||\Delta q||$ is the L^2 norm of the difference between the production rate from any other mesh size and the reference solution. The results indicate that the estimated production rates are convergent. To evaluate the sensitivity of

Table C.1: Mesh Size Sensitivity

	2 m	**4 m**	**8 m**	**16 m**	**32 m**
$\|\|\Delta q\|\|$	1.44	4.27	10.82	16.12	30.59
$\|\|\Delta q\|\|/h$	0.72	2.14	5.41	8.06	15.30
$\|\|\Delta q\|\|/h^2$	0.36	0.53	0.68	0.50	0.48

the model to different mesh orientations, different meshing algorithms were used to discretize the reservoir domain. The three meshing algorithms used are the "Delaunay", "mesh adapt", and the "frontal" method. The resulting meshes from these three algorithms are shown in Figure C.2. Geuzaine and Remacle (2009) and the "Gmsh" reference manual (http://gmsh.info/doc/texinfo/gmsh) provides further details on these meshing algorithms.

The smallest mesh size, h used in the generation of all three meshes shown in Figure C.2 is 2 meters. However, the use of different meshing algorithms results in different total number of elements and vertices. Table C.2 presents the actual number of vertices and elements corresponding to the meshes shown in Figure C.2. It shows that the "frontal" algorithm used the most elements, while the "mesh adapt" algorithm used the fewest elements. It is worth noting that the default meshing algorithm in "Gmsh" is the "Delaunay" algorithm, and all other meshes used in this work were based on this algorithm. Figure C.3 shows the production rates corresponding to the meshes generated using these three algorithms. The production rate from the reference solution (based on the finest mesh solution with h=1 m) is also shown for comparison. The computed value of the L^2 norm of the error for the

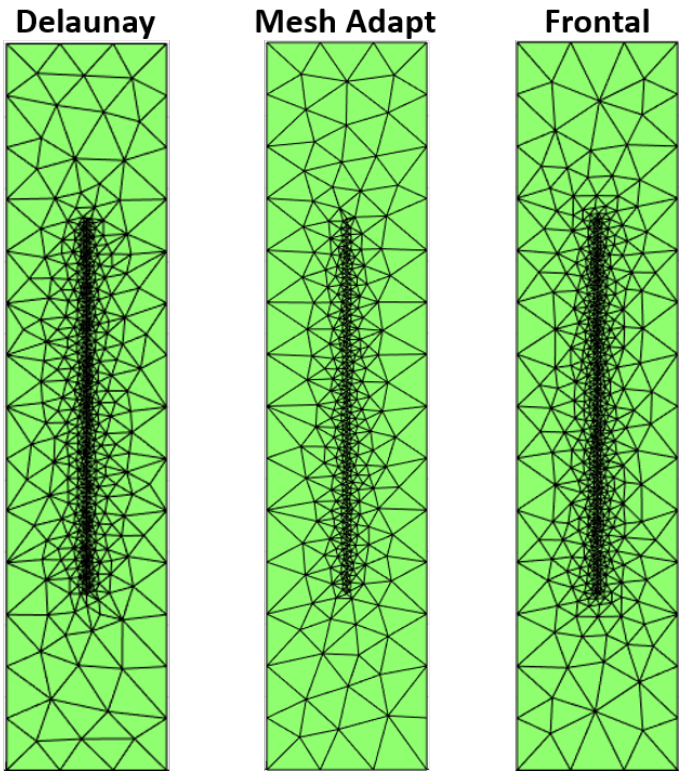

Figure C.2: Different mesh orientations based on the "Delaunay", "mesh adapt", and "frontal" algorithms.

Table C.2: Number of Elements and Vertices

	Delaunay	**Mesh Adapt**	**Frontal**
Vertices	635	465	664
Elements	1234	894	1292

"Delaunay", "mesh adapt", and "frontal" algorithms are 1.44, 2.01 and 1.36, respectively. This implies that the "frontal" algorithm was the most accurate, while the "mesh adapt" algorithm was the least accurate. The relative accuracy of these meshing algorithm could be related to the number of elements that were used to discretize the domain, because the most accurate mesh was the one that used the most elements, while the least accurate result came from the algorithm that gave the fewest elements.

In this dissertation, the time steps were selected to be very small at early times, and they arbitrarily increase in size at later times where this fine resolution is unnecessary. This is in order to capture the very early-time flow in the fractures. Time was discretized us-

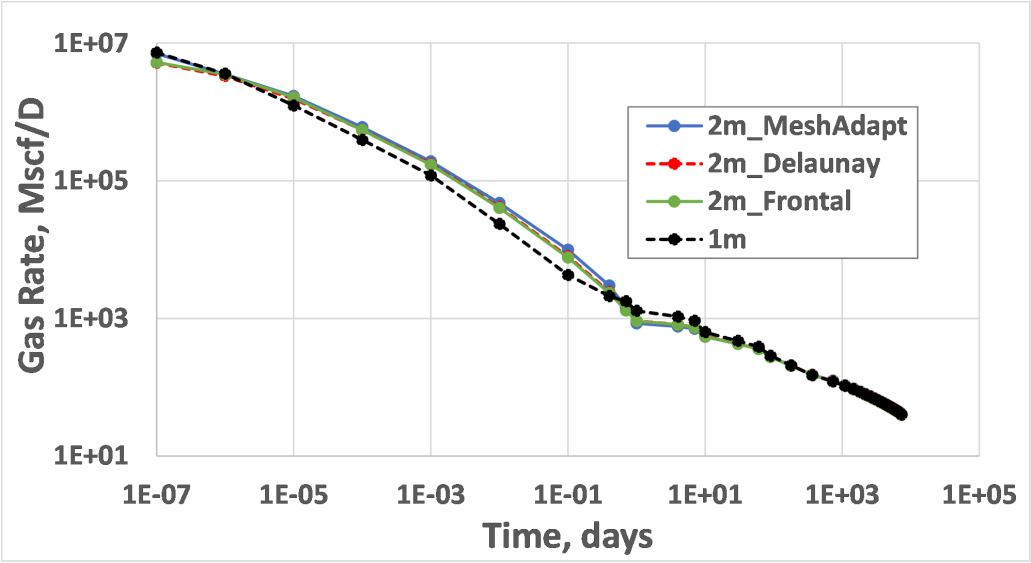

Figure C.3: Illustration of the effect of the meshing algorithm on the model estimates of production rate.

ing a fully-implicit backward Euler scheme, which theoretically guarantees unconditional stability. However, if a very large time step is taken at early times, the estimated mass of fluid to be withdrawn from a grid block (or control volume) could be larger than the mass of fluid stored in that grid block. This is easily seen when a very large initial step is taken, and the well model indicates the withdrawal of more fluid mass than is stored in the grid block in which the well is located. To overcome this potential problem, I implemented an adaptive time stepping where the time step size is automatically reduced whenever the model cannot converge on a solution. The implicit time-stepping, arbitrary spacing of time-step sizes, and the growing mesh sizes makes a time-step study less straight-forward. In Figures C.4 and C.5, I show simulation results with different arbitrary time-steps sizes. In addition to the base case, I ran two other cases with respectively fewer and more time steps than the base case. The log-log scale in Figure C.4 tends to exaggerate the differences at early times and it indicates. Figure C.5 shows the same results on a semi-log plot, and it indicates that all three cases appear almost identical. This implies that the sensitivity of the numerical model to time-step sizes is not significant.

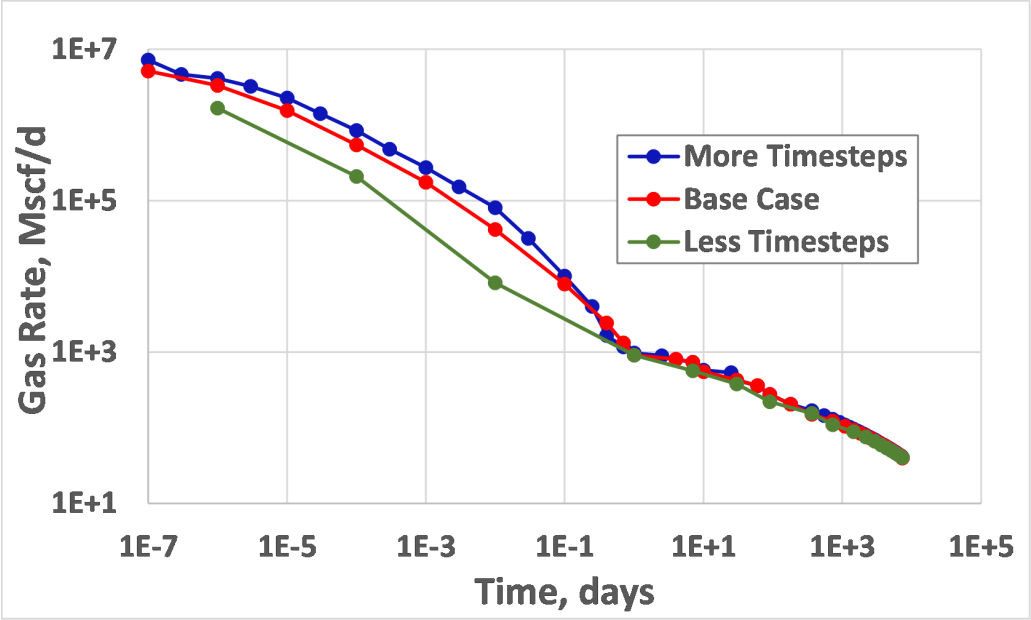

Figure C.4: The log-log rate plot illustrates the effect of time-step size on the model estimates of production rate. The log scale tends to exaggerate the differences at very early times.

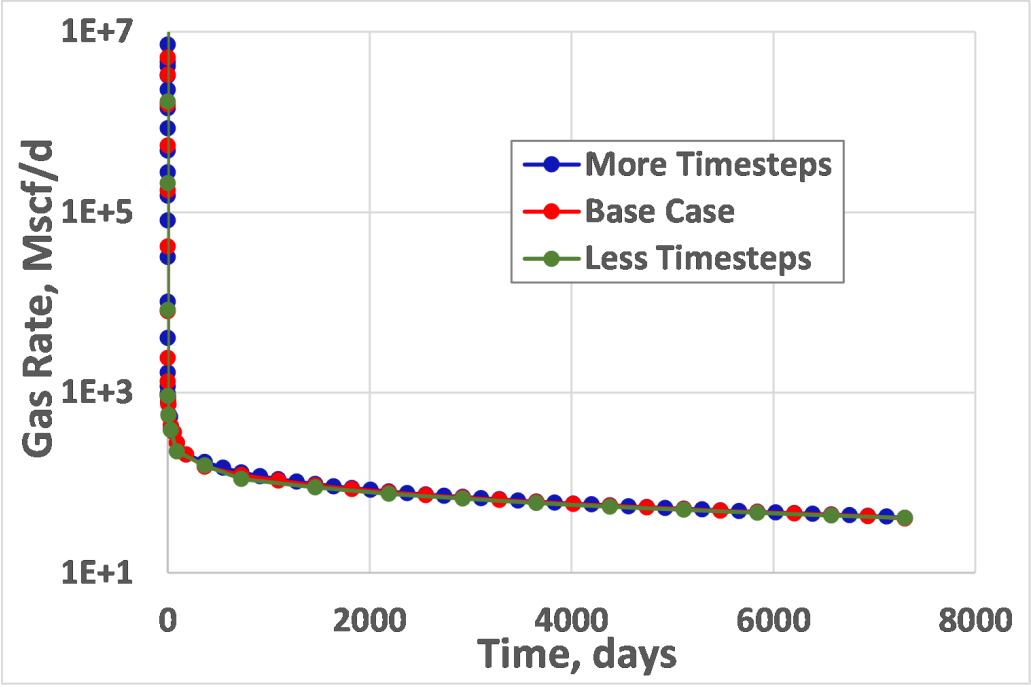

Figure C.5: The semi-log rate plot illustrates the effect of time-step size on the model estimates of production rate. The results from all three cases studied appear to match, indicating that the model sensitivity to time step size is not significant.